

UNIVERSITY OF NOVA GORICA  
GRADUATE SCHOOL

**STUDY OF ATMOSPHERIC AEROSOL  
TRANSPORT PROCESSES ON LOCAL AND  
REGIONAL SCALES**

DISSERTATION

**Tingyao He**

Thesis Advisor: prof.dr. Samo Stanič

Nova Gorica, 2013



UNIVERZA V NOVI GORICI  
FAKULTETA ZA PODIPLOMSKI ŠTUDIJ

**ŠTUDIJ LOKALNIH IN REGIONALNIH  
PROCESOV TRANSPORTA AEROSOLOV V  
OZRAČJU**

DISERTACIJA

**Tingyao He**

Mentor: prof.dr. Samo Stanič

Nova Gorica, 2013





To Lei, my life



## Acknowledgments

First, I would like to thank my advisor, prof.dr. Samo Stanič for giving me the opportunity to study in the Centre for Atmospheric Research, University of Nova Gorica, Slovenia. I would also thank him for his constructive ideas and strict supervision, and for helping with my family life in Slovenia. Great thanks to the members of the Centre for Atmospheric Research and Laboratory of Astroparticle Physics, who helped me with many tough problems related to my Ph.D. thesis. In particular, I am indebted to doc.dr. Klemen Bergant, doc.dr. Darko Veberič, dr. Fei Gao, doc.dr. Biagio Forte, dr. Alexandre Creusot, prof.dr. Martin O'Loughlin and Andreja Sušnik.

I would also like to thank prof.dr. Xiaoquan Song of Ocean Remote Sensing Institute, Ocean University of China, prof.dr. Dengxin Hua of School of Mechanical and Precision Instrument Engineering, Xi'an University of Technology and prof.dr. William Eichinger of IIHR Hydroscience & Engineering, University of Iowa for many valuable suggestions and assistance during my studies. My thanks goes to prof.dr. Andrej Filipčič, prof.dr. Marko Zavrtanik and Jure Eržen at Jožef Stefan Institute in Ljubljana, to Marko Trošt for his help with the measurements, Borut Likar for his help with coding and dr. Romina Žabar for providing great spot for lidar measurements at the Kekec guest house. Thanks to all my friends in Slovenia for making my stay enjoyable, doc.dr. Franc Marušič, doc.dr. Rok Žaucer, dr. Slavica Kochovska, doc.dr. Dorota Korte, Ambra Delneri, Maja Wagner and Maja Melinc Mlekuž and especially to Tea Stibilj Nemec.

Finally, thanks to my wife Ms. Lei Li who deserted her good position and accompanied me to enjoy the sour wine of unemployment and poverty in a remote country, and thanks to my little boy Fangyu for giving me so much happiness. My deepest gratitude goes to my parents and my parents-in-law for their continuous support, encouragement and understanding.



# Abstract

The aim of this dissertation was to study atmospheric aerosol transport processes on local and regional scales using remote sensing and in-situ measurement techniques. The main detection tools were a mobile scanning lidar operating at 1064 nm and a stationary vertical scanning lidar operating at 355 nm, stationed at Otlica, Slovenia. As a part of this thesis, both the hardware and the software for data acquisition and analysis of the mobile lidar system have been upgraded and validated in a multi-instrument measuring campaign.

On the local scale, we performed a number of case studies to investigate the concentration and distribution of urban aerosols over towns neighboring Nova Gorica, Slovenia, over Gorizia, Italy, over Ljubljana, Slovenia, and over Iowa City, USA. The measurement campaigns in Nova Gorica were aimed at tracking of spatial and temporal aerosol distributions, study of vertical atmospheric structure and identification of localized aerosol sources in different seasonal conditions. Daily cycles of aerosol loading in lower troposphere with a peak during the morning rush hours have been observed, as well as a number of point sources of particulate matter. Horizontal atmospheric extinction 200 m above the ground was found to be strongly correlated to  $PM_{10}$  and  $NO_x$  concentrations at the ground level. The Ljubljana campaign was aimed at the study of the atmospheric boundary layer (ABL) dynamics and aerosol loading. Here, remote sensing information was complemented by daily meteorological radiosonde measurements. The measurements clearly show daily variation cycles of the ABL height with stable ABL typically forming in the early morning. Aerosol loading shows two peaks, which can be related to human activities. On 18 June 2012, the slight change of synoptic conditions and the presence of mineral dust above Ljubljana resulted in an ABL about two times higher than on previous days. Based on ground-based measurements, the fraction of  $PM_{2.5}$  particles (in which the contribution of mineral dust was found to be high) in  $PM_{10}$  particles was found to be  $\sim 78.5\%$ . Another case study regarding local scale effects of air pollution from urban sources was performed in Iowa City and along highway Interstate 80 between Iowa City and Davenport, using a vehicle-mounted vertically oriented elastic lidar. Aerosol plume from local pollution sources within Iowa City was found to remain mostly at an altitude of 200 m above ground, with the maximum height and extinction coefficient of the aerosol layer gradually decreasing when moving to suburban areas. Measurements along highway Interstate 80 showed that aerosol loading was increased in the proximity of the interstate entry points and

smallest in the vicinity of the Mississippi River.

A study of long-range transport of aerosols was conducted from August to October 2010 using the stationary vertical scanning lidar at the Otlica observatory. The lidar data sample, which contains 38 night-time vertical profiles of the mean aerosol extinction, was combined with continuous O<sub>3</sub> concentration and daily radiosonde measurements. The obtained radiosonde- and lidar-derived heights of the ABL, which varied considerably from day to day, were found to be in agreement. The mean values of the aerosol optical depth (AOD) at 355 nm, were calculated separately for the ABL and for the free troposphere (FT). A ten-fold increase of the FT AOD was observed during the days with predicted presence of Saharan dust above the lidar site. To correlate AOD values with the type and origin of aerosols, backward trajectories of air-masses above Otlica were modeled using the HYSPLIT model and clustered. High ABL AOD values were found to be correlated with local recirculations and slowly approaching air masses from the Balkans and low values with northwestern flows. The highest values correlated with south-western flows originating in northern Africa. A preliminary study of the tropospheric structure above Vipava valley, Slovenia, was also performed in a simultaneous multi-instrument campaign using mobile lidar, stationary lidar and radiosonde investigating the same atmospheric volume. The lidar data was complemented by radiosonde measurements, launched at the intersection point of the two lidar traces. Two-layer aerosol structure obtained from the lidar data was found to be in agreement with the thermodynamical structure derived from the radiosonde data. The lidar further provided temporal development of the boundary layer structure during the observation time.

**Keywords:** Urban aerosols, atmospheric structure, lidar-based remote sensing, ground-based monitoring, radiosonde

# Povzetek

Glavni cilj disertacije je bil študij transporta aerosolov s pomočjo daljinskega zaznavanja in neposrednih meritev tako na lokalni skali kot tudi pri prenosu aerosolov na večje razdalje. Glavni raziskovalni orodji sta bila mobilni lidar (delujoč pri valovni dolžini 1064 nm) z možnostjo tridimenzionalnega pregledovanja ter stacionarni lidar na Otlici (delujoč pri valovni dolžini 355 nm) možnostjo dvodimenzionalnega vertikalnega pregledovanja atmosfere. Disertacija poleg raziskav atmosferskih pojavov zajema tudi razvoj in validacijo mobilnega lidarskega sistema in programskih orodij za zajem in analizo podatkov.

V okviru raziskav transporta aerosolov na lokalni skali smo izvedli večje število meriskih kampanj za določanje dinamike koncentracij in porazdelitev aerosolov v urbanih okoljih - v Novi in Stari Gorici, v Ljubljani ter v Iowa City, ZDA. Meritve v Novi Gorici so bile namenjene predvsem raziskavam časovnega razvoja prostorskih porazdelitev aerosolov in vertikalne atmosferske strukture ter identifikaciji lokaliziranih izvorov aerosolov v urbanem okolju. Opazili smo dnevne cikle v koncentracijah aerosolov v nižjih plasteh troposfere z značilnim jutranjim maksimumom, ki sovpada s prometno konico, ter uspeli identificirati število industrijskih izvorov, ki v ozračje spuščajo aerosole. Ugotovili smo, da je horizontalni koeficient atmosferske ekstinkcije na višini 200 m nad površjem močno koreliran s koncentracijami  $PM_{10}$  in  $NO_x$ , ki jih je izmerila prizemna okoljska postaja Agencije Republike Slovenije za okolje (ARSO). Meritve v Ljubljani so bile osredotočene na študij dinamike atmosferske mejne plasti (ABL) ter koncentracij aerosolov v njej. Informacije, pridobljene z daljinskim zaznavanjem smo dopolnili z meritvami meteoroloških balonov, ki jih ARSO izvaja enkrat dnevno. Rezultati jasno kažejo na dnevne variacije višine atmosferske mejne plasti, kjer se je stabilna ABL formirala šele nekaj po polnoči. Koncentracije aerosolov imajo izraziti jutranji in večernji maksimum, ki sta povezana s povečano aktivnostjo prebivalcev. 18. junija 2012 smo opazili približno dvakrat višje koncentracije aerosolov v ABL kot v predhodnih dneh. Talne meritve so pokazale, da gre za delce mineralnega prahu velikosti  $PM_{2.5}$ , ki so predstavljali kar  $\sim 78.5\%$  vseh delcev  $PM_{10}$ . V Iowa City smo raziskovali vpliv urbanih virov onesnaževanja ozračja na lokalne procese v atmosferi. Meritve smo izvedli z mobilnim, navpično usmerjenim lidaskim sistemom v gibanju po trasi od središča mesta Iowa City do sosednjega mesta Davenport. Plast aerosolov se je v samem mestu zadrževala na višini okoli 200 m nad površjem, tako višina kot koeficient slabitve pa sta se z oddaljenostjo od centra zmanjševala. Meritve vzdolž av-

tocestne povezave so pokazale, da prihaja do povišanih koncentracij aerosolov v bližini uvozov na avtocesto, najmanjše koncentracije pa smo zaznali v bližini reke Mississippi.

Študij transporta aerosolov na velike razdalje smo izvedli s ciklom meritev s stacionarnim lidarskim sistemom na observatoriju Otlica, trajajočim od avgusta do oktobra 2010. Nabor podatkov, ki zajema 38 nočnih vertikalnih profilov povprečnega koeficienta atmosferske ekstinkcije, smo kombinirali s podatki neprekinjenih meritev koncentracije  $O_3$  na Otlici in vertikalnimi profili atmosferskih lastnosti z meteoroloških balonov v Ljubljani. Višine ABL, ki smo jih neodvisno izmerili z daljinskim zaznavanjem in z meteorološkimi baloni, so se dobro ujemale, opazili pa smo signifikantne variacije na časovni skali nekaj dni. Srednje vrednosti optične globine aerosolov (AOD) pri valovni dolžini 355 nm smo izračunali posebej za ABL in za prosto troposfero. Ob določenih dnevih smo opazili do desetkratno povečanje AOD glede na njegovo običajno vrednost, kar se je časovno dobro ujemalo z modelskimi napovedmi prisotnosti Saharskega peska nad Otlico. Raziskali smo korelacijo med vrednostmi AOD ter predvidenimi tipi in izvori aerosolov, tako da smo trajektorije zračnih mas z modelom HYSPLIT in jih razporedili v značilne razrede. Ugotovili smo, da so visoke vrednosti AOD v mejni plasti korelirane z zračnimi masami, ki se dlje časa zadržujejo v lokalnem prostoru ali počasi napredujejo iz smeri Balkana. Nizke vrednosti AOD so korelirane z zračnimi masami, ki prihajajo s severozahoda, najvišje pa z jugozahodnimi zračnimi masami, ki izvirajo iz severne Afrike. V okviru disertacije smo izvedli tudi preliminarno študijo strukture troposfere nad Vipavsko dolino, kjer so meritve na istem prostoru potekale s hkratno uporabo dveh lidarjev in meteoroloških balonov, spuščениh v presečišču lidarskih sledi. Dvoplastna struktura aerosolov, razvidna iz lidarskega pregledovanja, je bila popolnoma v skladu s termodinamskim atmosferskim profilom, ki smo ga izluščili iz meritev meteorološkega balona, pri čemer nam je lidar dodatno omogočil podroben vpogled v časovni razvoj struktur v atmosferski mejni plasti v celotnem času opazovanja.

**Ključne besede:** okoljske meritve, aerosoli, atmosferska struktura, lidar, daljinsko zaznavanje, meteorološki balon



# 摘要

本课题主要是利用遥感和现场探测技术对大气气溶胶地方性和区域性运输过程进行研究。主要的遥感工具包括一台移动式三维扫描激光雷达(1064 nm)以及一台位于斯洛文尼亚奥特利察观测站的地基式垂直扫描激光雷达(355 nm)。作为课题的一部分，对移动式雷达系统的硬件以及数据采集分析软件进行了升级，并在多台仪器共同测量活动中得到验证。

在地方性运输的问题上，我们开展了多个城市的气溶胶的浓度和分布研究，包括斯洛文尼亚和意大利的边境城市，新戈里察/戈里齐亚，斯洛文尼亚的首都，卢布尔雅那，以及美国的爱荷华城。在新戈里察的研究主要是针对不同的季节追踪气溶胶的时空分布，研究垂直大气结构以及识别当地的气溶胶源。在实验中，我们观测到城区若干颗粒物源以及气溶胶日周期变化趋势，其中日最高值出现在早晨交通繁忙时刻。研究还表明地表200米高度的大气水平消光系数与地表的PM<sub>10</sub>和NO<sub>x</sub>含量有很强的相关性。卢布尔雅那的实验则主要研究气溶胶以及大气边界层的变化。实验获得的遥感信息与每日的气象探空气球测量进行了比对。实验结果清晰地显示日周期边界层变化。稳定的边界层一般在凌晨时分形成。气溶胶浓度在一天中出现两个峰值，都与人类活动相关。在2012年6月18日，由于沙尘天气出现在卢布尔雅那，致使边界层高度比之前几天高出一倍。地表的监测发现，PM<sub>2.5</sub>粒子在PM<sub>10</sub>中的比例高达~78.5%，这表明沙尘中含有大量的PM<sub>2.5</sub>粒子。另外一项城市气溶胶对当地的影响的研究在美国的爱荷华城和80号州际高速路上进行。实验使用一台车载式垂直测量激光雷达对道路上的气溶胶进行测量。实验表明，市内排放的气溶胶主要停留在地表200米高度内。随着汽车往郊区移动，气溶胶层的最大高度以及消光系数都在逐渐减小。沿着80号州际高速路的实验发现，气溶胶的增加主要发生在各个高速入口点，而气溶胶最小含量则出现在密西西比河附近。

从2010年8月至10月，气溶胶区域性长距离运输的研究在奥特利察观测站开展。实验观测主要使用地基式垂直扫描激光雷达完成。实验得到的38组日平均气溶胶消光系数曲线与每日的探空气球测得曲线以及地表臭氧(O<sub>3</sub>)含量进行比对。观测发现，虽然每日的边界层高度变化很大，但是由激光雷达与探空气球分别获得的数据具有很好的一致性。分别对边界层和自由对流层的气溶胶光学厚度进行计算发现，在沙尘天气里，自由对流层的气溶胶光学厚度甚至出现10倍的增长。为了进一步研究气溶胶光学厚度与其来源的相关性，我们使用HYSPLIT大气模型对抵达奥特利察观测站的气团进行了计算，并对其进行簇分析。结果表明，当地气流的再循环以及巴尔干半岛的缓慢气流会产生比较高的边界层内气溶胶光学厚度，而从西北方向快速移动的气流只带来少量气溶胶。最高的光学厚度则发现与西南的气流相关，该气流主要起源于北非地区。我们还使用两台扫描激光雷达和无线电探空气球对斯洛文尼亚维帕瓦山谷的大气结构进

行初步的可行性研究。激光雷达观测到的两气溶胶层结构与探空气球观测的热力学结构一致。激光雷达可视化数据进一步显示了山谷内的随时间变化的大气边界层结构。

**关键词:** 城市气溶胶, 大气结构, 激光雷达遥感, 地表监测, 无线电探空气球

# Contents

<b>1</b>	<b>Introduction</b>	<b>1</b>
1.1	Motivation . . . . .	1
1.2	State of the art in the field . . . . .	3
1.3	Purpose of the performed research . . . . .	6
<b>2</b>	<b>Light propagation in the atmosphere</b>	<b>7</b>
2.1	The atmosphere . . . . .	7
2.1.1	Troposphere . . . . .	8
2.1.2	Atmospheric boundary layer . . . . .	8
2.2	Propagation of light . . . . .	9
2.2.1	Rayleigh scattering . . . . .	11
2.2.2	Mie scattering . . . . .	12
2.2.3	Fluorescence . . . . .	13
<b>3</b>	<b>Lidar-based remote sensing</b>	<b>17</b>
3.1	Mobile Mie-fluorescence lidar . . . . .	17
3.1.1	Configuration of the mobile lidar system . . . . .	18
3.1.2	Validation of the mobile lidar system . . . . .	21
3.1.3	Detection in the fluorescence channel . . . . .	23
3.2	Stationary Mie lidar . . . . .	26
3.3	Vehicle-mounted Mie lidar . . . . .	28
3.4	Data structure of the UNG lidar systems . . . . .	28
3.5	Lidar equation and inversion methods . . . . .	30
3.5.1	Slope method for a homogeneous atmosphere . . . . .	30
3.5.2	Boundary point solution . . . . .	31
3.5.3	Multiangle method . . . . .	33
3.6	Absolute calibration of the vertical scanning lidar . . . . .	34

<b>4</b>	<b>Tracking of aerosols in urban environment</b>	<b>40</b>
4.1	Tracking of urban aerosols in Nova Gorica . . . . .	40
4.1.1	Geographic properties of the study area . . . . .	40
4.1.2	Remote sensing . . . . .	41
4.1.3	Ground-based measurements . . . . .	45
4.1.4	Structure of lower troposphere . . . . .	45
4.1.5	Identification of aerosol sources . . . . .	46
4.1.6	Daily aerosol cycles . . . . .	48
4.1.7	Correlation between aerosol extinction and $PM_{10}$ concentration .	50
4.2	Winter-time measurements in Nova Gorica . . . . .	53
4.2.1	Vertical atmospheric structure . . . . .	53
4.2.2	Localized aerosol sources . . . . .	55
4.3	Observation of atmospheric processes in Ljubljana . . . . .	57
4.3.1	Measurements . . . . .	57
4.3.2	Results and discussion . . . . .	57
4.4	Investigation of aerosol distributions in Iowa City . . . . .	64
4.4.1	Experimental setup . . . . .	64
4.4.2	Aerosol presence in the vicinity of Iowa City . . . . .	65
4.4.3	Area dependence of aerosol extinction . . . . .	67
4.5	Conclusions . . . . .	68
<b>5</b>	<b>Investigation of long-range transport of aerosols</b>	<b>71</b>
5.1	Measurements and data analysis . . . . .	72
5.1.1	Lidar-based remote sensing . . . . .	72
5.1.2	Radiosonde observations . . . . .	74
5.1.3	Ground-based measurements . . . . .	75
5.2	Aerosol transport modeling . . . . .	75
5.2.1	Air trajectories . . . . .	75
5.2.2	Presence of Saharan dust . . . . .	76
5.3	Cluster analysis of backward trajectories . . . . .	78
5.4	Long-term variation of the boundary layer height . . . . .	79
5.5	Impact on local environment . . . . .	82
5.6	Conclusions . . . . .	87
<b>6</b>	<b>Observation of atmospheric structure over complex terrain</b>	<b>89</b>
6.1	Geographic location and experiments . . . . .	89

6.2	Lidar-based measurements of tropospheric structure . . . . .	92
6.3	Radiosonde measurements of tropospheric structure . . . . .	95
6.4	Discussion . . . . .	96
<b>7</b>	<b>Conclusions and perspectives</b>	<b>99</b>
	<b>Appendix</b>	<b>103</b>
	<b>References</b>	<b>107</b>



## Introduction

### 1.1 Motivation

Atmospheric aerosols, including dust, smoke, and clouds which are mainly present in the troposphere, play an important role in global and regional climate changing processes ([Andreae and Crutzen, 1997](#); [Kaufman et al., 2002](#)). Because of their absorbing and scattering properties, the presence of aerosol particles can directly and indirectly affect Earth's radiation budget, as well as influence cloud properties through a variety of different physical mechanisms ([Li, 1998](#); [Che et al., 2005](#)). Increased aerosol loading with dust and smoke due to human activities produces a negative radiative forcing, similar in magnitude to the positive radiative forcing associated with the increase in anthropogenic greenhouse gases ([Forster et al., 2007](#)). Due to the importance of the impact of aerosols on global and local climate, many studies have been made of their radiative and micro-physical properties as well as their distributions and transport (e.g. [Betzer et al., 1988](#)). As the presence of aerosols in the atmosphere strongly varies with respect to time and location due to various natural and anthropogenic influences (proximity of sources, meteorological conditions, etc.), they might have large effects in some regions, whereas almost no effects in other regions. Due to data on spatial and temporal aerosol distribution are rather sparse and high uncertainties, direct and indirect effects of aerosols on climate are still not well understood. Obtaining information on atmospheric aerosol sources and transport of aerosols is of great importance for complete understanding of meteorological and climatological processes as well as facilitating of extended environmental studies.

On a local scale, increase of aerosol concentration has a significant impact on the status of the environment and quality of life for the inhabitants. In addition to atmo-

## Atmospheric observation tools

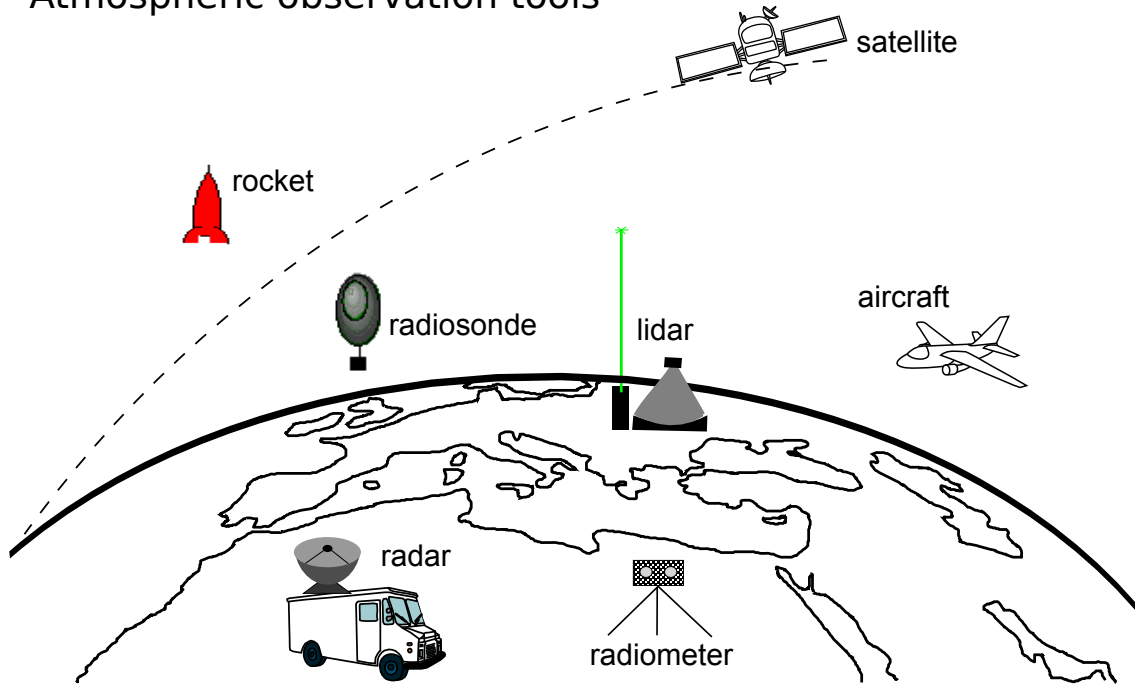


Figure 1.1: Main tools of atmospheric detection.

spheric circulation, a large source of anthropogenic pollution is mainly responsible for the local environment. With the increasing urbanization and industrialization, high concentrations of particulate matter, which are often found in urban areas (Hofmann, 1993; Rosenfeld, 2000), are as a rule due to a combination of many aerosol emissions, atmospheric conditions and specific topography of the area. The main cause of the increase of aerosol concentrations arises from human activities (IPCC, 2007), which may have significant environmental and climatological impacts as well as considerable effects on human health, as they may, e.g., increase the rates of the atmospheric photochemical reactions, reduce visibility and cause epidemiological diseases in general. The guidelines for the ambient air quality in Europe are set by the 2008/50/EC (EC, 2008) of the European Commission, where the allowed upper limit of  $\text{PM}_{10}$  particles is set to  $50 \mu\text{g m}^{-3}$  from 1 January 2010 and the allowed upper limit of  $\text{PM}_{2.5}$  particles to  $25 \mu\text{g m}^{-3}$  from 1 January 2015. The need for meeting and enforcing these standards calls for extensive air quality monitoring and distributed measurements of aerosol particle concentrations in inhabited areas.



## 1.2 State of the art in the field

The awareness of atmosphere related problems such as the air pollution and climate change is becoming more and more present. Observational instruments and techniques for the investigation of atmospheric processes have been developed. Figure 1.1 represents main observation tools for the atmosphere. Basic tools for the assessment of air quality and atmospheric observation are ground-based monitoring stations that provide continuous point-source measurements of particulate matter concentrations, presence of various gaseous pollutants and general meteorological data (temperature, relative humidity, pressure, wind speed and direction, etc.). However, ground-based in-situ measurements can not profile atmospheric parameters as a function of altitude, that instead give locally representative information. Aircraft instruments can capture aerosol properties at selected altitudes but only perform for short time intervals during field campaigns (Russell et al., 1999). Passive remote sensing (e.g. Sun photometers) measurements are averaged over the entire atmosphere column, but are not able to provide vertical aerosol distributions and can only be performed under total cloud free condition (Holben et al., 1998). Therefore, winter data in mid-latitudes are not very frequent and there is definitely a “good weather” bias of those measurements. Satellite measurements of the global climate change, global radiation and large scale aerosol transport, have been conducted by several countries and organizations in recent years (Herman et al., 1997). They provide an overall view into the atmosphere, however, the low resolution (Kaufman et al., 1997) limits the accurate models in local areas. Additionally, satellite data are still of high uncertainty over land, where the main aerosol sources are. A complete and real-time description of the atmosphere from conventional radiosonde measurements made twice a day is not sufficient to obtain a thorough understanding.

A modern remote sensing tool for the study of atmospheric characteristics is lidar (Measures, 1984; Kovalev and Eichinger, 2004; Weitkamp, 2005), which is also known as laser radar. LIDAR (LIght Detection And Ranging) as an optical tool that can profile the atmosphere and can measure the vertical distribution of aerosols with high spatial and temporal resolution, which is of essential relevance to understand their effects on climate and environment. Many lidar systems (Mie lidar, Raman lidar, high-spectral-resolution lidar, etc.) have been developed and implemented for atmospheric state studies (e.g. Hair et al., 2001), for measurements of aerosol optical properties (e.g. McGill et al., 2002; Bosenberg et al., 2003) and for air pollution studies in the atmospheric boundary layer in urban areas (e.g. Cooper and Eichinger, 1994; Devara et al.,

1994). In addition to ground-based lidars, the Cloud-Aerosol lidar with Orthogonal Polarization (CALIOP) onboard the Cloud-Aerosol lidar and Infrared Pathfinder Satellite Observations (CALIPSO) has been since June 2006 providing data on the global scale for the characterization of aerosols and clouds (Winker et al., 2007, 2009, 2010).

The first studies of the atmospheric properties using laser devices were undertaken by Fiocco and Smullin (1963), who recorded laser echoes from the upper atmosphere. Over the 40 years since this pioneering work, great strides have been made based on the development of  $Q$ -switching by McClung and Hellwarth (1962), which led to the generation of very short, single laser pulses and made possible range-resolved measurements. The energy compression afforded by  $Q$ -switching also gave rise to laser power densities that the measurements based on inelastic scattering, absorption and fluorescence were plausible. In recent years, optical and electronic technology has made great advances, enabling the wide use of lidar in the atmospheric studies (e.g. Ansmann et al., 1990; Hua et al., 2004).

Scheme of a typical lidar is shown in Fig. 1.2. Lidar systems operate on principles similar to that of radar. Laser pulses are emitted into the atmosphere. Light from the beam is scattered in all directions from molecules and particles in the atmosphere. Backscattering light, a portion of the scattering light directed back to the lidar, is then collected by a telescope and redirected to spectroscopic filter, where desired wavelengths and/or polarization states of the collected light are selected out. Photo-detector measures the intensity of returned light as a function of distance from the lidar. The electrical signal is then digitized and sampled by a data acquisition system.

Lidar has proven to be a powerful tool for detection of atmospheric aerosols and gas pollutants and has played an important role in this effort. Stationary ground-based lidars are usually situated at sites with high possibility for observation of atmospheric parameters and interesting processes such as aerosol long range transport. However, a combination of emissions, atmospheric conditions and specific topography patterns can result in high concentrations of pollutants in some areas, such examples are urban areas, proximity of power plants, factories, farms, etc. where may not be suitable for development of stationary lidar. In this case, a new type of lidar system which is compact, mobile and also capable of full time unattended aerosol observations is employed. Traditional micropulse lidars (e.g. Spinhirne, 1993) are inexpensive and reliable; however, they do not provide scanning capability, which is needed for the acquisition of two-dimensional aerosol information. Using scanning lidar (e.g. Spuler and Mayor, 2005) for aerosol tracking and source identification studies becomes more important associated with the emissions. Development of scanning mobile lidars has

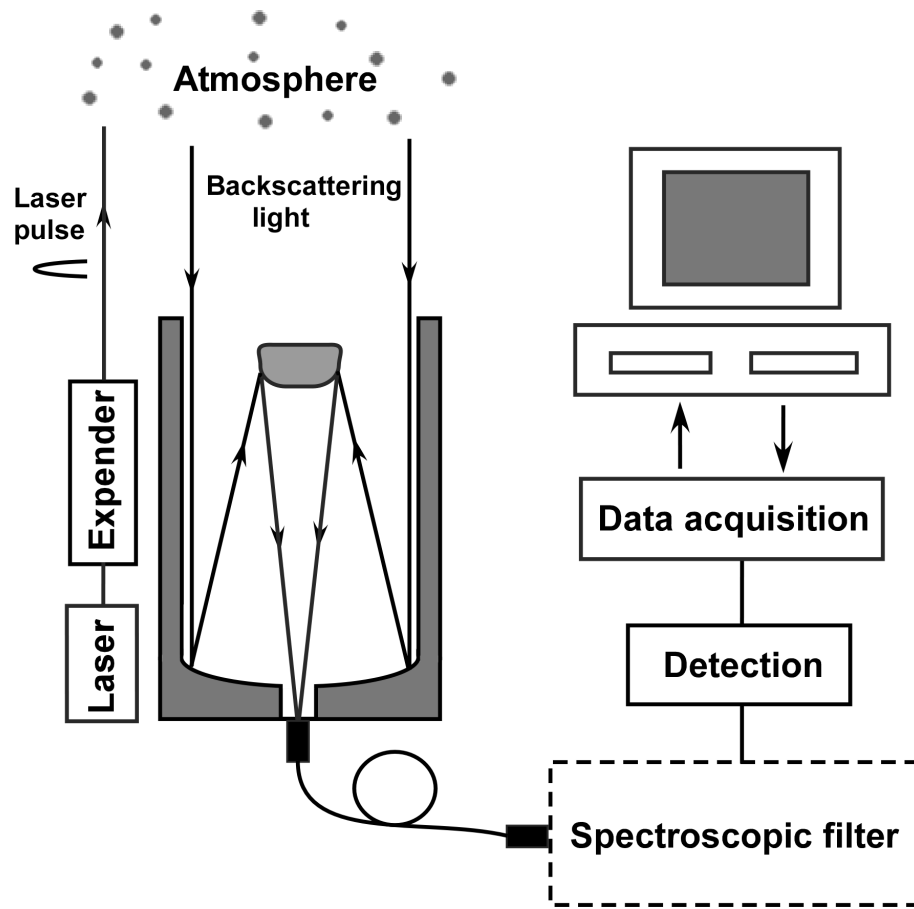


Figure 1.2: Schematic diagram of a lidar system.

been proceeding at an quickened pace, as it can be used for in-situ applications as tracers, by tracking inhomogeneities in the aerosol loading it is further possible to determine the dynamics of the atmospheric processes including operational meteorology and air pollution studies.

Using a time series of the scanned data, aerosol sources and its dynamics in the scanned area can be identified. In this sense, lidar has also been used in the visualization of atmospheric processes. However, despite the effort invested and the advances that have been made in the development of lidar systems for periodical and routine atmospheric measurements, no widely accepted method of lidar data inversion or analysis has been provided. The quality of the inverted lidar data depends largely on the experience and skill of the researcher, instead the data processing is considered a routine procedure. The classical methods for retrieving of lidar return signals such as Klett or Fernald method (Klett, 1981; Fernald, 1984), yield large uncertainties due to

the assumption of relationship between the extinction coefficient and the backscatter coefficient (so-called lidar ratio). One way to circumvent this fault is to employ multi-angle method (Kano, 1968; Hamilton, 1969; Sicard et al., 2002; Filipčič et al., 2003) using the scanning lidar. The multiangle method utilizes the dependence of the atmospheric attenuation coefficient on the zenith angle to obtain the extinction and backscatter coefficients based on the assumption of horizontal atmospheric homogeneity. As the atmospheric boundary layer over urban areas is generally turbulent and heterogeneous (Spinhirne et al., 1980; Kovalev and Eichinger, 2004), this method is rarely used due to the inaccuracy of the horizontal atmospheric homogeneity assumption.

### 1.3 Purpose of the performed research

The research in the scope of my Ph.D. thesis was oriented towards the study of atmospheric aerosol transport processes on local and regional scales using combined lidar-based remote sensing, radiosonde and surface meteorological measurements. Investigation of short-term appearances of increased aerosol loading in urban areas was centered around scanning mobile lidar measurements, yielding detailed information on the dynamics of the atmospheric boundary layer. The device was upgraded as a part of this work, both in hardware and in data processing techniques. The study of long-range aerosol transport was centered around measurements by a stationary lidar at the University of Nova Gorica's Otlica observatory. This research provided information on long-range transport mechanisms and their effects on the local environment.

## Light propagation in the atmosphere

In lidar-based remote sensing of atmospheric properties the atmosphere is probed by a laser beam, which interacts with atmospheric constituents (molecules and particles). Scattering and absorption of light beam in the atmosphere are very complicated, and the theory is well developed (e.g. [Van de Hulst, 1957](#); [McCartney, 1977](#); [Bohren and Huffman, 1983](#)). In this chapter, only some basic information on the atmosphere and a summary of relevant processes affecting lidar operation, such as Rayleigh scattering, Mie scattering and fluorescence, are presented. While it is not a direct result of my work, it provides the frame for understanding and interpretation of my results. Unless specifically cited otherwise in the text, this chapter is based on works by [Van de Hulst \(1957\)](#) and [McCartney \(1977\)](#).

### 2.1 The atmosphere

The atmosphere is a relatively thin gaseous layer surrounding the earth. The major constituents of the atmosphere are nitrogen, oxygen, argon and different trace gases. Solid particles, aerosols and liquid and/or solid water are also present, and are highly variable in concentration both spatially and temporally. According to the temperature structure, the atmosphere is generally divided into five main layers ([U.S. Standard Atmosphere, 1976](#)): the exosphere, the thermosphere, the mesosphere, the stratosphere, and the troposphere. The troposphere can further be divided into the atmospheric boundary layer (ABL)<sup>1</sup> and the free troposphere (FT). The ABL is directly affected by interaction with the Earth's surface.

---

<sup>1</sup>Also known as planetary boundary layer (PBL).

### 2.1.1 Troposphere

The troposphere is the lowest portion of Earth's atmosphere, where nearly all weather takes place. It is a well-mixed layer and the rapid mixing encourages weather changes. Within the troposphere, air pressure and density rapidly decrease with height and the temperature generally decreases with a average lapse rate of approximately  $6.5\text{ }^{\circ}\text{C}/\text{km}$  ([U.S. Standard Atmosphere, 1976](#)). The troposphere contains approximately 80 % of the atmosphere's mass and 99 % of water vapor and aerosols. These aerosols affect significantly Earth's radiative budget by scattering or absorbing radiation ([Slingo, 1990](#)).

Sources of aerosols can be natural or man made. The natural sources include volcanoes, dust storms, sea spray, forest and grassland fires and pollens. Human activities, such as the combustion of fossil fuels, construction, power plants and various industrial processes, contribute to this natural burden. The shapes of the aerosols can be very complex, ranging from the very irregular fly ash to the spherical liquid droplets. Their size, chemical composition and optical properties may also change in time with relative humidity and the presence of chemically reactive molecules. Because of precipitation, particulates in the troposphere have relatively short lifetimes, and thus, the number distribution of particulates also rapidly varies. Recently, two in-situ techniques are used to monitor the concentration of particles: an electro-optical method which counts particles in certain size ranges and then provides a measure of aerosol number density; and a filter technique which monitors the total mass of particles collected (in  $\mu\text{g m}^{-3}$ ) ([Corn, 1968](#)).

Ozone ( $\text{O}_3$ ) is considered a toxic pollutant and a green house gas in the troposphere ([IPCC, 2007](#)), in contrast to this, it plays a beneficial role in the stratosphere from high energy ultraviolet absorption<sup>2</sup>. Ground-level ozone, though much less concentrated than ozone aloft, require a continuous monitor related to human health effects. The natural sources of ozone near the ground level include transport from the stratosphere, lightning and volcanic eruptions. Human activities (such as incomplete combustion of fossil fuels, etc.) produce ozone through releasing hydrocarbons and nitrogen oxides ( $\text{NO}_x$ ), which react in photochemical and chemical processes in the presence of sunlight.

---

<sup>2</sup>Commonly known as the ozone layer.

### 2.1.2 Atmospheric boundary layer

Atmospheric boundary layer (ABL) is the lowest 1–2 km of the troposphere that is directly affected by human activities. It responds to surface forcing with a time scale of about an hour or less (Stull, 1988). Because of turbulent motion and convection, emissions at the surface can be mixed throughout the depth of the ABL on timescales of an hour.

The ABL height varies diurnally being related primarily with solar activity. Solar heating at the surface causes thermals of warm air to rise, which is the main source of convection, transporting moisture, heat and particulates higher into the boundary layer. The top of the ABL is usually characterized by a sharp increase in temperature and a sudden drop in the concentration of water vapor and particulates as well as most trace chemical species. Due to the large number of sources at the surface, the highest particulate concentrations are generally found within the ABL (about 3–10 times greater than in the FT) (Kovalev and Eichinger, 2004).

In the boundary layer theory, temperature is usually taken to be the potential temperature,  $\theta_p$ . This is the temperature that would result if a parcel of air were brought adiabatically from some altitude to a standard pressure level of 1000 mbar. Near the surface, the difference between the actual temperature and the potential temperature is small, but at higher altitudes, comparisons of potential temperature are important to stability and the onset of convection. Tropospheric convection is associated with clouds, rain, and storms. A displaced parcel of air with a potential temperature greater than that of the surrounding air will tend to rise. Conversely, it will tend to fall if the potential temperature is lower than that of the surrounding air. The potential temperature is defined to be (Stull, 1988)

$$\theta_p = T \left( \frac{p_0}{p} \right)^{R_d/C_p}, \quad (2.1)$$

where  $T$  is the current absolute temperature of the parcel,  $p_0$  a standard reference pressure, usually 100 kPa,  $p$  the pressure at the altitude to which the parcel is displaced;  $R_d$  is the gas constant for dry air,  $R_d = 287.04 \text{ J kg}^{-1} \text{ K}^{-1}$ ,  $C_p$  is the specific heat of air at constant pressure,  $C_p = 1005 \text{ J kg}^{-1} \text{ K}^{-1}$ .

## 2.2 Propagation of light

According to Beer's law<sup>3</sup>, when a collimated light beam passes through a turbid heterogeneous medium, the intensity of the radiation can be described as

$$I_\lambda = I_{0,\lambda} \exp \left[ - \int_0^R \alpha_\lambda(r) dr \right], \quad (2.2)$$

where  $I_{0,\lambda}$  is the radiant intensity of the light energy source,  $\alpha_\lambda(r)$  the probability per unit path length that a photon will be removed from the beam (scattered or absorbed), which represents the total extinction coefficient.

The optical transparency is written as (Bohren and Huffman, 1983)

$$T(R) = \exp \left[ - \int_0^R \alpha_\lambda(r) dr \right], \quad (2.3)$$

which describes the fraction of the original radiant flux that passed through a given range  $[0, R]$ . Transparency of the atmosphere is one of the most important parameters in the equations of laser monitoring, whose solutions enable extraction of quantitative information on the profiles of atmospheric gases and particles. The optical depth of the layer  $(0, R)$  then is defined as

$$\tau = \int_0^R \alpha_\lambda(r) dr. \quad (2.4)$$

The total extinction coefficient is a simple sum of the coefficients of all of the processes. Scattering processes depend significantly on the light wavelength and the width of the spectral interval. Lidar uses a laser source with a very narrow wavelength band, which is considered to be monochromatic light. According to the energy lost in the collision, the scattering processes are divided into elastic scattering (Rayleigh scattering and Mie scattering) and inelastic scattering (Raman scattering and fluorescence). Absorption depends on the light wavelength and the presence of the absorbers along the path of the emitted light. Water vapor, carbon dioxide, ozone, and oxygen are the main atmospheric gases that absorb light energy in the ultraviolet, visible and infrared regions of spectra. Most aerosols are non-absorbing in the visible range. At short wavelengths, the absorption is due to oxygen and ozone, while at longer wavelengths, to water vapor. As the present study is focused mainly on interaction of light with atmo-

---

<sup>3</sup>Often referred to as the Beer-Lambert-Bouguer's law.



spheric molecules and particles at wavelengths of 355 nm and 1064 nm, the contribution from molecular absorption to extinction coefficient is considered to be negligible. The molecular scattering of light is then described using Rayleigh theory (McCartney, 1977). The interaction of light with particles is given by Mie theory (Van de Hulst, 1957).

### 2.2.1 Rayleigh scattering

To account for pressure and temperature dependence, the scattering coefficient from gas molecules at wavelength  $\lambda$  can be shown to be (Penndorf, 1957; Bohren and Huffman, 1983)

$$\alpha_m = \frac{8\pi^3(n^2 - 1)^2 N_m}{3N_s^2 \lambda^4} \left( \frac{6 + 3\delta}{6 - 7\delta} \right) \left( \frac{p}{p_s} \right) \left( \frac{T_s}{T} \right), \quad (2.5)$$

where  $n$  is the refractive index,  $N_m$  is the number of gas molecules per unit volume (number density) at the existing pressure  $p$  and temperature  $T$ , and  $N_s$  is the number density of molecules at standard conditions ( $N_s = 2.547 \times 10^{19} \text{ cm}^{-3}$  at  $T_s = 288.15 \text{ K}$  and  $p_s = 101.325 \text{ kPa}$ );  $\delta$  is the depolarization factor of the scattered radiation which accounts for the anisotropy of the gas molecules.

The intensity of molecular scattering is proportional to  $1/\lambda^4$  (Eq. 2.5), therefore, the molecular scattering is considered to be negligible in the infrared region of the spectrum, and is dominated scattering in the ultraviolet region. Table 2.1 presents the quantitative data on molecular scattering coefficients  $\alpha_m$  and optical depth  $\tau_m$  of the atmosphere for different wavelengths.

Molecular scattering has a symmetric phase function  $P_m(\theta)$ , which is defined as the intensity of the scattered light at an angle  $\theta$  from the direction of the incident light. The normalized phase function is

$$P_m(\theta) = \frac{3}{16\pi}(1 + \cos^2 \theta). \quad (2.6)$$

It has the maximum value of  $3/8\pi$  for backscattered light ( $\theta = 180^\circ$ ) and for the light scattered in forward direction ( $\theta = 0^\circ$ ), while the minimum value for  $\theta = 90^\circ$  and  $270^\circ$ .

Rayleigh scattering also occurs when the incident light interacts with particulates, which are small in size relative to the wavelength of the incident light. As the characteristic sizes of the particulates approach the size of the wavelength of the incident light, Mie scattering occurs instead of Rayleigh scattering.

Table 2.1: Molecular scattering coefficients  $\alpha_m$  for different wavelengths at temperature  $T = 288.15$  K and pressure  $p = 101.325$  kPa, and optical depth  $\tau_m$  of the vertical atmosphere (Penndorf, 1957).

Wavelength $\lambda$ ( $\mu\text{m}$ )	Scattering coefficient $\alpha_m$ ( $\text{km}^{-1}$ )	Optical depth $\tau_m$
0.30	$1.446 \times 10^{-1}$	1.2237
0.36	$6.680 \times 10^{-2}$	0.5653
0.40	$4.303 \times 10^{-2}$	0.3641
0.50	$1.716 \times 10^{-2}$	0.1452
0.55	$1.162 \times 10^{-2}$	0.0984
0.60	$8.157 \times 10^{-3}$	0.0690
0.70	$4.364 \times 10^{-3}$	0.0369
0.80	$2.545 \times 10^{-3}$	0.0215
0.90	$1.583 \times 10^{-3}$	0.0134
1.06	$8.458 \times 10^{-4}$	0.0072

## 2.2.2 Mie scattering

Mie scattering can be visualized as an interaction between waves that wrap themselves around and through the particle. In which the circumference of the particle is exact multiples of the wavelength of the incident light, the cross sections are large, while the magnitude of the cross section is a minimum in which the circumference is a multiple of a wavelength and a half. When the diameter of the particle is very near the same size as the wavelength, most effective scattering occurs. The scattering process obeys the laws of geometric optics in which the size of the particles is much greater than the wavelength (Kovalev and Eichinger, 2004).

The intensity of the light scattering by particulates depends on the refractive index, the geometric size and shape of the particle, the wavelength of the incident light, and on the particulate number density. Mie theory assumes that the particle is homogeneous sphere, such that it can be characterized by a single refractive index for a radiation wavelength. In addition, the effects of multiple scattering are considered to be negligible (Bissonnette and Hutt, 1995; Bissonnette, 1996; Wandinger, 1998).

The efficiency factors of scattering ( $Q_{\text{sca}}$ ) and absorption ( $Q_{\text{abs}}$ ) are defined as the ratio of particulate scattering cross section ( $\sigma_{\text{sca}}$ ) and absorption cross section ( $\sigma_{\text{abs}}$ ), respectively, to the geometric cross section of the particle

$$Q_{\text{sca}}(x, m) = \frac{\sigma_{\text{sca}}(\rho, \lambda, m)}{\pi \rho^2}, \quad (2.7)$$

$$Q_{\text{abs}}(x, m) = \frac{\sigma_{\text{abs}}(\rho, \lambda, m)}{\pi \rho^2}, \quad (2.8)$$

where  $\rho$  is the particle radius,  $\lambda$  is the wavelength of the incident light. The parameters  $x$  and  $m$  characterize the relative size and relative index of refraction of the particle

$$x = \frac{2\pi\rho}{\lambda}, \quad (2.9)$$

$$m = \frac{m_1}{m_2}, \quad (2.10)$$

where  $m_1$  and  $m_2$  are the refractive indices of the particle and medium, respectively. In the atmosphere,  $m_2$  is considered to be 1.  $m_1$  is a complex number, whose real part is the index of refraction and imaginary part is the index of absorption. The efficiency of the total extinction then can be written as

$$Q_{\text{ext}} = Q_{\text{sca}} + Q_{\text{abs}}. \quad (2.11)$$

These efficiency factors are represented theoretically by infinite, slightly convergent series, described in detail by [Van de Hulst \(1957\)](#).

The total particulate extinction coefficient can be computed as

$$\alpha_p = N_p \pi \rho^2 Q_{\text{ext}}, \quad (2.12)$$

where  $N_p$  is the number density of the particles. In which the particle radii range from  $\rho_1$  to  $\rho_2$ , the integral form of Eq. 2.12 for the total extinction coefficient is established,

$$\alpha_p = \int_{\rho_1}^{\rho_2} N_p(\rho) \pi \rho^2 Q_{\text{ext}}(\rho, \lambda, m) d\rho. \quad (2.13)$$

The particulate phase function  $P_p(\theta, x)$ , which is more complicated than molecular phase function, is a function of the relative size  $x$ . For sizes  $x < 0.2$ , the angular distribution of particulate scattering is symmetric (equal scattering intensities for forward and backward directions), similar to that for molecular scattering. As the relative size increases, scattering in the forward direction increases in magnitude ([Kovalev and Eichinger, 2004](#)). In lidar applications, the numerical value of the scattering in the backward direction ( $\theta = 180^\circ$ ) is very important for data processing. It commonly assumes that the backscatter coefficient is proportional to the total extinction coefficient.

### 2.2.3 Fluorescence

Except for molecular and particulate elastic scattering constituents, which have the same wavelength as the incident light, some additional spectral constituents may exist, such as fluorescence constituent, in which wavelengths are shifted relative to that of the incident light (Measures, 1984). Fluorescence is the spontaneous emission of a photon following excitation into an excited state by absorption of incident light at a frequency within a specific absorption line or band of molecules. The re-emitted light measured at the appropriate frequency, is useful for identifying the molecular species responsible for the fluorescence. It has a longer wavelength and lower energy than the absorbed light in general (Lakowicz, 1999).

Fluorescence is considered as a two-step photon interaction consisting of absorption of a single photon with frequency  $\nu_0$  followed by spontaneous emission of a photon with frequency  $\nu_r$  (Fig. 2.1). Hence, it involves a time uncertainty between the two processes, which is called the fluorescence lifetime and is given by the inverse of the radiative decay rate  $1/\Gamma_r$  at very low pressures. However, fluorescence is generally modified by quenching in the atmosphere due to inelastic collisions with air molecules, which lowers the intensity by several orders of magnitude compared with the low pressure case (e.g. in the upper atmosphere). These collision processes also result in changes of the fluorescence spectral distribution and polarization (Lakowicz, 1999).

The cross section per molecule for fluorescence excited by monochromatic incident light with frequency  $\nu_0$  is written as

$$\sigma_f(\nu_0, \nu_L) = \frac{\sigma_{\text{abs}}(\nu_0, \nu_L)}{4\pi} Q \eta_F, \quad (2.14)$$

where  $Q$  is the quenching factor and  $\eta_F$  the fluorescence quantum yield (fluorescence efficiency), which is defined as the ratio of the number of photons emitted to the number of photons absorbed. The parameter  $\nu_L$  characterizes the central frequency of the absorption line. The absorption cross section  $\sigma_{\text{abs}}$  is expressed by (e.g. Fouche et al., 1972)

$$\sigma_{\text{abs}} = \frac{\pi c^2}{2\nu_0^2} \frac{F_{\text{total}}}{(\nu_L - \nu_0)^2 + F_{\text{total}}^2/4} A_{\text{ei}}, \quad (2.15)$$

where  $c$  is the speed of light and  $A_{\text{ei}}$  is the transition probability for the radiative process from excited state to initial state. The total bandwidth  $F_{\text{total}}$  of the excited state is the sum of the natural width  $F_N$ , the width due to the elastic collision  $F_E$  and the width

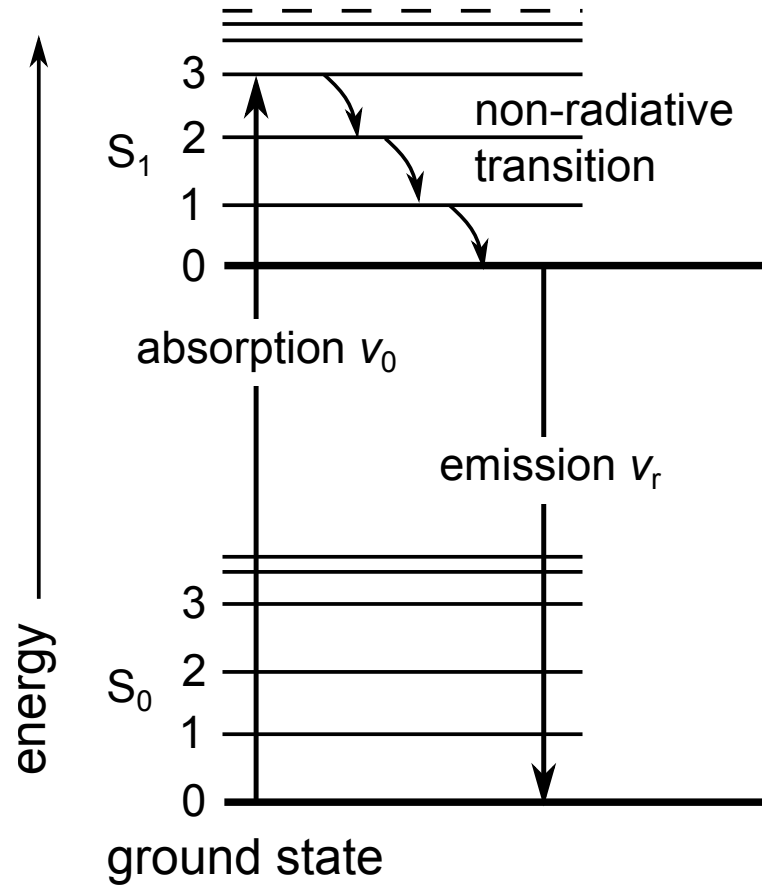


Figure 2.1: Schematic energy transfer diagram of fluorescence. After an electron absorbs a high energy photon the system is excited electronically and vibrationally. The system relaxes vibrationally, and eventually fluoresces at a longer wavelength ([Atkins and De Paula, 2002](#)).

for quenching  $F_Q$ ,

$$F_{\text{total}} = F_N + F_E + F_Q, \quad (2.16)$$

where  $F_E$  and  $F_Q$  are usually related to the pressure. The quenching factor  $Q$  is given by the Stern-Volmer equation

$$Q = \frac{1}{1 + F_Q/F_N}, \quad (2.17)$$

and the fluorescence efficiency  $\eta_F$  is determined by

$$\eta_F = \frac{\Gamma_r}{\Gamma_r + \sum_i \kappa_i}, \quad (2.18)$$

where the summation of  $\kappa_i$  represents all possible non-radiative transitions from the excited state ([Bernard, 2001](#)).

Fluorescence generally occurs only when the frequency of the exciting radiation lies within a particular absorption band of the material. Many biological materials in nature, such as fungi, pollens and bacteria, contain key constituent molecules which exhibit considerable absorption in UV and characteristic fluorescence emission spectra. UV laser-induced fluorescence has been developed as a standard technique used to discriminate between biological and non-biological particles (e.g. [Kliger, 1983](#)).

Discrimination mechanism of lidar system relies on transmitting light and detecting the wavelength-shifted fluorescence produced by the biological materials. The natural fluorophores, such as amino acids (e.g. tryptophan<sup>4</sup>), which are present in almost all biological substances, can be used as characteristic tracer of biological aerosols. Using fluorescence lidar, biological aerosols can be identified through the detection of fluorescence of the amino-acid tryptophan ([Lakowicz, 1999](#)). One of the most significant factors of fluorescence lidar is the wavelength of the UV excitation, which concerns the detection range and efficiency. Currently, most fielded lidars use either 266 or/and 355 nm UV light, which are easily derived from a Nd:YAG laser.

---

<sup>4</sup>Tryptophan resides in a protein, which is the dominant intrinsic fluorophore.

## Lidar-based remote sensing

Lidar emits laser pulses into the atmosphere and collects the light back-scatter in interaction with particles. High temporal and spatial resolution lidars can capture the vertical distribution of aerosol particles suspended in the air and observe the structure of atmosphere as well as pollutant transport in term of the boundary layer dynamics (Kovalev and Eichinger, 2004; He et al., 2012a). The three lidar systems used for remote sensing of atmosphere in this study were a mobile Mie-fluorescence lidar, a stationary ground-based Mie lidar located at Otlica observatory, Slovenia (45.93° N, 13.91° E, 945 m a.s.l.<sup>1</sup>) and a vehicle-mounted Mie lidar. The mobile Mie-fluorescence lidar provides automatic scanning in both azimuth and elevation angle with an angular resolution of 0.1°, while the stationary lidar has scanning functionality in elevation angle only, with a fixed azimuth angle of 235.1°. The vehicle-mounted lidar system is capable of taking vertical aerosol measurements while in motion and recording the current position using built-in GPS receiver. In this chapter, I present the scanning mobile Mie-fluorescence lidar (He et al., 2010) in detail and briefly describe the setup of the stationary Mie lidar (Gao et al., 2011a) and of the vehicle-mounted Mie lidar (Lewandowski et al., 2010).

### 3.1 Mobile Mie-fluorescence lidar

The scanning mobile Mie-fluorescence lidar at the University of Nova Gorica (UNG) can map and track aerosol loading within a radius of 10 km and identify biological aerosols through the detection of tryptophan fluorescence. The device, which can be operated in both day and nighttime conditions, includes three channels for the de-

---

<sup>1</sup>a.s.l. stands for “above sea level”.

Table 3.1: Specifications of the scanning mobile lidar. QE: Quantum Efficiency, T: Transmittance, R: Reflectance, CWL: Central Wavelength, FWHM: Full Width at Half Maximum, PT: Peak Transmission.

<b>Transmitter</b>	Nd:YAG pulsed laser		<b>Spectroscopy</b>	
Wavelength	1064 nm	266 nm	BS1	
Pulse energy	40 mJ	100 mJ	T	~90 % at 1064 nm
Pulse duration	9 ns	8 ns	R	~98 % at 260 – 300 nm
Max. repetition rate	10 Hz	10 Hz	BS2	
Beam diameter	7 mm	5.6 mm	T	~98 % at 295 nm
Beam divergence	1.2 mrad	0.7 mrad	R	~98 % at 266 nm
<b>Receiver</b>	Newtonian telescope		IF1	
Diameter	300 mm		CWL	$1064 \pm 0.15$ nm
Focal length	1500 mm		FWHM	$1.0 \pm 0.2$ nm
<b>Detectors</b>			PT	> 70 %
APD	EG & G C30954/5E		IF2	
QE	~38 %		CWL	$266 \pm 0.45$ nm
PMTs	Hamamatsu R7400		FWHM	$1.0 \pm 0.6$ nm
QE	~20 %		PT	> 18 %
<b>Data recorder</b>	Licel TR40-160		IF3	
Sampling rate	40 MSPS		CWL	$295 \pm 1.5$ nm
A/D resolution	12 bit		FWHM	$10.0 \pm 2.0$ nm
Range resolution	3.75 m		PT	> 25 %

tection of elastic scattering signals at 1064 nm and 266 nm as well as the fluorescence signal at 295 nm. An important benchmark confirming the functionality of the system were aerosol loading measurements pending the eruption of the Icelandic Eyjafjallajökull volcano on 14 April 2010. Experiments on 20 April 2010 showed an elevated aerosol layer above Nova Gorica ( $45.96^\circ$  N,  $13.64^\circ$  E) at an altitude of 2.5 km a.s.l., which was confirmed as a layer of volcanic ash by laboratory analysis of aerosol composition (Gao et al., 2011b).

### 3.1.1 Configuration of the mobile lidar system

A schematic diagram of the system configuration is shown in Fig. 3.1. Specifications of the system are summarized in Table 3.1. As a transmitter, a solid state Nd:YAG pulsed laser<sup>2</sup> is employed, which is capable of simultaneous emission of light pulses

<sup>2</sup>ULTRA CFR400, Quantel, USA.



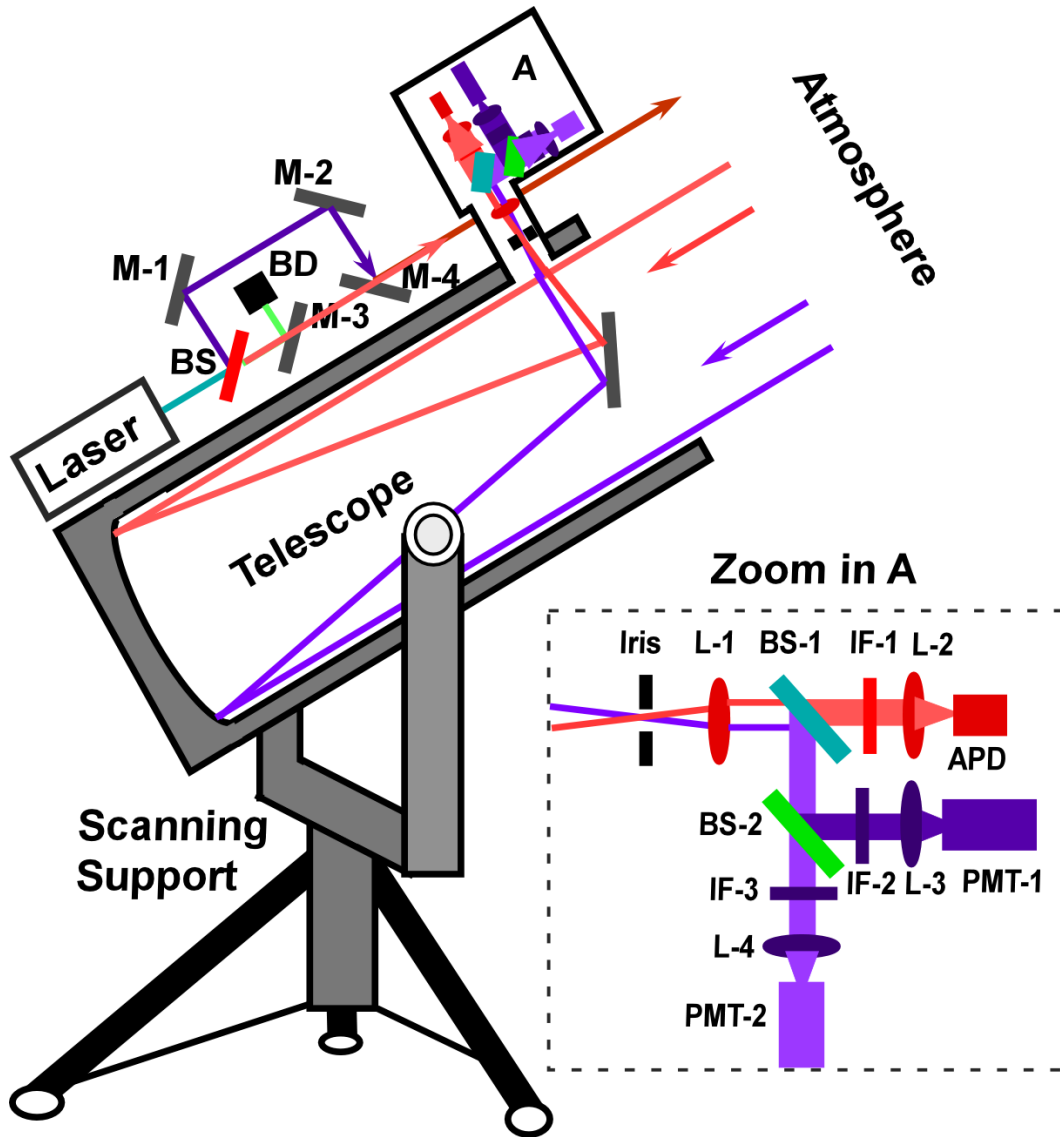


Figure 3.1: Schematic diagram of the optical components of the scanning mobile lidar. A detailed description of the spectroscopic filter is shown as an enlargement. BD: Beam Dump, BS: Beam Splitter, IF: Interference Filter, PMT: Photomultiplier Tube, APD: Avalanche Photodiode.

at 1064 nm, 532 nm and 266 nm. In our case, the unused 532 nm pulses are absorbed in a beam dump, which may induce noise in detection channels at other wavelengths. Since in the infrared detection channel the molecular backscatter signal is negligible compared to the particle backscatter signal, the fundamental wavelength (1064 nm) is used for aerosol detection. Tryptophan contained in biological aerosols is excited by 266 nm laser pulses and the return fluorescence signals are detected in a local peak of the spectral band centered at 295 nm, used for their identification. Figure 3.2 repre-

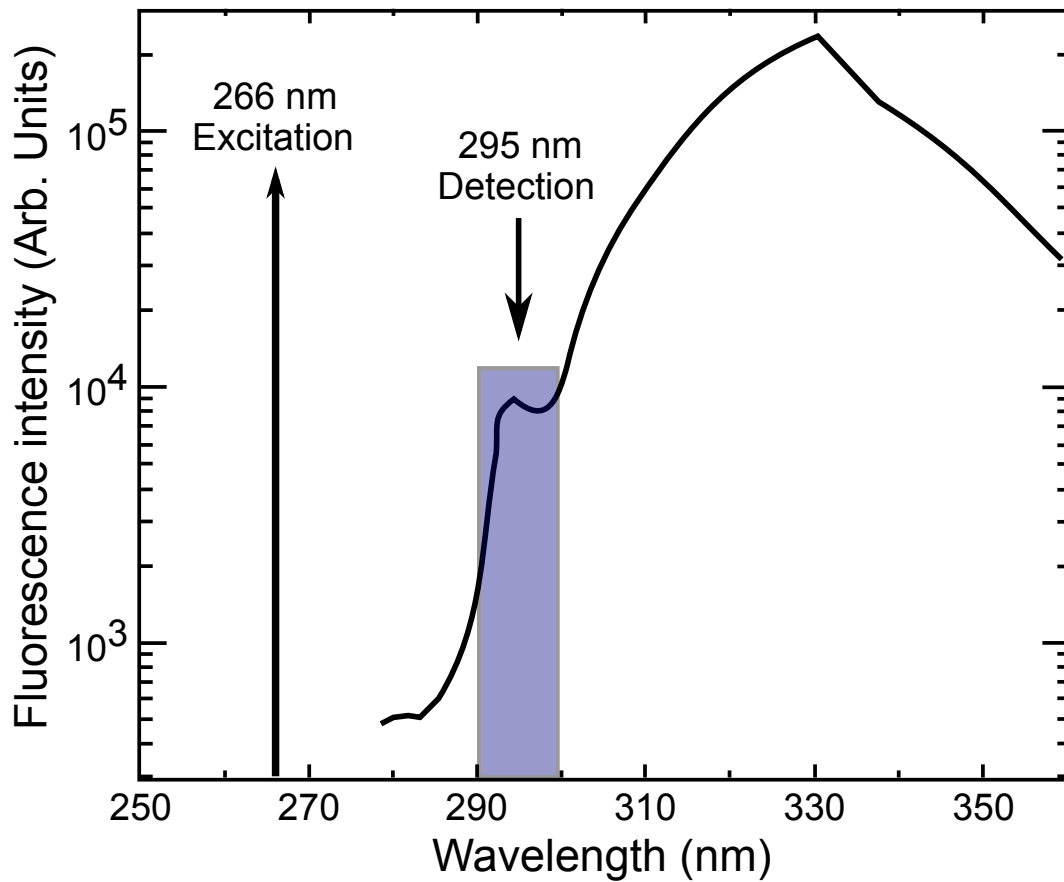


Figure 3.2: Fluorescence emission spectrum of the amino acid tryptophan for an incident laser wavelength of 266 nm (Kliger, 1983).

sents the fluorescence spectrum of the amino-acid tryptophan intrinsic to biological substances. The selected detection of 295 nm, instead of other spectral regions of larger intensity (for example, 330 nm), is to minimum the daylight background in the day-time operation. The 1064 nm and 266 nm beams overlap as they exit the laser and have a divergence angle of 1.2 mrad and 0.7 mrad, respectively, at a maximum repetition rate of 10 Hz. The pulse energy for 1064 nm is 40 mJ at 9 ns pulse width and 100 mJ at 8 ns width for 266 nm.

Backscattered light is collected by a Newtonian telescope<sup>3</sup> with a diameter of 300 mm and focal length of 1500 mm. In order to establish the scanning functionality, both the transmitter and the receiver are installed on a frame supporting which is steered by two servomotors<sup>4</sup> connected to the computer via a serial port. This enables

<sup>3</sup>Guan Sheng Optical Co., Ltd., Taiwan.

<sup>4</sup>Intelligent Motion System Inc., USA.

the lidar system scan in both azimuth ( $0^\circ - 360^\circ$ ) and elevation angle ( $-10^\circ - 90^\circ$ ) with an angular resolution of  $0.1^\circ$ . The transmitter and the receiver are configured bi-axial. As a result, the complete overlap region of the system starts from around 700 m. For the purpose of this study, lidar return signal was simply discarded in the first few hundred meters, where the overlap was not complete.

To suppress the background, an adjustable iris is placed at the focus of the telescope. After the iris, collected light is re-collimated and split into three channels using dichroic beam splitters and partial reflection mirrors. Finally, channel-specific interference filters<sup>5</sup> are used to suppress the interference light (Table 3.1). The return signals are detected by photomultiplier tubes (PMTs)<sup>6</sup> for 266 nm and 295 nm channels and an IR-enhanced Avalanche photodiode (APD)<sup>7</sup> for the 1064 nm channel. Output of the detector is then amplified and digitized by a three-channel transient recorder<sup>8</sup> with 12-bit A/D resolution at 40 MHz sampling rate and 16 k trace length in analog mode. Combined with a 250 MHz discriminator (64 different discriminator levels and two different preamplifier settings) in photon-counting mode, Licel transient recorder makes a large dynamic range of the acquired signal. These digitization parameters yield a range resolution of 3.75 m and a maximum theoretical detection range of 61.4 km. Signal averaging is performed inside the unit and a high speed data interface is applied to connect to the host computer, which allows readout of the acquired data between successive laser shots.

Transient recorder is connected to a Linux-based computer via an Ethernet link. The data acquisition (DAQ) software, developed within our laboratory, features graphical interfaces for the full detector, digitizer, laser and telescope control and is based on C++ code and the ROOT package<sup>9</sup>. The data is stored in ROOT binary files, including the setting information about the lidar run and the whole trace of the lidar return provided by transient recorders. The developed data analysis software provides real-time presentation of aerosol loading and visualization of atmospheric process in various environmental settings.

---

<sup>5</sup>Barr Associates Inc., USA.

<sup>6</sup>R7400, Hamamatsu, Photonics, Japan.

<sup>7</sup>EG & G C30954/5E, URS Corporation, USA.

<sup>8</sup>TR40-160 transient recorder, Licel, Germany.

<sup>9</sup>ROOT, An object-oriented data analysis framework. Available at: <http://root.cern.ch>

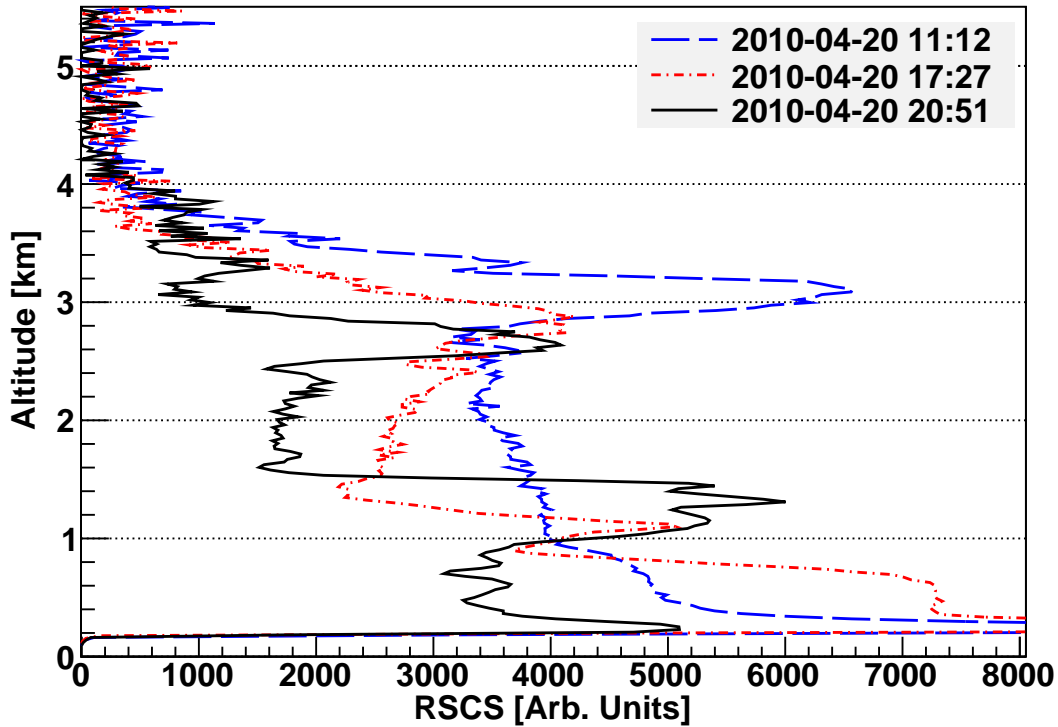


Figure 3.3: Range-square-corrected-signal (RSCS) vertical profiles obtained with the mobile lidar at Nova Gorica (107 m a.s.l.), Slovenia. Measurements show an elevated aerosol layer between 2.5–3.1 km a.s.l. on 20 April 2010, which decreased with time (from 3.1 km in the morning to 2.5 km in the evening) (He et al., 2010).

### 3.1.2 Validation of the mobile lidar system

The performance of the mobile lidar for aerosol tracking was validated in a multi-instrument measurement campaign (Gao et al., 2011b) of the volcanic ash from the Eyjafjallajökull volcano eruption, which was performed in Slovenia from 16 to 20 April 2010. The mobile lidar system was used as the main remote sensing detection tool to probe for the optical characteristics of ash, which was found to be streaming at relatively uniform altitude above the investigated region. In the measurements, only the infrared channel was used to minimize the molecular scattering.

On 20 April, one or more elevated aerosol layers in the low troposphere were observed at Nova Gorica throughout the day (Fig. 3.3). The upper elevated aerosol layer, located between 2.5–3.1 km a.s.l. was simultaneously detected by the stationary Mie lidar system at Otlica, around 20 km east of Nova Gorica. To validate remote sensing measurement results and to confirm the identity of the aerosols, an airborne mis-

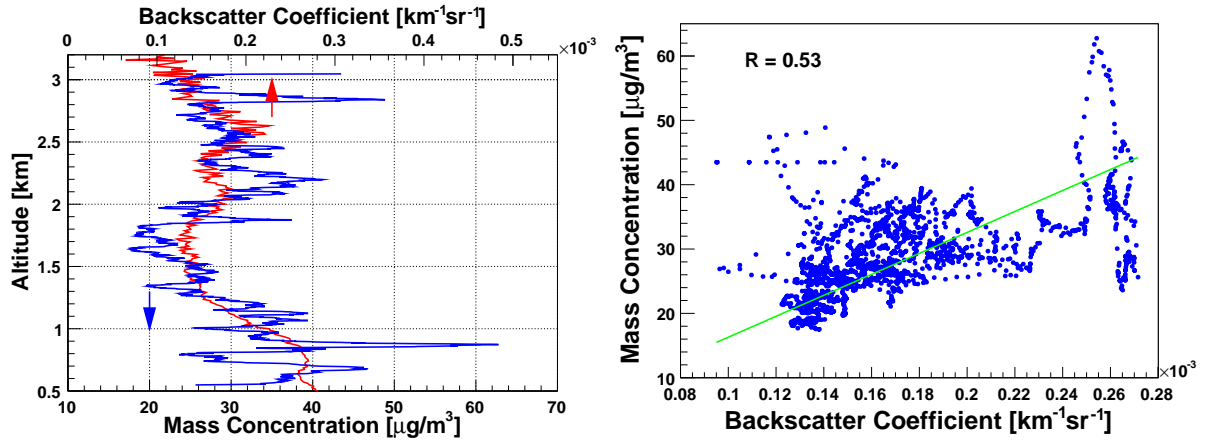


Figure 3.4: Total particle matter content from the airborne measurements and aerosol backscatter coefficient obtained by mobile lidar were found to be correlated. The correlation can be qualitatively seen from the overlap of both profiles simultaneously measured at 15:20 Central European Time on 20 April 2010 (top). The linear correlation coefficient was found to be 0.53 (bottom) (Gao et al., 2011b).

sion was carried out by Istituto Nazionale di Oceanografia e di Geofisica Sperimentale (Italy), about 40 km away from Nova Gorica. Subsequent chemical analysis of the airborne collected aerosol samples confirmed that aerosol layers contained volcanic ash particles. The concentration of aerosol particles with aerodynamic equivalent diameters up to  $10\text{ }\mu\text{m}$  ( $\text{PM}_{10}$ ) was measured throughout the spiral climb of the aircraft from 0.61 to 3.05 km using a laser particle counter<sup>10</sup>. Vertical profiles of the backscatter coefficient obtained from mobile lidar measurements and the total particle matter content from airborne measurements were found to be correlated with a correlation coefficient of 0.53 (Fig. 3.4). The comparison shows that the mobile lidar system has the capability to provide the data necessary to locate and quantify relative loading of aerosols in the atmosphere and to study their dynamics.

### 3.1.3 Detection in the fluorescence channel

Due to their potential harm, it is of great importance to be able to detect, trace and identify aerosols of biological origin from among a broad variety of other aerosols in the atmosphere. The mobile Mie-fluorescence lidar provides biological aerosol detection capability through the detection of the fluorescence of the amino-acid tryptophan, which is present in most substances of biological origin (Fig. 3.2). In order to estimate

<sup>10</sup>Lighthouse 3016 IAQ Particle Counter, Lighthouse Worldwide Solutions, USA

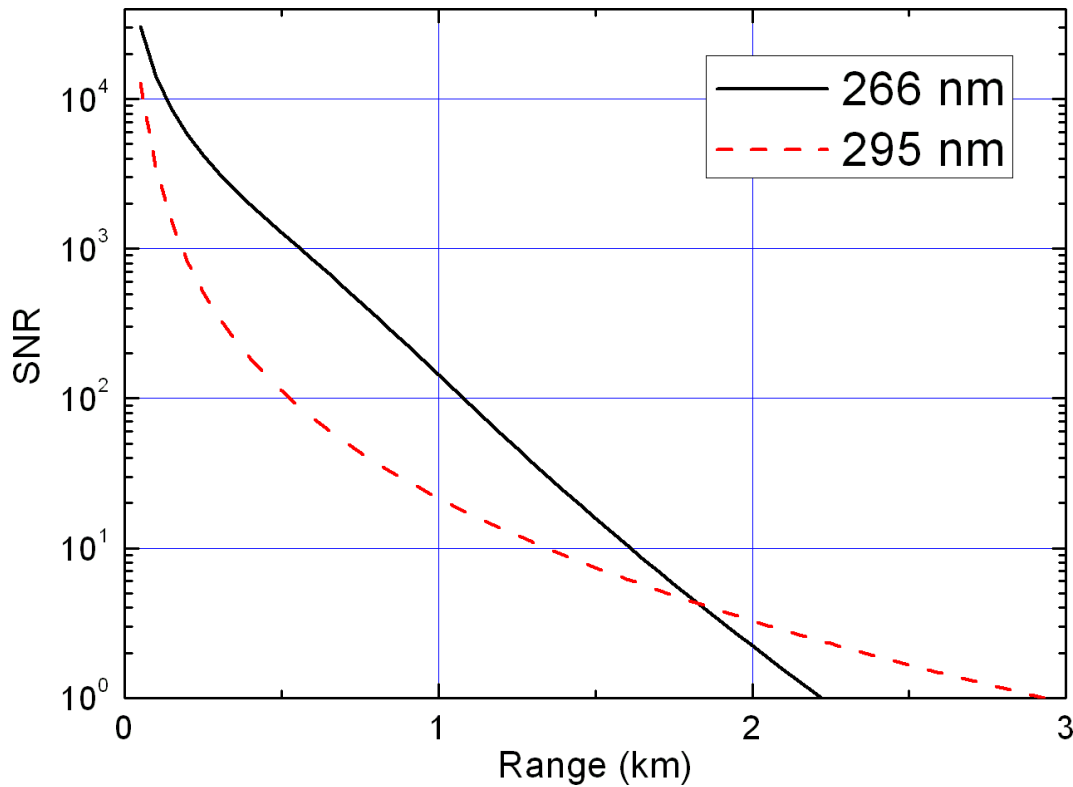


Figure 3.5: Simulated signal-to-noise ratio (SNR) of the lidar return signal in the fluorescent channel (295 nm) and the elastic channel at excited wavelength (266 nm). For a 15 s measurement along a single trace, the maximum detectable range of both UV channels (with SNR > 10) is about 1.5 km.

feasibility of biological aerosol identification, the maximum detectable range of both UV elastic (266 nm) and fluorescent (295 nm) channels has been numerically evaluated based on the corresponding signal-to-noise ratios (SNR). The computations include numerical generation of a plume of fluorescent particles in lidar's field of view that are hit by laser pulses.

For laser-induced fluorescence, finite relaxation effects of the laser-excited species should be taken into consideration. This leads to a very complex form of the lidar equation and to an optical depth dependence of the target media, detector integration period, and laser pulse shaper and duration. In the limit of large optical depth, the fluorescence lidar which was specifically developed, is identical to a fluorescent particle identifier instead of quantity of bioaerosol concentration (i.e. the information on the concentration of the fluorescent particles is lost). The energy of the fluorescence return

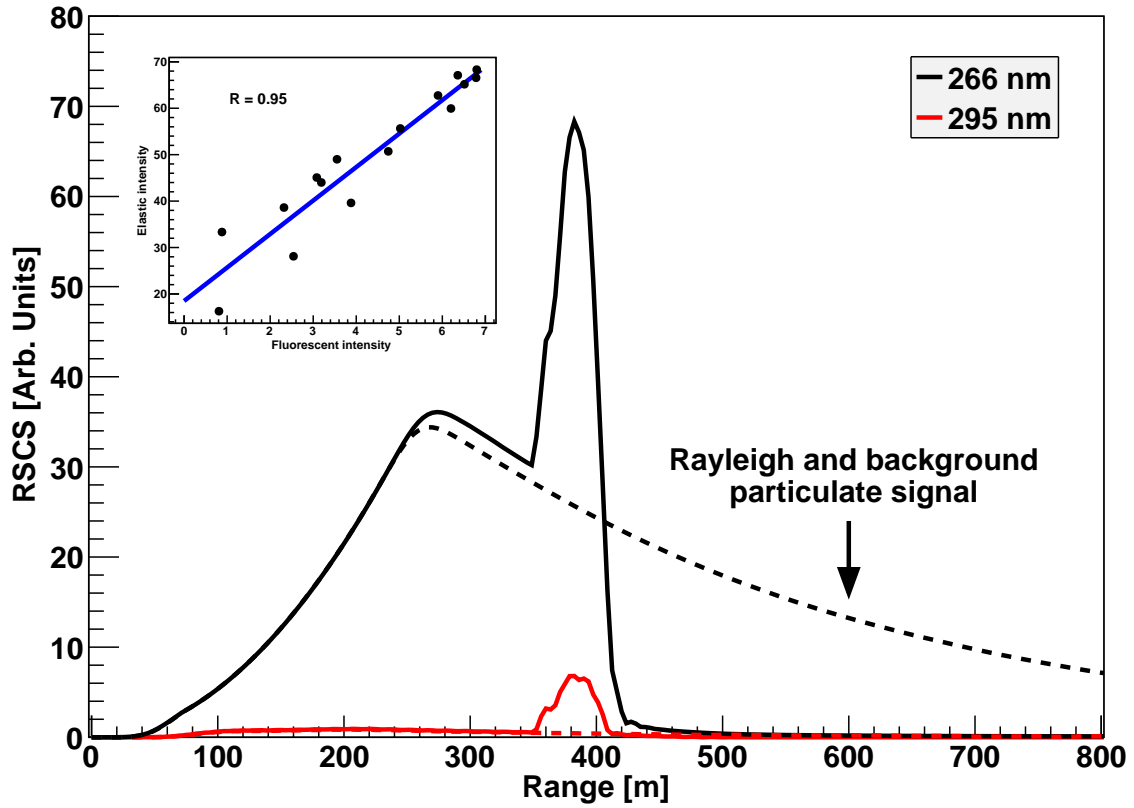


Figure 3.6: Range-square-corrected-signal profiles obtained with the mobile Mie-fluorescence lidar. Dash line represents the contribution from molecules and background particulates. In the laser-induced fluorescence detection, because the leaves block the laser beam, a sharp decrease was observed in the elastic signal at excited wavelength of 266 nm. The elastically backscattered signal was found to be related to the fluorescent signal within the range of presence of biological aerosols (between 350–410 m), with a correlation coefficient of 0.95 (inlaid figure).

signal as a function of range  $R$  can then be formally expressed as (Measures, 1988)

$$E(\lambda, R) = E_L \eta_F \frac{A_r}{R^2} \frac{c\tau}{2} \frac{\sigma(\lambda, \lambda_L)}{4\pi} N(R) \exp \left( - \int_0^R [\alpha_\lambda(r) + \alpha_{\lambda_L}(r)] dr \right), \quad (3.1)$$

where  $E_L$  is the energy of the laser pulse,  $\eta_F$  the fluorescence quantum efficiency,  $A_r$  the effective receiver area,  $c$  the speed of light,  $\tau$  the pulse duration,  $\sigma(\lambda, \lambda_L)$  the total cross-section for fluorescence at  $\lambda$  for incident radiation of wavelength  $\lambda_L$ ,  $N(R)$  the number density of laser-excited molecules, and  $\alpha_\lambda$  and  $\alpha_{\lambda_L}$  the volume extinction coefficients of the atmosphere and wavelengths  $\lambda$  and  $\lambda_L$ , respectively.

By assuming that error sources contributing to the uncertainty of the energy of the return signals are uncorrelated, signal-to-noise ratio (SNR) can be written as (Melchior,

1972)

$$\text{SNR}(r) = \frac{\sqrt{n}N_s(r)}{\sqrt{N_s(r) + 2(N_b + N_d)}} \quad (3.2)$$

where  $n$  is the number of pulses used in signal averaging,  $N_s(r)$  the total number of photons in the signal,  $N_b$  the background noise, and  $N_d$  the detector dark current. We further assumed that the laser intensity decreases only by Rayleigh-Mie scattering on aerosols and by absorption in molecules of air as it propagates through the atmosphere towards the generated fluorescent aerosol plume. Particle background is based on the U.S. standard atmospheric model ([U.S. Standard Atmosphere, 1976](#)). For 266 nm, the absorption is mainly due to the presence of ozone molecules ( $\text{O}_3$ ). Typical ozone concentration for populated areas applied in the calculation is  $50 \mu\text{g m}^{-3}$ . Figure 3.5 shows simulation results for the SNR of the UV channels. For a 15 s measurement along a single trace, the maximum detection range (with errors less than 10 %) is about 1.5 km. Based on this analysis, the system capability of biological aerosol identification from other particles in the plume which are solely elastic scatterers will be applicable, however, with a shorter detection range than simple aerosol mapping in the IR detection channel.

Preliminary characterization measurements were performed at Otlica observatory. The location is surrounded by an amount of trees, which are considered as fluorescent tracer materials. In the measurements, the Mie-fluorescence lidar was first pointing to the clear air, right above the height of the trees. Obtained elastically backscattered signals from both UV channels were considered as a base line for the tracer component. In order to induce the fluorescence, the lidar transmitter pulses then interrogate the regions of trees. The lidar returns were constructed in Fig. 3.6. In the fluorescent detection, because the leaves block the laser beam, they are seen as distinct drop formations in the elastic lidar return at excited wavelength. This allows to precisely determine the distance of the target from the lidar site (about 380 m away). However, it is impossible to obtain the information on the fully distribution of biological aerosols due to the strong extinction of the lidar signal. The elastically backscattered signal was found to be linearly related to the fluorescent signal within the range of presence of biological aerosols (between 350–410 m), with a correlation coefficient of 0.95. Although the capability of the system was not being fully tested with a simply experiment, which confirmed the feasibility of biological aerosol identification.





Figure 3.7: Stationary Mie lidar at Otlica observatory ( $45.93^\circ$  N,  $13.91^\circ$  E, 945 m a.s.l.), with an open view towards the southwest.

## 3.2 Stationary Mie lidar

The stationary Mie lidar is set up at the Otlica observatory of the University of Nova Gorica (UNG), above Ajdovščina, with an open view towards the southwest (Fig. 3.7). A high power *Q*-Switched pulsed Nd:YAG laser<sup>11</sup> is used as the transmitter, providing 100 mJ pulse energy at 4 ns width and a repetition rate of 20 Hz at 355 nm. Backscattered light is collected by a parabolic mirror with a diameter of 800 mm and focal length of 410 mm. The transmitter and the receiver are configured bi-axial. In the non-coaxial configuration of lidar system, the estimated complete overlap is from about 1000 m. In order to make the lidar system steerable, both of the transmitter and the receiver are mounted on a common frame which is adjustable in the elevation angle from  $-5^\circ$  to  $90^\circ$  using a step motor with  $0.1^\circ$  angular resolution.

---

<sup>11</sup>Brilliant B by Quantel, France.



Figure 3.8: The University of Iowa vehicle-mounted Mie lidar system.

The signal is detected by a Hamamatsu PMT (R7400). To suppress the background, an adjustable iris is placed at the focus of the mirror, moreover, a collimating lens and a 5 nm interference filter centered at 354.7 nm are used. With the present experimental setup, lidar measurements are usually performed during the night, as the daylight background is prohibitive. Data acquisition is performed using a Licel transient recorder (TR40-160) with 12-bit resolution at 40 MHz sampling rate in combination with our own C++ (Linux) based DAQ software.

### 3.3 Vehicle-mounted Mie lidar

The vehicle-mounted Mie lidar system (Fig. 3.8) was built by Professor William Eichinger from University of Iowa (UI), USA. The system mounted inside a dedicated vehicle, is capable of taking vertical aerosol measurements while in motion and recording the current position using built-in GPS receiver. A pulsed Nd:YAG laser<sup>12</sup> operating at the 1064 nm wavelength was used as the transmitter, providing ~25 mJ pulse energy with a repetition rate of 50 Hz. The laser was attached to a 254 mm, f/10, Cassegrain telescope<sup>13</sup> and the laser beam was emitted coaxially with the telescope.

<sup>12</sup>Big Sky CFR400 by Quantel, France.

<sup>13</sup>LX50, Meade Instruments Corp., USA

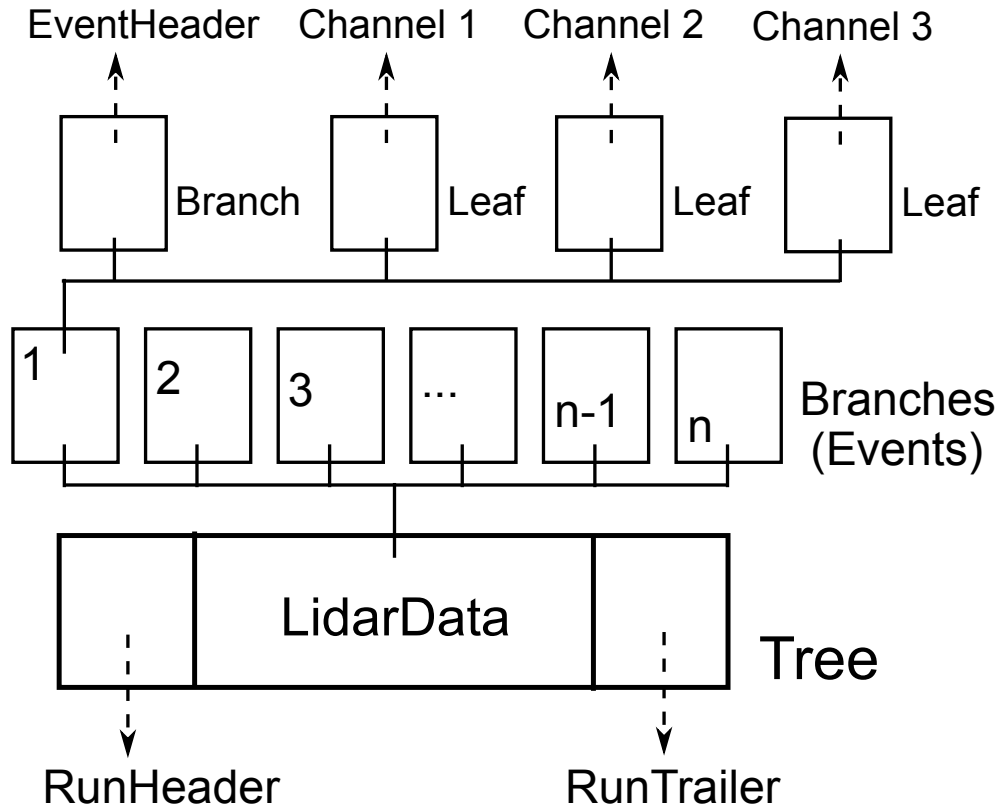


Figure 3.9: Schematic diagram of the data storage in ROOT objects. In the tree structure, successive lidar events are stored as a series of branches.

The backscattered signal was detected by an IR-enhanced Si-APD detector<sup>14</sup> and then digitized by a 100 MHz transient digitizer<sup>15</sup>, resulting a spatial resolution of 1.5 m.

### 3.4 Data structure of the UNG lidar systems

The DAQ software for both lidar systems at the University of Nova Gorica is written in the C++ programming language and based on the ROOT framework. Collected data is stored in ROOT binary files, which comprise two principal classes: `RunHeader` and `Event`. Class `RunHeader` contains basic information on the configuration and state of experiment, e.g. the number of operational channels, starting time, the laser power, the voltages of detectors, the total number of events and some comments, etc. `Event` class is used for the storage of the collected signal provided by all operating

<sup>14</sup>EG & G C30954/5E, URS Corp., USA.

<sup>15</sup>PDA12, Signatec Inc., USA

transient recorders. It provides access to time-dependent events with the number of laser shots and zenith and azimuth orientation information residing in data files. In the measurements, mobile lidar signals from 10 laser shots were average to an event, while stationary lidar signals from 20 shots, that both yield to 1 s temporal resolution.

Figure 3.9 illustrates the tree structure of the data. Successive lidar events are stored as a series of branches which can be read independently for further processing. Each event contains the data of all of the channels, as well as its own time stamp (class `EventHeader`). The access to the members of the class `Event` (i.e., the branches and the leaves), can be achieved through the shared library of `libEvent`.

### 3.5 Lidar equation and inversion methods

The lidar return signal along a single line of sight can be written as (Kovalev and Eichinger, 2004)

$$P(r) = CY(r) \frac{\beta(r)}{r^2} \exp \left[ -2 \int_0^r \alpha(r') dr' \right], \quad (3.3)$$

where  $P(r)$  is the received signal,  $C$  the lidar system constant including the losses in the transmitting and receiving optics and the effective receiver aperture,  $Y(r)$  the overlap function ( $0 \leq Y(r) \leq 1$ ),  $\beta$  the total (particulate and molecular) backscatter coefficient ( $\text{m}^{-1} \text{sr}^{-1}$ ), and  $\alpha$  the total extinction coefficient ( $\text{m}^{-1}$ ).

The overlap function  $Y(r)$  changes from zero to unity with the increase of the range  $r$ . In the areas close to the lidar, where the overlap of the collimated laser beam and the field of view of the receiver is incomplete, the value of  $Y(r)$  is less than 1. The maximum value of  $Y(r)$  is normalized to 1 in the complete overlap areas (usually starts from a few hundred meters). In present study, the lidar data obtained within the region of incomplete overlap where  $Y(r) < 1$  are discarded, because of the difficulties associated with the accurate overlap correction.

A difficulty for inversion of lidar equation (Eq. 3.3) is that there are more than one unknown ( $C$ ,  $\beta(r)$  and  $\alpha(r)$ ) in one equation. The indeterminacy of the solutions for lidar equation is one of the main challenges for lidar applications, which restricts practical applications of lidars for atmospheric study. One way to solve the underdetermined lidar equation, is the use of independent measurements of the unknown atmospheric parameters, which is rather challenging (e.g. Weinman, 1988; Hoff et al., 1996). A more common method is the use of a priori assumption about atmospheric properties along the lidar line of sight. Different approaches are presented in the following sections.

### 3.5.1 Slope method for a homogeneous atmosphere

By assuming that the examined atmosphere is homogeneous, a simple mathematical solution for Eq. 3.3 can be achievable for the extinction coefficient  $\alpha$ . For a valid homogeneous atmosphere, it has

$$\alpha(r) = \alpha = \text{const.} \quad (3.4)$$

and

$$\beta(r) = \beta = \text{const.} \quad (3.5)$$

The lidar  $S$ -function can then be defined as

$$S(r) = \ln [r^2 P(r)] = \ln(C\beta) - 2\alpha r. \quad (3.6)$$

The extinction coefficient  $\alpha$  can be determined as the slope of the least squares straight line fit to  $S(r)$  through the considered range (Collis, 1966). The standard deviation of the linear fit for  $S(r)$  can be used as estimator for the atmospheric heterogeneity.

### 3.5.2 Boundary point solution

The slope method can only be used to determine the mean extinction coefficient over an estimated range in a homogeneous atmosphere. To extract the extinction coefficient values along the lidar line of sight in an inhomogeneous atmosphere, an assumption of the backscatter to extinction ratio is made in general. In order to obtain quantitative extinction from lidar returns, the system constant  $C$  must also be determined. This is found by using reference values of  $\alpha(r_m)$  rather than through direct determination of the constant  $C$ . In other words, the knowledge of extinction coefficient  $\alpha(r_m)$  either at a local point or over a specified range of the atmosphere (so-called critical height or boundary point), is needed.

A remarkably stable solution was proposed by Klett (1981). The suggested boundary point is chosen close to the far end ( $r_m > r$ ) of the measurement range (so-called far-end solution). In practice, an accurate value of the local extinction coefficient  $\alpha(r_m)$  can be established at an aerosol-free region in which the extinction can be assumed to be purely molecular. Another way to determine the boundary condition  $\alpha(r_m)$  is using the slope method by assuming a homogeneous atmosphere over a restricted zone close to  $r_m$ .

The relationship between backscatter  $\beta$  and extinction  $\alpha$  coefficients can be ex-

pressed as a power law of the form (Curcio and Knestrick, 1958)

$$\beta = B\alpha^\kappa, \quad (3.7)$$

where factor  $B$  is taken as constant, exponent  $\kappa$  depends on the lidar wavelength and the aerosol properties,  $0.67 \leq \kappa \leq 1.0$ . With the relationship in Eq. 3.7, the lidar  $S$ -function (Eq. 3.6) can be re-written as

$$S(r) = \ln C + \kappa \ln \alpha(r) - 2 \int_0^r \alpha(r') dr'. \quad (3.8)$$

The corresponding differential equation

$$\frac{dS(r)}{dr} = \frac{\kappa}{\alpha(r)} \frac{d\alpha(r)}{dr} - 2\alpha(r), \quad (3.9)$$

is the Bernoulli equation, which exists an analytical solution. If  $\kappa$  is regarded as constant, the far-end solution for the lidar operating range  $r < r_m$  is (Klett, 1981)

$$\alpha(r) = \frac{\exp\{[S(r) - S(r_m)]/\kappa\}}{\alpha(r_m)^{-1} + \frac{2}{\kappa} \int_r^{r_m} \exp\{[S(r') - S(r_m)]/\kappa\} dr'}. \quad (3.10)$$

Light extinction in the atmosphere is caused by two basic components, molecules and particulates. In the case of a high aerosol concentration, the molecular component of the scattering can be ignored (Fujii and Fukuchi, 2005). When examining a clear atmosphere, the scattering from air molecules has to be considered. The lidar equation (Eq. 3.3) is then written in the form

$$P(r) = C \frac{\beta_p(r) + \beta_m(r)}{r^2} \exp\{-2 \int_0^r [\alpha_p(r') + \alpha_m(r')] dr'\}, \quad (3.11)$$

where  $\beta_p(r)$  and  $\beta_m(r)$  are the particulate and molecular backscatter coefficients and  $\alpha_p(r)$  and  $\alpha_m(r)$  are the particulate and molecular extinction coefficients, respectively. The procedure to solve the lidar equation (Eq. 3.11) for a two-component atmosphere was proposed by Fernald (1984). It is assumed that the molecular density profile is well known (computed from a standard atmosphere or determined from the meteorological data), and exploits a relation between the extinction and the backscatter coefficients.

As no significant molecular absorption exists at the lidar wavelengths, the molecular extinction-to-backscatter ratio reduces to a range-independent quantity, being de-



scribed by the expression (Eq. 2.6 in Sec. 2.2.1)

$$S_2 = \frac{\alpha_m(r)}{\beta_m(r)} = \frac{8\pi}{3}. \quad (3.12)$$

The particulate extinction-to-backscatter ratio (so-called lidar ratio) which can also be assumed as range independent, is defined as

$$S_1 = \frac{\alpha_p(r)}{\beta_p(r)}, \quad (3.13)$$

where  $S_1$  depends on the shape, size and other parameters of the particulate scatterers. Typical values for the lidar ratio are on a wide interval,  $10 \text{ sr} \leq S_1 \leq 100 \text{ sr}$ . The variation can be explained by analyzing the scattering direction as a function of particulate size. Scattering of light of small diameter particulates is almost isotropic, similar to the pure molecular scattering (Weitkamp, 2005). This results in the lidar ratio being similar to the molecular extinction-to-backscatter ratio ( $8\pi/3$ ). However, in the case of the higher aerosol diameter, forward peaked scattering is presented. Thus, the amount of light directed backwards is relatively low and the lidar ratio value is relatively high.

The solution for Eq. 3.11 is then written as (Fernald, 1984)

$$\alpha_p(r) = -\frac{S_1}{S_2}\alpha_m(r) + \frac{P(r)r^2 \exp \left[ 2\left(\frac{S_1}{S_2} - 1\right) \int_r^{r_m} \alpha_m(r') dr' \right]}{\frac{P(r_m)r_m^2}{\alpha_p(r_m) + \frac{S_1}{S_2}\alpha_m(r_m)} + 2 \int_r^{r_m} P(r')r'^2 \exp \left[ 2\left(\frac{S_1}{S_2} - 1\right) \int_{r'}^{r_m} \alpha_m(r'') dr'' \right] dr'}, \quad (3.14)$$

where  $r < r_m$ .

### 3.5.3 Multiangle method

The boundary point solution for lidar equation, can yield large uncertainties due to the selection of a boundary value and the assumption of the lidar ratio. The difficulties can be overcome with multiple angle measurement approaches. The multiangle method (Kano, 1968; Hamilton, 1969; Sicard et al., 2002; Filipčič et al., 2003) utilizes the dependence of the atmospheric attenuation on the elevation angle to obtain vertical extinction profiles based on the assumption of horizontal atmospheric homogeneity (i.e., the backscatter  $\beta$  is assumed to be uniform and invariant in horizontal layers). In general, scanning lidar is applied to obtain different elevation angle data. The lidar scans the atmosphere in many angular directions at a constant azimuth, starting from

horizontal direction, producing a two-dimensional image known as a range-height-indicator (RHI) scan.

Under the assumptions of a horizontally uniform atmosphere, the optical depth of the atmosphere can be found directly from lidar multiangle measurement. When zenith angle  $\phi$  is considered, the range dependent lidar  $S$ -function (Eq. 3.6) can be re-written in terms of height  $h$  and geometric factor  $\xi = 1/\cos \phi = \sec \phi$  as

$$S(h, \xi) = \ln C + \ln \beta(h, \xi) - 2\xi\tau(h, h_0), \quad (3.15)$$

where  $\tau(h, h_0) = \int_{h_0}^h \alpha(h') dh'$  is the vertical optical depth of the atmosphere between  $h_0$  and  $h$ . Considering lidar measurements at two different zenith angles  $\xi_1 = 1/\cos \phi_1$  and  $\xi_2 = 1/\cos \phi_2$  and height  $h$ , Eq. 3.15 can be solved for the optical depth,

$$\tau(h) = -\frac{1}{2} \frac{S(h, \xi_1) - S(h, \xi_2)}{\xi_1 - \xi_2}, \quad (3.16)$$

and the mean extinction coefficient of the fixed layer  $(h_0, h)$ ,

$$\bar{\alpha}(h) = -\frac{1}{2h} \frac{S(h, \xi_1) - S(h, \xi_2)}{\xi_1 - \xi_2}. \quad (3.17)$$

The local extinction coefficient can then be obtained by determining the increments in the optical depth for consecutive layers.

The optical depth is directly proportional to the difference of two  $S$ -function at the same height and different angles. Therefore, choosing a small separation between zenith angles,  $\xi_1 = \xi$  and  $\xi_2 = \xi + d\xi$ , a differential form of Eq. 3.16 can be written as

$$\tau(h) = -\frac{1}{2} \frac{\partial S}{\partial \xi} \Big|_h, \quad (3.18)$$

with  $S(h_0) = 0$  and  $\tau(h_0) = 0$ .

The necessary information can be obtained from a two-angle data set. However, due to a mere two-point approximation, substantial uncertainties in  $S(h, \xi)$  for single angle can yield a large retrieval uncertainty. When a large number of angular directions are used in multiangle measurements, the uncertainty that originates from random errors can be significantly reduced using a least-squares method. The optical depth  $\tau$  is then determined as the slope of the resulting linear function for  $S(h, \xi)$  in  $\xi$ . The linear fit also enables a well-separated angle in zenith, which has to be considered under different atmospheric conditions (i.e., clear or turbid), related to the horizontal



homogeneity assumption. The preferred horizontal invariance is not required to take place across huge atmospheric volumes, but has to be met only in relatively small arc of interest where the continuous lidar scan is performed.

### 3.6 Absolute calibration of the vertical scanning lidar

Scanning lidars are ideal tools for the study of atmospheric structure and the dynamics of ABL height, because of their fine spatial and temporal resolution. Range height indicator (RHI) scans are generally performed to indicate two-dimensional (2D) distributions of atmospheric aerosols. In such range-resolved measurements of particulate concentrations, small errors in the long range measurements can lead to large uncertainties in the quantities being measured. Atmospheric optical variables (vertical optical depth and extinction coefficient) can also be obtained from the data of the 2D RHI scan based on the multiangle method and under the assumption of horizontal atmospheric homogeneity. Inaccurate value of the zenith angle may influence the accuracy of the retrieval results.

In Cartesian 2D RHI scan, the height offset  $\Delta h$  (offset in vertical directions) and the distance offset  $\Delta d$  (offset in horizontal axis) are both affected by accuracies of the detection range  $r$  and the elevation angle  $\theta$  (Taylor, 1997),

$$(\Delta h)^2 = \left[ \frac{\partial(r \sin \theta)}{\partial r} \right]^2 (\Delta r)^2 + \left[ \frac{\partial(r \sin \theta)}{\partial \theta} \right]^2 (\Delta \theta)^2, \quad (3.19)$$

$$(\Delta d)^2 = \left[ \frac{\partial(r \cos \theta)}{\partial r} \right]^2 (\Delta r)^2 + \left[ \frac{\partial(r \cos \theta)}{\partial \theta} \right]^2 (\Delta \theta)^2. \quad (3.20)$$

For the lidar systems which have a detection range up to 40 km with range resolution of 3.75 m, both height offset  $\Delta h$  and distance offset  $\Delta d$  originating from the error of detection range  $\Delta r$  are considered to be negligible. The offset of the elevation angle behaves different, even a small error can produce large offset in both coordinates. It is necessary to calibrate the elevation angle for the scanning lidar before performing RHI scans.

In present study, the absolute calibration for the elevation angle of the scanning lidar were performed in two levels at Otlica observatory (945 m a.s.l.) to minimize the zero-line offset. The first level calibration was performed by an electronic level device<sup>16</sup>, in which the reference elevation angle ( $\theta = 0^\circ$ ) was roughly set. The second

<sup>16</sup>DNM 60L 24-in Digital Level, BOSCH, Germany.

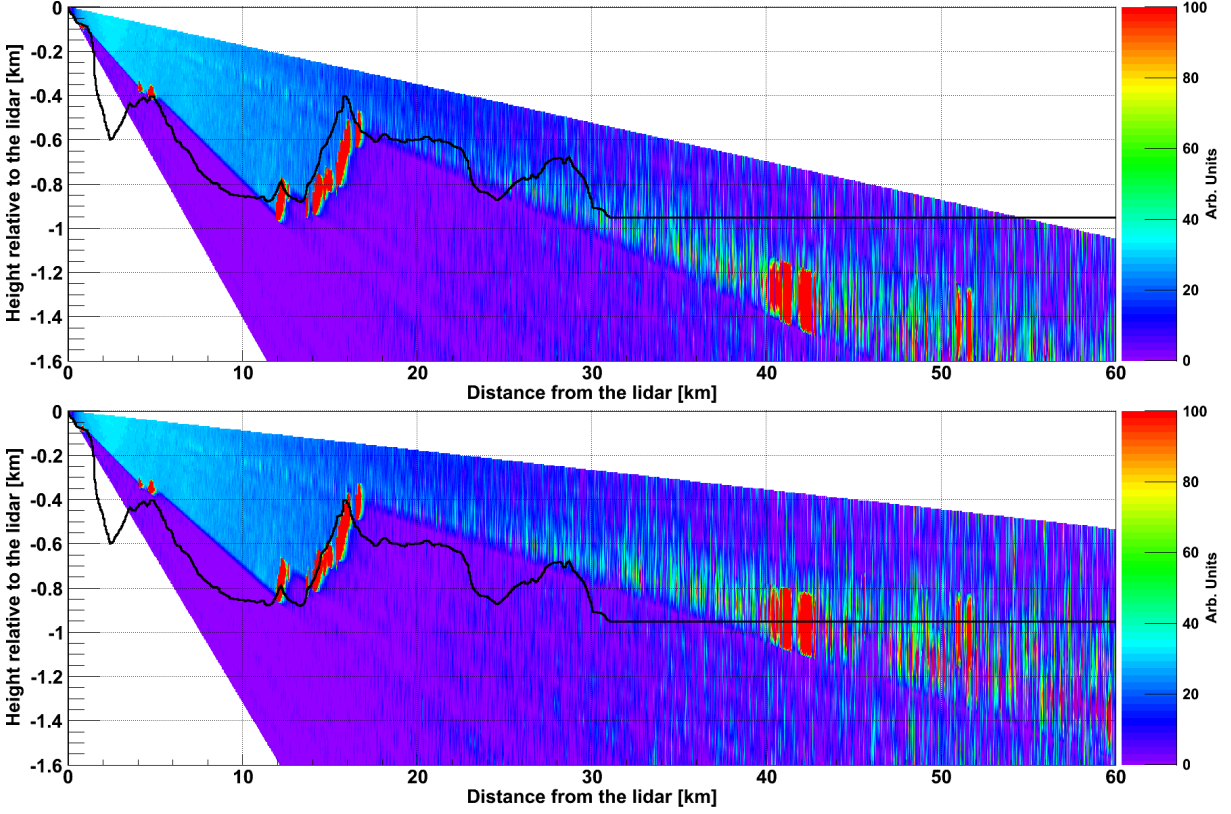


Figure 3.10: Exact absolute calibration of the elevation angle of the scanning lidar at Otlica (945 m a.s.l.) was performed through the comparison of topological terrain profile (black solid line) and the lidar returns. The top figure shows the returns before and the bottom after elevation angle adjustment of  $0.49^\circ$ .

level calibration was then performed through the comparison of the lidar returns and the topological terrain profile based on the information about the sea level (Fig. 3.10), in which the absolute calibration factor of the elevation angle was obtained.

The lidar was set to scan below the horizon, from the elevation angle of  $-8^\circ$  to  $-1^\circ$  with an angular step of  $0.2^\circ$ . Spatial distribution of the natural logarithm range-corrected lidar return signal ( $S$ -function) obtained by RHI scanning was presented by 2D Cartesian scans. To fill the pixels where no lidar data were available, a weighted value was reconstructed using a barycentric interpolation scheme (Min, 2004) between successive step profiles with a 5 m resolution of the Cartesian 2D grid. The weighted value  $w(x, y)$  was calculated as

$$w(x, y) = \frac{v(x_1, y_1)d_2 + v(x_2, y_2)d_1}{d_1 + d_2}, \quad (3.21)$$

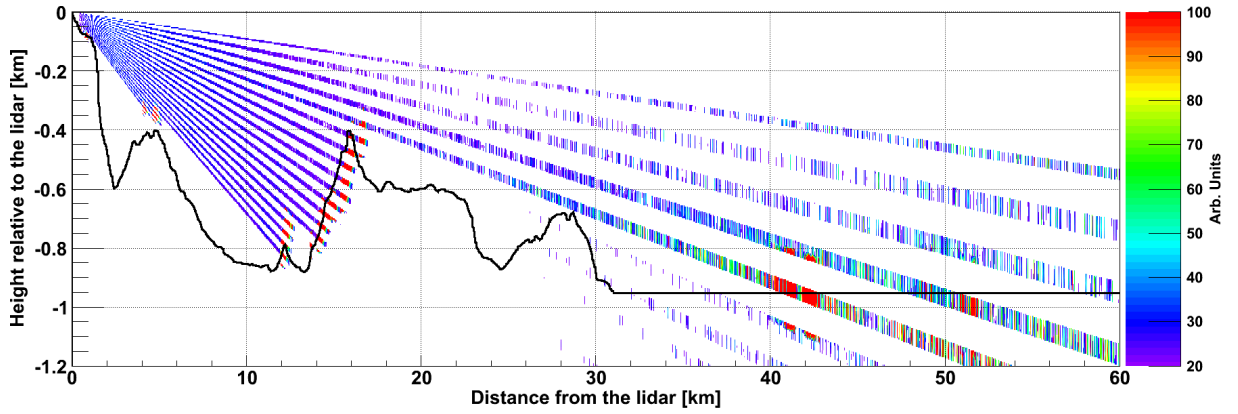


Figure 3.11: Scanning lidar returns with the limitation of the laser beam divergence.

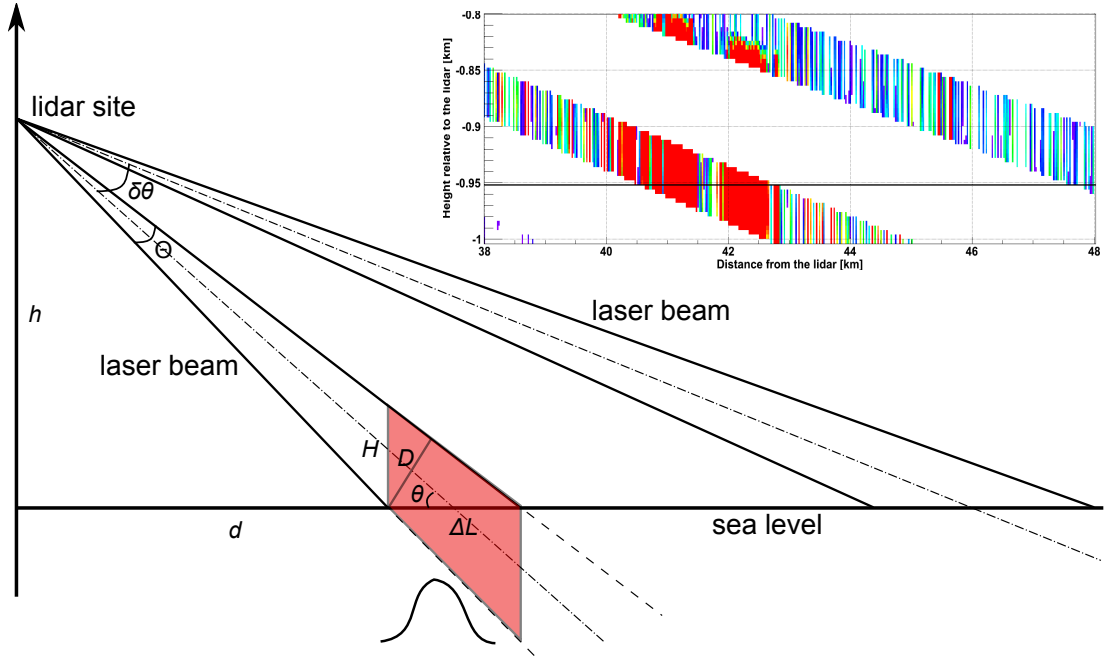


Figure 3.12: Schematic diagram of absolute calibration of vertical scanning lidar based on the sea surface. Red shadow denotes the constructed lidar returns from the reflection of the sea surface corresponding to Fig. 3.11, which is also illustrated in the inlaid figure.

where  $v(x_1, y_1)$  and  $v(x_2, y_2)$  are the measured values in successive step profiles,  $d_1$  and  $d_2$  are the shortest distances between the center of the pixel and the closest profiles on both sides.

Figure 3.10 demonstrates the constructed RHI scanning diagrams with the topological terrain profile along the line of lidar sight. A strong lidar return from the about

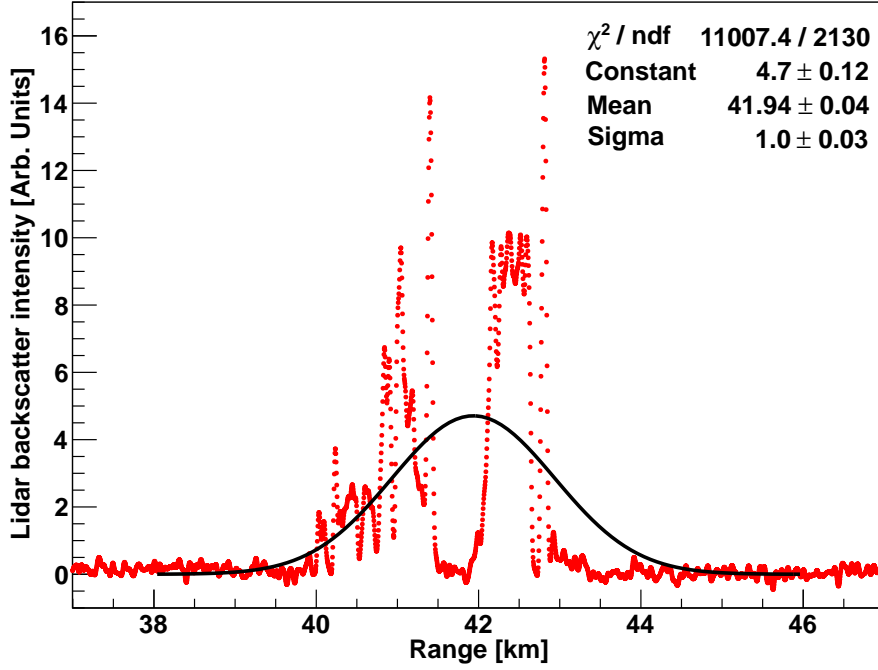


Figure 3.13: The Gaussian fit of lidar backscatter intensity in the measured range between 38 and 46 km at the elevation of  $-1.31^\circ$ .

42 km distant sea surface sea surface is clearly visible. The return is about 360 m offset in vertical coordinate with respect to the geodetic terrain profile, therefore, a second level calibration is needed. The angular offset of the elevation  $\Delta\theta$  can be then determined by

$$\Delta\theta = \arctan\left(\frac{\Delta h}{r}\right) = 0.49^\circ. \quad (3.22)$$

To further verify the obtained calibration factor, we have replotted the data in the RHI diagram of Fig. 3.10 to show the intensity of the backscattered signal as a function of range (Fig. 3.11). The plot contains only the data at discrete scanning angles with no interpolation between successive step profiles. Divergence of the laser beam as provided by the manufacturer is 1.2 mrad. Since the lidar signal decreases with distance as  $1/r^2$  (Eq. 3.3), angular calibration was performed using the lidar profile that reached the sea surface at the lowest elevation angle ( $\theta = -1.31^\circ$  in our case). The geometric principle for measuring the angular offset is shown in Fig. 3.12. Lidar return reflected from

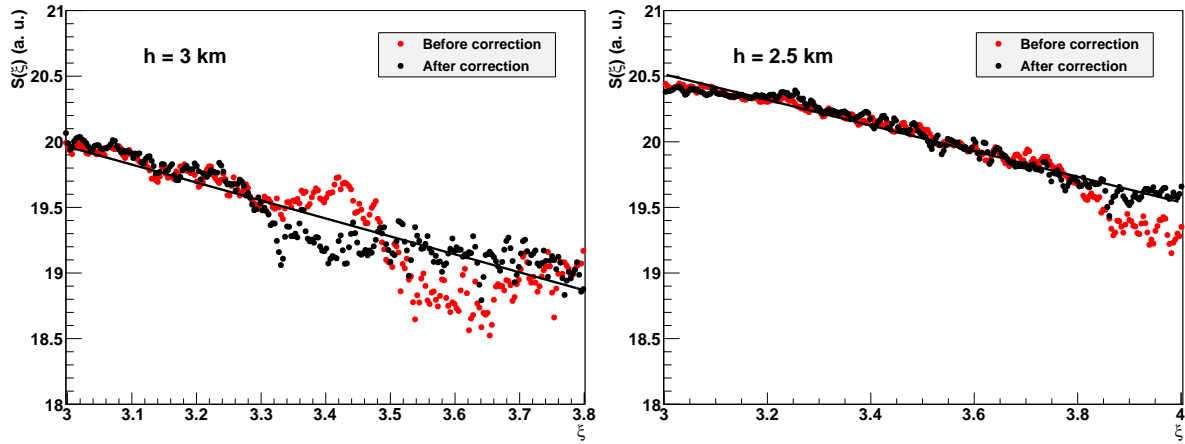


Figure 3.14: The comparison of the dependence of  $S$ -function values on zenith angle at the height of 3 km (left) and 2.5 km (right). Red points denote the values before and black points after angular correction.

the sea surface forms a triangle with a height  $H$  and base  $\Delta L$ , which can be derived as

$$H \approx D = \Theta r = 50.4 \text{ m}, \quad (3.23)$$

and

$$\Delta L = \frac{H}{\tan \theta} = 2.1 \text{ km}, \quad (3.24)$$

respectively, based on the parameters of angular resolution  $\delta\theta = 0.2^\circ$ , laser beam divergence  $\Theta = 1.2 \text{ mrad} = 0.07^\circ$ , and  $r \approx d = 42 \text{ km}$ . Note that the emitted beam diameter with a value of 7 mm is ignored here, which is rather small compared to that of the diameter at a range of 42 km. In ideal conditions, lateral distribution of laser pulse intensity should be Gaussian and we assume this to be true for our case. Gaussian fit of the lidar return was performed between the measured range interval 38 and 46 km at the elevation of  $-1.31^\circ$ , which results in mean value of  $41.94 \pm 0.04 \text{ km}$  with a standard deviation  $\sigma$  of  $1.0 \pm 0.03 \text{ km}$ , shown in Fig. 3.13. These parameters valid the calibrated angle of  $0.49^\circ$  and the correction results is presented in Fig. 3.10 (bottom).

Due to this small angular offset of the scanning lidar, the spatial difference in the near range between the 2D RHI diagrams with and without the angular correction may not be obvious (Fig. 3.10). The effects are more pronounced in the retrieval of atmospheric optical depth based on the multiangle method. Comparison of the dependence of  $S$ -function on zenith angle before and after the angular calibration at two different

heights is shown in Fig. 3.14. At both heights the linearity of  $S$ -function improves considerably after angular correction, which implies that for data analysis that require the assumption of horizontal atmospheric homogeneity, absolute angular calibration of the lidar is very important.

## Tracking of aerosols in urban environment

This chapter presents a number of case studies performed to investigate concentration and distribution of aerosols in urban areas. In particular, we present measuring campaigns performed over the neighboring towns of Nova Gorica, Slovenia and Gorizia, Italy (24 – 25 May 2010 and 30 – 31 January 2012) ([He et al., 2012a](#)), a campaign aimed at the studies of the ABL dynamics in Ljubljana, Slovenia (15 – 18 June 2012) and a study of vertical aerosol distributions within and around Iowa City, USA (9 – 10 August 2011) ([He et al., 2012b](#)).

### 4.1 Tracking of urban aerosols in Nova Gorica

On 24 and 25 May 2010, tracking of two-dimensional spatial and temporal aerosol distributions and aerosol emissions over the neighboring towns of Nova Gorica in Slovenia and Gorizia in Italy was performed using scanning elastic lidar, operating at 1064 nm.  $PM_{10}$  concentrations of particles,  $NO_x$  concentrations and meteorological data were continuously monitored within the lidar scanning region to complement the lidar results. Based on the collected data, several case studies were investigated, including the observation of the atmospheric structure and dynamics in the lower troposphere, the identification of aerosol point sources and the study of daily aerosol concentration cycles. In addition, a correlation study between the lidar-based and ground-based data was performed.

### 4.1.1 Geographic properties of the study area

The cities of Nova Gorica and Gorizia ( $45.96^{\circ}$  N,  $13.64^{\circ}$  E, 107 m a.s.l.), where the campaign was performed, are located in basin at the confluence of the Soča (Isonzo) and Vipava Rivers. From the north, they are sheltered from the direct influence of the alpine climate by an intermediate mountain range, from the west by the Goriška Brda (Collio) hills and from the southeast by the high Karst plateau, and are thus protected against the cold Bora wind, which affects most of the neighboring areas in the Slovenian littoral ([Alpers et al., 2007](#)), retaining mild Mediterranean climate throughout the year. In a typical anticyclonic situation, which was present during the campaign, there are generally mild breezes from E-NE in the nighttime and comparatively stronger winds in the daytime from the Adriatic Sea in the SW, which is about 20 km away. In an environment with very scarce precipitation from spring to late autumn ([Gasith and Resh, 1999](#)) and a presence of day-night wind reversal and basin-like terrain configuration, the risk of increased aerosol loading in urban settings is expected to be high, which calls for a systematic monitoring effort for quantitative estimation of concentration levels as well as spatial and temporal variability of aerosols. The present monitoring campaign was the first attempt in Slovenia to address this problem using a combination of remote sensing and ground-based monitoring.

### 4.1.2 Remote sensing

Remote sensing was performed using the scanning mobile lidar. The lidar was set up at an elevated site northeast from Nova Gorica (305 m a.s.l., 200 m above the basin ground), with clear horizontal visibility over the entire region of interest (Fig. 4.1). In this study, only the infrared channel was used to minimize the amount of molecular scattering relative to particulate scattering. The pulse energy was set to 40 mJ in order to prevent saturation of the receiver in the near field. As a result of the non-coaxial configuration of the transmitter and the receiver, the complete overlap region of the system starts from around 700 m. For the purpose of this study, lidar return signal was simply discarded in the first few hundred meters, where the overlap was not complete.

To observe two-dimensional temporal and spatial distributions of aerosols, two scan patterns were executed: range height indicator (RHI) scan and plane position indicator (PPI) scan. In RHI scan, the elevation angle was increased in  $1^{\circ}$  steps from  $4^{\circ}$  to  $45^{\circ}$  (covering a range of  $41^{\circ}$ ) at a constant azimuth angle of  $230^{\circ}$ . In PPI scan the elevation angle was set to zero and the azimuth angle was changed in  $2^{\circ}$  steps in counterclockwise direction from  $267^{\circ}$  to  $205^{\circ}$ , covering a range of  $62^{\circ}$ . At each step, 150





Figure 4.1: Top view of the scanning region (light-colored shadow) and the lidar site ( $45.96^\circ$  N,  $13.64^\circ$  E, 305 m a.s.l., 200 m above the town).  $\text{PM}_{10}$ ,  $\text{NO}_x$  and meteorological data were monitored at the ground level. Red points denote the locations of the identified aerosol sources and the yellow line the border between Slovenia and Italy.

laser shots were averaged and each scan took approximately 8 min to complete.

The lidar return signal along a single line of sight can be modeled (Collis and Russell, 1976) as

$$P(r) = \frac{C\beta(r)}{r^2} \exp \left[ -2 \int_0^r \alpha(r') dr' \right], \quad (4.1)$$

where  $P(r)$  is the received signal,  $C$  the lidar system constant including the losses in the transmitting and receiving optics and the effective receiver aperture,  $\beta$  the volume backscatter ( $\text{m}^{-1} \text{sr}^{-1}$ ), and  $\alpha$  the extinction coefficient ( $\text{m}^{-1}$ ). Raw data were normalized to the laser energy, and the flat baseline of each return, which is proportional to the intensity of background noise, was subtracted. Background noise was defined as an average of data points sampled at the far end of the trace. Each lidar return was then corrected for inverse range-squared dependence (Measures, 1988). To improve

the signal-to-noise ratio, a five-point gliding type radial basis spatial filter algorithm with weights given by Pascal's triangle was employed. Maximum detectable range with signal-to-noise ratio larger than one was then found to be about 5 km. Spatial distribution of the range-corrected lidar return signal obtained by both RHI and PPI scanning was presented by Cartesian 2D scans. To fill the pixels where no lidar data were available, a weighted value was reconstructed using a barycentric interpolation scheme (Min, 2004) between successive step profiles with a 5 m resolution of the Cartesian 2D grid.

To be able to normalize lidar return signals to aerosol concentrations, they need to be transformed into atmospheric extinction profiles. In urban areas, Klett solution (Klett, 1981) of the vertical extinction profile can be highly erroneous because of the relatively large uncertainty of the extinction-to-backscatter ratio (so-called lidar ratio). The multiangle method (Filipčič et al., 2003) is a possible way to obtain vertical extinction profiles from different elevation angle data obtained by scanning lidar under the assumption of horizontal atmospheric homogeneity and without the need to select specific lidar ratio. As the atmospheric boundary layer over urban areas is generally turbulent and heterogeneous (Spinhirne et al., 1980; Kovalev and Eichinger, 2004), this method is rarely used due to the inaccuracy of the horizontal atmospheric homogeneity assumption along any single trace. However, as aerosol fluctuations in horizontal directions are mostly random, lidar return data averaged over the entire horizontal scan do allow for a relatively accurate calculation of spatially-averaged aerosol extinction at a specific height.

As the lidar operated in the infrared part of the spectrum, the contribution from molecular scattering to extinction and backscatter coefficients was considered to be negligible. Effects of atmospheric inhomogeneities on the aerosol extinction coefficient  $\alpha$  (which may be caused by localized pollution sources and meteorological conditions) were minimized by using the average of the lidar  $S$ -function,

$$\bar{S}(r) = \langle \ln [r^2(P(r) - P_{bg})] \rangle = \ln(C\beta) - 2\alpha r, \quad (4.2)$$

over each horizontal PPI scan in the deconvolution process, where  $P_{bg}$  represents the intensity of the background noise. In the averaging, directions with apparent nonlinear data (e.g. with the presence of point sources) were excluded. Horizontal atmospheric extinction coefficient at a specific height was obtained using the slope method (Collis, 1966), as the slope of the least squares straight line fit to  $\bar{S}(r)$  through the considered range (Fig. 4.2). The deviations of atmospheric extinction coefficient  $\alpha$  from linearity

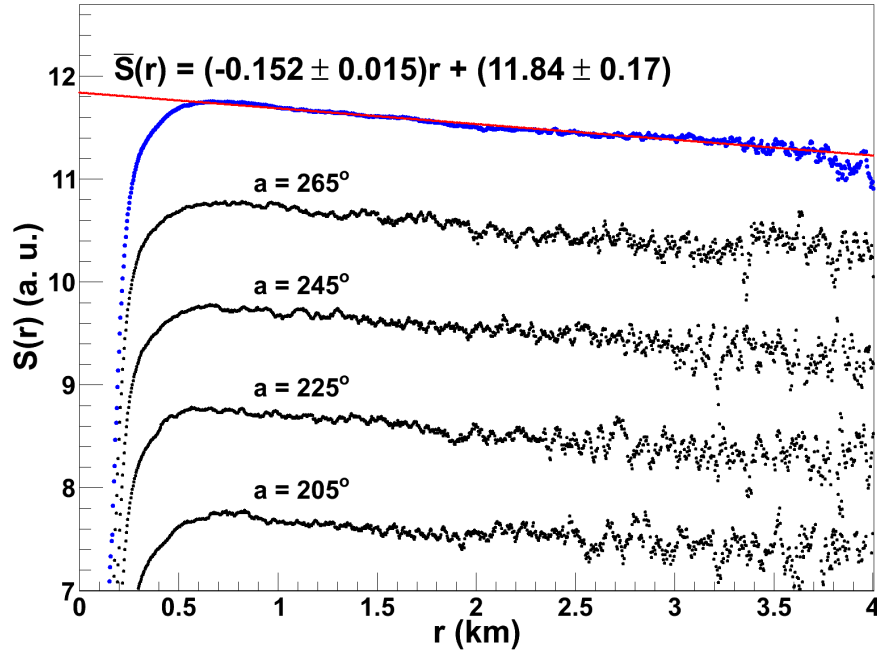


Figure 4.2: Averaged  $S$ -function for different horizontal directions over the PPI scan performed at 11:54 CET on 25 May 2010, with apparent nonlinear data excluded. The line  $\bar{S}(r) = (-0.152 \pm 0.015)r + (11.84 \pm 0.17)$  is a result of least squares linear fit in the range between 0.8 and 3.5 km, yielding a correlation coefficient of 0.94. The resulting horizontal atmospheric extinction coefficient  $\alpha$  is  $0.076 \text{ km}^{-1}$ , with relative error of about 0.1 due to atmospheric inhomogeneity.  $S$ -functions with azimuthal angles of  $265^\circ$ ,  $245^\circ$ ,  $225^\circ$ , and  $205^\circ$  are also shown with an incremental shift minus one from the averaged value.

are a suitable criterion for the detection of the extent of horizontal heterogeneity of the atmosphere and thus can be used as an estimator for the quality of the retrieved data.

The total uncertainty mainly related to the lidar-based measurement of aerosol extinction coefficient arose from three major sources: the uncertainty of the system constant factor  $C$ , the error in the background  $P_{\text{bg}}$  subtraction, and the horizontal atmospheric inhomogeneity (Eq. 4.2). The contribution of the system constant uncertainty for the case of thermally stabilized lidar return detection system is typically less than 0.05 (e.g. PerkinElmer, 2012). Relative uncertainty arising from background subtraction is related to the signal-to-noise ratio of the lidar system. As the lidar signal decreases with distance as  $1/r^2$  (Eq. 4.1), this uncertainty tends to be smaller closer to the lidar site and greater further away from the lidar. In our case, the deviation of background noise was 0.12 mV out of approximately 5 mV at the range of 3.5 km. The uncertainty from background noise subtraction was on average found to be 0.03. Dom-

inant contribution to the total uncertainty of the measurement was due to horizontal atmospheric inhomogeneities. These were estimated by considering the nonlinearity of the lidar  $S$ -function signal  $S(r)$  for horizontal traces with different azimuth angles at a fixed distance from the lidar site (e.g. azimuthal nonlinearity), and the nonlinearity of the averaged  $S$ -function signal  $\bar{S}(r)$  within the considered range, where the apparently nonlinear traces (less than 10 % of the full scan) were excluded from the calculation. The upper limits on azimuthal nonlinearities were calculated at the distance of 3.5 km from the lidar site, which was chosen to maximize the effects of heterogeneity due to geometrical distance between successive azimuthal profiles. Total relative uncertainty due to horizontal inhomogeneity was estimated to be less than 0.2. These three uncertainties are assumed to be statistically independent; a total relative uncertainty of aerosol extinction coefficient was estimated to be less than 0.21. Another possible source of uncertainty, which was not explicitly accounted for in this study, is the variability of the lidar ratio over the scanning area; it was however minimized by excluding lidar data traces with apparently non-linear behavior (distinct point sources) of the averaged  $S$ -function (Fig. 4.2).

### 4.1.3 Ground-based measurements

Due to the elevated risk of increased aerosol loading in Nova Gorica region, the concentration of  $PM_{10}$  particles is being continuously monitored by the Slovenian Environmental Agency. The monitoring site is located within the scanning area in a vicinity of a busy road in Nova Gorica (Fig. 4.1). True mass concentrations were provided by an ambient particulate monitor<sup>1</sup>, positioned 2 m above the ground. In addition,  $NO_x$  concentrations and meteorological data (wind speed and direction 10 m above the ground, temperature and relative humidity 2 m above the ground) were also collected at the same site. All ground-based data were averaged every hour except for the wind speed and direction, which were averaged every half an hour.

### 4.1.4 Structure of lower troposphere

In the daytime and under unstable, windy conditions, the lower troposphere is usually well mixed due to convection or vertical wind shear. On the other hand, in stable atmospheric conditions some horizontally stratified layers can be formed, especially during the night. In our case study we used vertical RHI scans to reveal vertical distribution

---

<sup>1</sup>TEOM series 1400a ambient particulate monitor, Thermo Electron Corporation, USA.



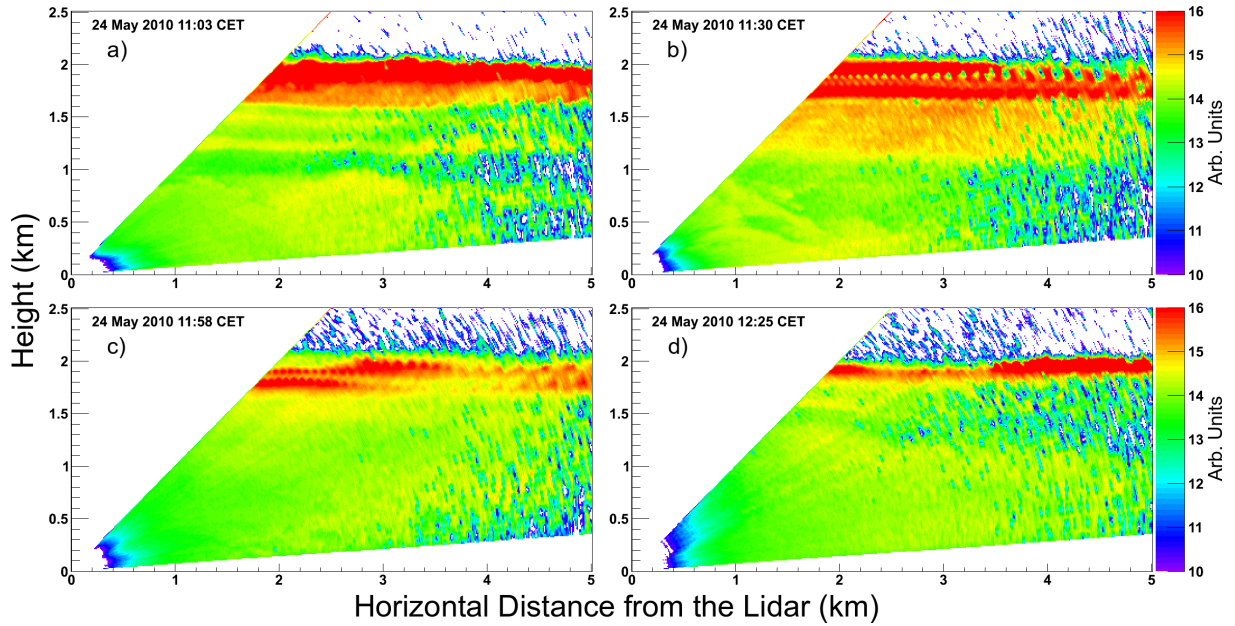


Figure 4.3: Time series of vertical RHI scans showing the logarithm of the range-corrected lidar signal for elevation angles from  $4^\circ$  to  $45^\circ$  with angular step of  $1^\circ$ . The scans were performed between 11:00 and 12:30 CET on 24 May 2010. The presence of a lower layer of clouds can be seen throughout the scanning period at the altitude of 2 km, relative to the lidar site. Above 2 km, lidar signal is effectively blocked by the clouds.

of aerosols in the lower troposphere. The main purpose of the case study was to investigate the transition from the horizontally stratified lower troposphere formed during the night to well mixed lower troposphere due to the increased thermal convection during the daytime. An example of temporal development of vertical structure of the lower troposphere, illustrated by a series of RHI scans performed from 11:00 to 12:30 Central European Time (CET) on 24 May 2010, is shown in Fig. 4.3. At 11:03, lower troposphere was still horizontally stratified (Fig. 4.3 a), and several optically thin aerosol layers can be seen up to 1.6 km above the lidar site. At the height of about 2 km, a layer of low level clouds was also present. In the next one and a half hour (Fig. 4.3 b–d), increased solar radiation caused the low clouds to slowly diminish and therefore more solar radiation reached the surface. Solar heating of the surface and consequential heating of the air at the surface intensified thermal convection and mixing of the air in the lower troposphere, which caused the degradation of the stratified layers. The effect of the heating was additionally confirmed by an evident increase of air temperature and the increase in wind speed (Fig. 4.4 a) in the period between 11:00 and 12:30. The described turbulent atmospheric conditions due to changing structure of

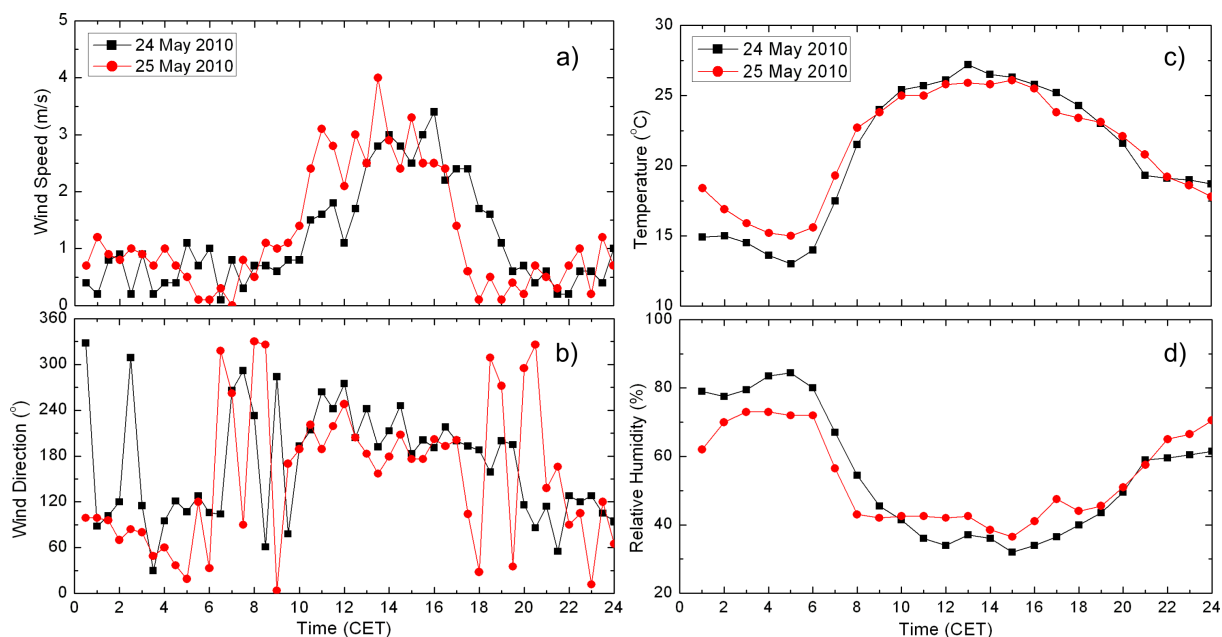


Figure 4.4: Meteorological data for Nova Gorica from 24–25 May 2010. Wind information was obtained 10 m above the ground and the temperature and relative humidity 2 m above the ground.

the lower troposphere are expected to be the main contribution to the uncertainty of the horizontal aerosol extinction coefficient (Fig. 4.7), whose relative errors during this period increased for about 50 %, with respect to earlier and later measurements.

#### 4.1.5 Identification of aerosol sources

In urban areas, main aerosol sources are expected to be localized exhausts from industrial and domestic emissions and traffic along the roadways. Individual aerosol emissions can not be distinctly visible in the single point ground-based  $\text{PM}_{10}$  and  $\text{NO}_x$  monitoring data because of spatial and temporal averaging; however, time series of the remote sensing scanning data can reveal the exact locations of the sources and complex dispersion paths of the plumes. We attempted to identify aerosol sources from the spatial distribution of the logarithm of the range-corrected lidar return signal in the horizontal PPI scans.

During the lidar campaign, a total of eight distinct cases of localized increases of lidar return were observed, all of them in the industrial area northwest of Nova Gorica. Using the range and azimuth information from horizontal PPI scans, these cases were found to appear at four different locations (Fig. 4.1) with polar coordinates of

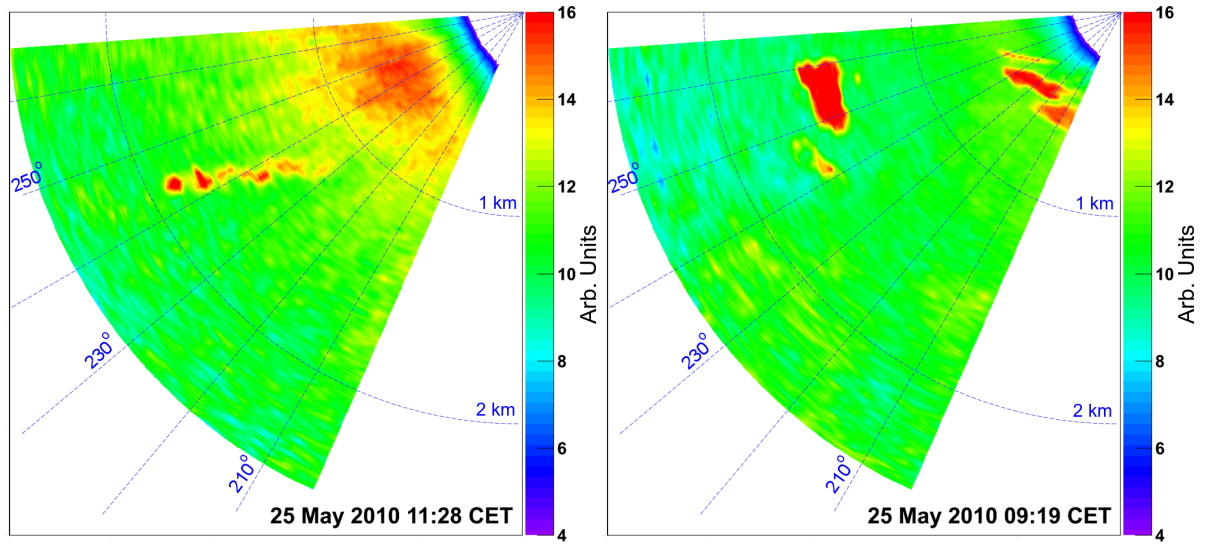


Figure 4.5: Two examples of horizontal PPI sector scans showing the logarithm of the range-corrected lidar signal (performed at 09:19 and 11:28 CET on 25 May 2010) show localized increases of lidar return corresponding to aerosol emission sources (B) and (D). In the later scan, the dispersion of the plume (D) towards the NE due to the increased wind speed can be clearly seen.

$A = [1.7 \text{ km}, 265^\circ]$ ,  $B = [1.55 \text{ km}, 262^\circ]$ ,  $C = [1.7 \text{ km}, 258^\circ]$  and  $D = [1.8 \text{ km}, 245^\circ]$ , with respect to the lidar site. After visual inspection of these locations in the field, they were confirmed to be major industrial aerosol sources, namely processing plants (A) and (D), lime production plant (B) and a foundry (C). In most cases, the plume emitted from these sources was found to spread towards inhabited areas.

Examples of aerosol emissions from sources (B) and (D) can be seen in horizontal PPI sector scans performed at 09:19 and 11:28 on 25 May 2010 (Fig. 4.5), where both show localized increases of lidar return. In the scan taken at 09:19 in calm wind conditions, the increased lidar return was found to be localized above the source (B) only. In the scan at 11:28, the plume from the source (D) was found to be carried in a relatively straight line towards the north-east for about 800 m due to the emerging south-western wind (Fig. 4.4 b), after which it disappeared (either blended in with background aerosols or rose above the scanning plane). Based on the logarithmic velocity law (Garratt, 1992), rapid dispersal of the plume can be explained by the presence of a stronger wind around the lidar scanning height.

### 4.1.6 Daily aerosol cycles

In urban areas, aerosol concentration levels were found to be strongly related to human activities, which result in the appearance of prominent features in daily aerosol cycles. These cycles are clearly visible in ground-based  $\text{PM}_{10}$  and  $\text{NO}_x$  monitoring data (e.g. [Harrison et al., 1999](#)). Daily variations of  $\text{PM}_{10}$  and  $\text{NO}_x$  in Nova Gorica from 24–25 May 2010 are shown in Fig. 4.6. The increase in both  $\text{PM}_{10}$  and  $\text{NO}_x$  concentration levels, peaking at around 08:00, was found to be present not only on these two days, but as a rule in the long-term data and can be related to the traffic emissions in the morning rush hours. In addition to the exhaust emissions, road dust picked up and injected into the boundary layer by vehicles may also be responsible for the concentration increase (e.g. [Eichinger et al., 1994](#)). The  $\text{NO}_x$  concentration had an apparent low in the afternoon, while the  $\text{PM}_{10}$  increased and reached a plateau at around 17:00. A local  $\text{NO}_x$  peak observed at around 21:00 was found to appear regularly in the Nova Gorica long-baseline environmental monitoring data and can be related to human activities. As the ground-based measurements were performed near a busy road and the largest shopping area in this region, the elevated  $\text{NO}_x$  concentrations are assumed to be due to the traffic, especially as they decrease after the closure of the stores. Relatively low and constant concentrations of both  $\text{PM}_{10}$  and  $\text{NO}_x$  during the night are expected to be the result of significantly reduced traffic and the absence of strong localized nighttime sources outside the winter season.

In the lidar monitoring campaign, scanning measurements were performed from 09:00 to 16:00 on 24 May 2010 and from 09:00 to 18:00 on 25 May 2010. The late morning increase of aerosol concentrations over the entire area is visible from temporal evolution of lidar-derived aerosol extinction, obtained from horizontal PPI scans 200 m above the ground (Fig. 4.7). Despite the fact that aerosol extinction is due to scattering on particulate matter and should therefore follow more or less the same daily pattern, several differences were found. There was a rapid decrease of aerosol concentration at the ground level after 10:00 due to the decrease of traffic intensity and the increase of the southwestern updraft wind speed (Fig. 4.4 a), which was not observed in the scanning data. We expect this to be due to basin-like terrain configuration, so that the aerosols remained contained and were present at the lidar scanning height. On 25 May, a second peak in aerosol extinction was observed after 16:00, when solar radiation and wind speed (Fig. 4.4 a) simultaneously decreased, which indicates an increase of the amount of accumulated aerosols during such conditions. The decrease of aerosol extinction between 13:00–16:00 was not observed in the  $\text{PM}_{10}$  measurements, which



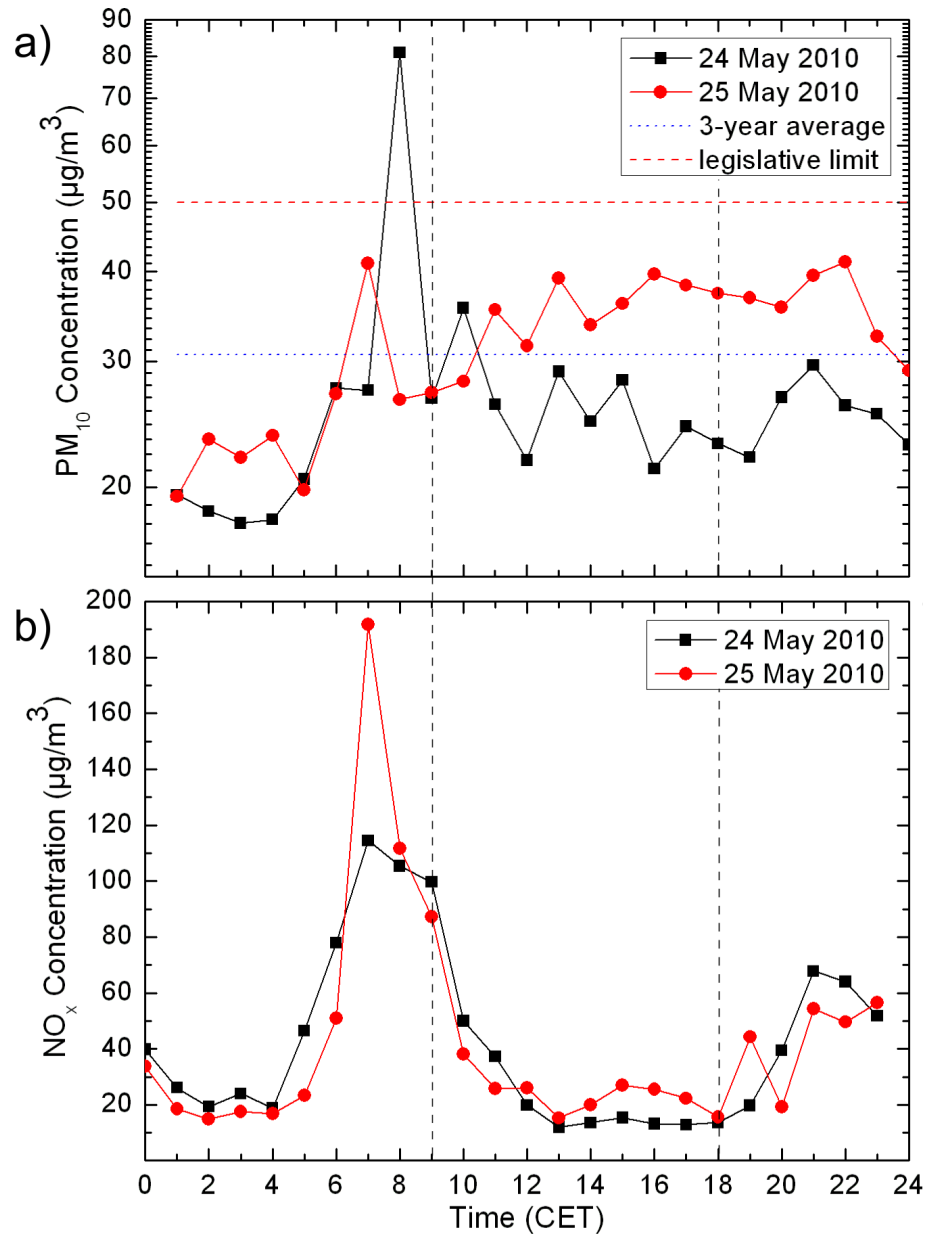


Figure 4.6: Temporal evolution of  $\text{PM}_{10}$  and  $\text{NO}_x$  concentrations for the period of 24–25 May 2010, obtained from the ground-based measurements at the monitoring station in Nova Gorica. The intervals when lidar measurements are available are marked with vertical dashed lines.

were more or less constant. In such a case, we expect the aerosol extinction decrease to be due, at least in part, to the increased water evaporation from hygroscopic aerosols (e.g. [Lewandowski et al., 2010](#)) during the daily temperature maximum (Fig. 4.4 c). Another reason for the decrease could be that in this period the convection was the

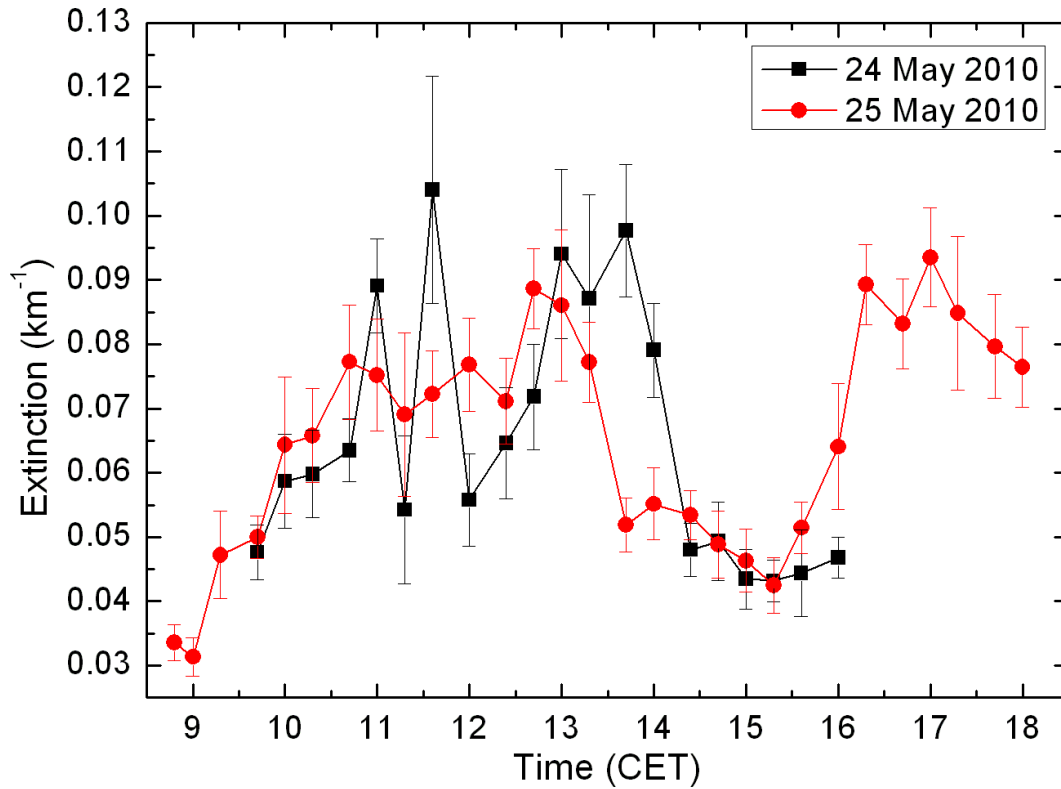


Figure 4.7: Temporal evolution of lidar-derived aerosol extinction coefficients over the entire scanning area (with point sources excluded), 200 m above the town from 09:00 to 16:00 CET on 24 May 2010 and from 09:00 to 18:00 CET on 25 May 2010.

strongest. The resulting mixing of air masses and the increase of the boundary layer height would decrease aerosol concentrations in the entire Nova Gorica basin, including at the lidar scanning height.

#### 4.1.7 Correlation between aerosol extinction and $PM_{10}$ concentration

As the aerosol extinction is a result of Mie scattering on particulate matter in the atmosphere, it is expected to be highly correlated to particle concentrations and to depend on the size of the scatterers, which was experimentally confirmed in several studies (e.g. [Del Gusta and Marini, 2000](#); [Lagrosas et al., 2005](#)).

In our case study, in the absence of the data regarding the distribution of aerosol size, a simple comparison of lidar-based horizontal atmospheric extinction and ground-based  $PM_{10}$  concentration was made. In addition to the unknown aerosol size distribution, another major source of uncertainties was expected to originate from dif-

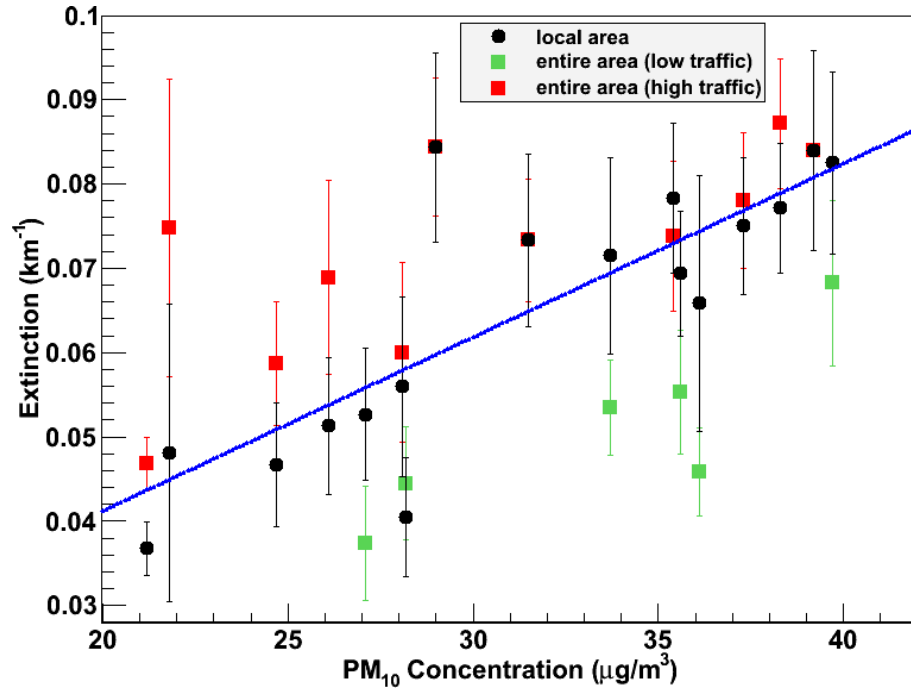


Figure 4.8: The correlation between the lidar-derived extinction and the  $\text{PM}_{10}$  concentration. The extinction for the entire dataset (black points) in a localized area with a radius  $R \leq 300$  m directly above the ground-based measurement site was found to be related to the  $\text{PM}_{10}$  concentration with a correlation coefficient of 0.84 and a slope of  $0.002 \pm 0.00007 \text{ m}^3 \text{ km}^{-1} \mu\text{g}^{-1}$  (blue line). Red points (correlation coefficient 0.72) represent the extinction values averaged over the entire scanning area for intervals of high traffic and green points (correlation coefficient 0.86) for periods of low traffic. In the fits, aerosol extinction was constrained to zero for the limit case, when  $\text{PM}_{10}$  concentration was zero.

ferent locations of the measurements, as lidar measurements were performed at 200 m above the ground, while  $\text{PM}_{10}$  concentration was measured at the ground level. The correlation between aerosol extinction ( $\alpha$ ) and  $\text{PM}_{10}$  concentration ( $c$ ) was investigated using hourly averaged data. When limiting the lidar scanning area to a circle with a radius  $R \leq 300$  m directly above the ground-based measurement site, the correlation was found to be linear with a slope of  $\alpha = (0.002 \pm 0.00007) c$  and a correlation coefficient of 0.84 for the entire dataset (Fig. 4.8). Based on the assumption that aerosols with diameters up to  $10 \mu\text{m}$  are the main scatterers (e.g. Birmili et al., 2010), the extinction in the fit was constrained to zero for the limit case, when  $\text{PM}_{10}$  concentration was zero. In the case of an unconstrained linear fit, the constant term was also found to be consistent with zero.

Due to the basin-like terrain configuration and relatively quiet meteorological con-

ditions, hourly averaged horizontal aerosol extinctions over the entire scanning area were expected to be correlated with the  $\text{PM}_{10}$  concentration as well and are included in the Fig. 4.8 as square-shaped red and green markers. The correlation coefficient for the entire dataset was found to be 0.4. Detailed investigation of traffic conditions for the apparently non-correlated values with lower extinction (green markers) revealed that they represent those measurements between 13:00 and 16:00, when the traffic was low ( $\text{NO}_x$  concentrations were below  $27 \mu\text{g m}^{-3}$ ). Both the low (green) and the high (red) traffic subsets were separately found to be linearly correlated to the  $\text{PM}_{10}$  concentration with slopes  $\alpha_{\text{green}} = (0.0015 \pm 0.0001) c$  and  $\alpha_{\text{red}} = (0.0023 \pm 0.0001) c$ , correlation coefficients of 0.86 and 0.72, respectively. In both fits, aerosol extinction was constrained to zero for the limit case, when  $\text{PM}_{10}$  concentration was zero.  $\text{PM}_{10}$  concentrations appeared to be best correlated with aerosol extinctions averaged over the entire scanning area, when aerosol concentrations were not dominated by traffic contributions from the vicinity of the ground-based measuring site.

## 4.2 Winter-time measurements in Nova Gorica

A similar campaign as in May 2010 was performed in winter conditions on 30–31 January 2012, in order to provide an insight into seasonal effects on the atmospheric processes above Nova Gorica. In winter season, cold N-NE winds generally prevail throughout the day, which was the case during this campaign as well, with occasional presence of wind reversal from the Adriatic Sea in the SW. Wind information 10 m above the ground was obtained from an environmental monitoring station and is shown in Fig. 4.9. In comparison to weather conditions during our May 2010 measurements (Fig. 4.4), wind speed was about three times higher reaching hourly maximum values of about 17 m/s. Considering that lidar measurements were performed at a altitude of 200 m above the ground, based on the logarithmic velocity law (Garratt, 1992), much stronger winds can be expected at that height. Under these conditions, convective turbulence can be expected and thus the atmosphere plane cannot be considered to be homogeneous. This effect is clearly seen in both RHI (Fig. 4.10) and PPI (Fig. 4.12) scans during the campaign. In this case, the retrieval method of aerosol extinction coefficient described in Sec. 4.1.2, is not suitable at all. In this section, we investigate the atmospheric structure and dynamics in the lower troposphere and the dispersal and the trajectories of aerosols based on the lidar RHI and PPI scans.

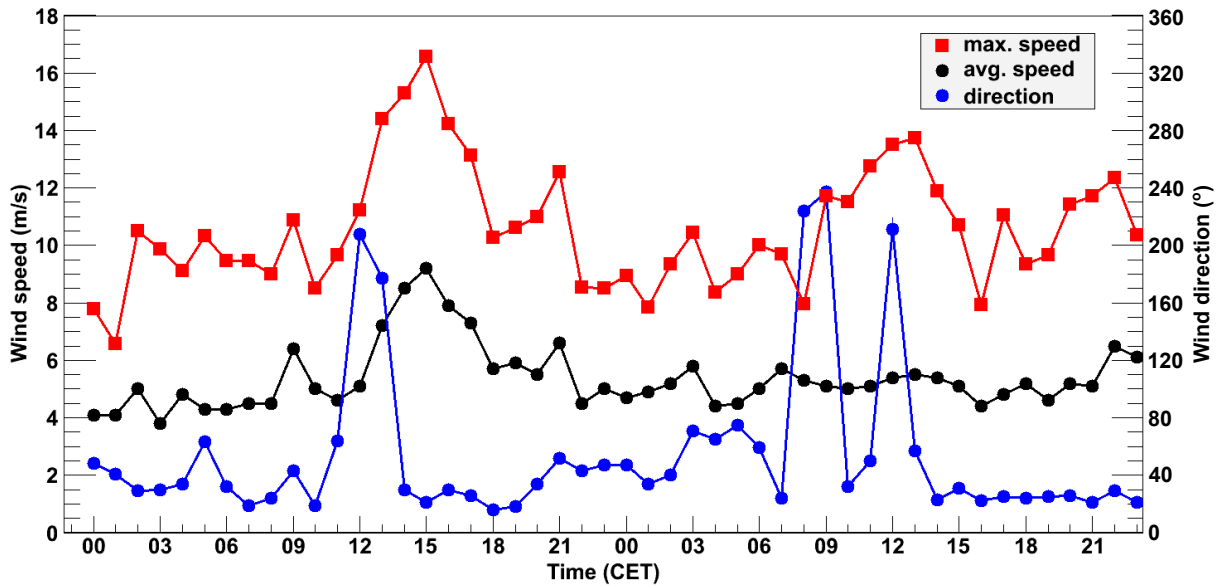


Figure 4.9: Hourly wind information from 30–31 January 2012, obtained 10 m above the ground. Wind direction was predominantly N-NE with occasional short term changes to SW.

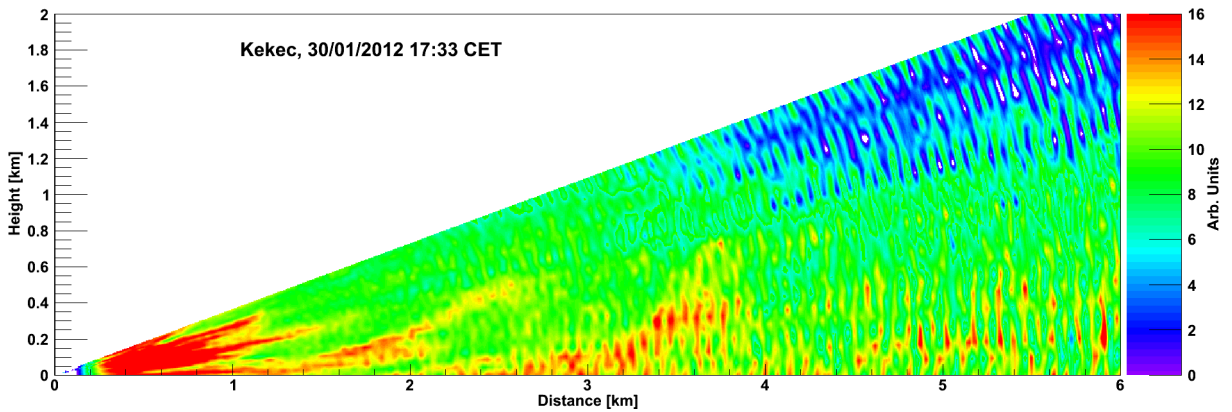


Figure 4.10: Example of vertical RHI scan showing the logarithm of the range-corrected lidar signal for elevation angles from  $0^\circ$  to  $20^\circ$  with angular step of  $1^\circ$ , performed at 17:33 CET on 30 January 2012. Aerosol plumes moving away from the lidar site due to the strong NE strong winds can be seen.

#### 4.2.1 Vertical atmospheric structure

Under unstable and windy conditions pollutants emitted at the surface can be rapidly lifted due to convection or vertical wind shear, and then mix with the upper background aerosols. This results in a well-mixed troposphere. However, the atmosphere is usually turbulent and heterogeneous near the surface. In our case study we used

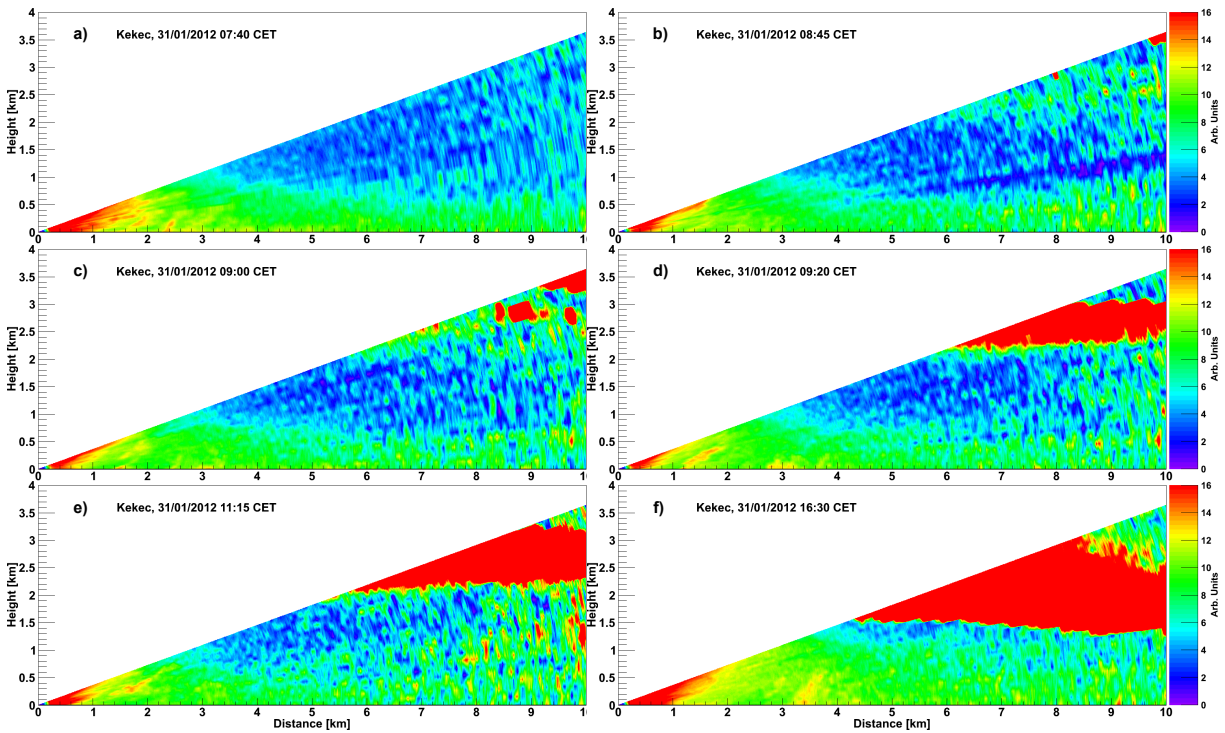


Figure 4.11: Time series of vertical RHI scans performed from 07:30 to 16:30 CET on 31 January 2012. The dispersal of aerosol plumes was observed throughout the day. The height of the aerosol layer near the surface was found to be non-uniform and to decrease with distance from the lidar site. In the morning, a low layer of clouds 2.5 km above the lidar site formed in about 30 minutes and remained present the whole day.

vertical RHI scans to reveal vertical distribution of aerosols in the lower troposphere. The RHI scan performed at 17:33 CET on 30 January 2012 (Fig. 4.10) illustrates an example of vertical mixing of aerosols in the lower troposphere. Aerosol plumes were lifted up to 600 m above the lidar site (about 800 m above the ground) and were carried away due to the presence of strong NE winds (Fig. 4.9). Most aerosols were detected between the surface and the height of 1.2 km above the lidar site.

Temporal development of the vertical structure of the lower troposphere from 07:30 to 16:30 CET on 31 January 2012 is illustrated by a time series of RHI scans (Fig. 4.11). In addition to a non-uniform aerosol layer near the surface, which was found to decrease with the distance from the lidar and to reach a maximum value of 1.5 km at 16:30 (Fig. 4.11 f), lower troposphere was initially clear and without clouds at 07:40 (Fig. 4.11 a). Due to wind reversal between 08:00 and 09:00 CET (Fig. 4.9), a layer of clouds appeared at about 3.5 km and a new layer of clouds gradually formed at about 2.5 km, the process taking about 30 minutes (Fig. 4.11 b–d). Once formed, the cloud



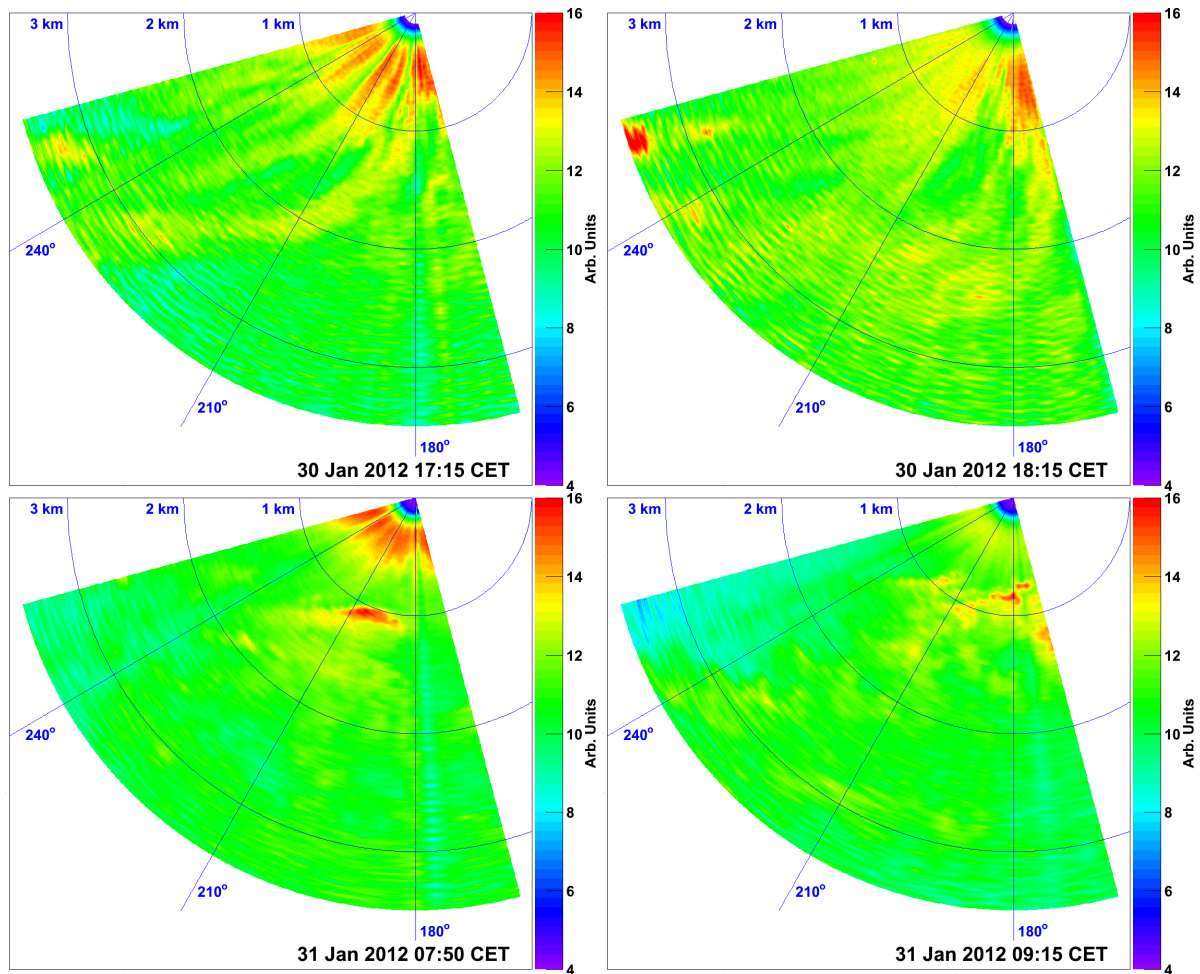


Figure 4.12: Examples of horizontal PPI sector scans showing the logarithm of the range-corrected lidar return signal, demonstrate localized increases of lidar return corresponding to aerosol dispersions. Complex dispersion paths of the plumes and a significant inhomogeneous atmosphere due to the relatively strong wind can be clearly seen. Measurements at around 18:00 CET on 30 January (top), shows the plumes blended towards southwest under stable NE wind conditions.

layer at 2.5 km remained present throughout the day.

#### 4.2.2 Localized aerosol sources

In addition to always present exhausts from industrial emissions and traffic emissions along the roadways, in the winter numerous localized aerosol sources are expected to appear as a result of domestic heating devices. Due to windy conditions during the campaign the emissions from these individual sources rapidly mixed with the upper

background aerosols and could not be exactly localized using the range and azimuth information from horizontal PPI scans. A time series of horizontal PPI sector scans presenting the logarithm of the range-corrected lidar return signal is shown in Fig. 4.12. Measurements on both 30 and 31 January 2012 show localized increases of lidar return (corresponding to aerosol dispersions) with complex dispersion paths of the plumes and a significant atmospheric inhomogeneity at the lidar scanning altitude. Under stable NE wind conditions on 30 January 2012, 17:15–18:15 CET (Fig. 4.9) the plumes were found to spread towards the south-west with dispersion distances of about 3 km (Fig. 4.12 top). With the presence of the reversal winds on 31 January 2012 between 07:00–10:00 CET, dispersion paths could not be clearly seen (Fig. 4.12 bottom). Sequential horizontal PPI sector scans from a fast scanning lidar, may provide a visualization of wind directions within the scanning region, using aerosols as tracers.

## 4.3 Observation of atmospheric processes in Ljubljana

Increase of aerosol concentrations that arises from human activities may have a significant impact on atmospheric processes in the ABL. Aiming at the study of the ABL dynamics and aerosol loading in urban areas, a measurement campaign was carried out in Slovenia's capital Ljubljana from 15:00 15 June to 10:00 CET 18 June 2012 using our mobile lidar.

### 4.3.1 Measurements

The mobile lidar was positioned at the premises of Slovenian Environment Agency in Ljubljana center (46.06° N, 14.51° E, 297 m a.s.l.). The device operated at 1064 nm, was set to a fixed elevation angle of 30° and was automatically collecting data in 1 s interval. In present study, lidar data were averaged to 15 min profiles. Aerosol extinction coefficient was then retrieved using the far-end Klett method (Klett, 1981) with a assumption of the fixed lidar ratio for  $50 \pm 5$  sr. The reference height was set to the height where just pure molecular attenuation occur (about 5 km).

Throughout the lidar operation, concentrations of  $PM_{10}$  and  $NO_x$  and meteorological data (temperature, humidity, air pressure and wind speed and direction) were also continuously monitored by a weather station at the lidar site. Additional information was provided by meteorological radiosondes, which were launched daily at 2 AM. Based on the collected data, we investigated the variation of the ABL and daily aerosol cycles in Ljubljana.





Figure 4.13: Photograph of the measurement location in Ljubljana (taken by Iztok Sinjur).

### 4.3.2 Results and discussion

The ABL, as the lowest part of the troposphere, its height is variable in space and time, and its behaviors directly influenced by human activities. It is of great importance to understand the temporal and spatial variation of the ABL. In the present study, ABL height was determined from a combination of lidar and radiosonde measurements as a height with a sharp increase in temperature and a sudden drop in the concentration of water vapor and aerosol loading. Radiosonde profiles and corresponding lidar derived aerosol extinction coefficient profiles obtained in this campaign are shown in Fig. 4.14.

On 16 June 2012, 02:00 CET, when both lidar and radiosonde data were available, the ABL height was estimated as the height of a distinct decrease (significant negative gradient) in the lidar-derived aerosol extinction coefficient profile (Fig. 4.14 a), which was observed at about 0.9 km a.s.l. (0.6 km above the ground). At the same height, temperature inversion and a decrease of relative humidity was observed in the corresponding radiosonde profile (Fig. 4.14 d). On all days of the campaign, stable boundary layer was found to be typically formed in the early morning. In addition to the single-point-in-time determination from the thermodynamic structure of atmosphere (the potential

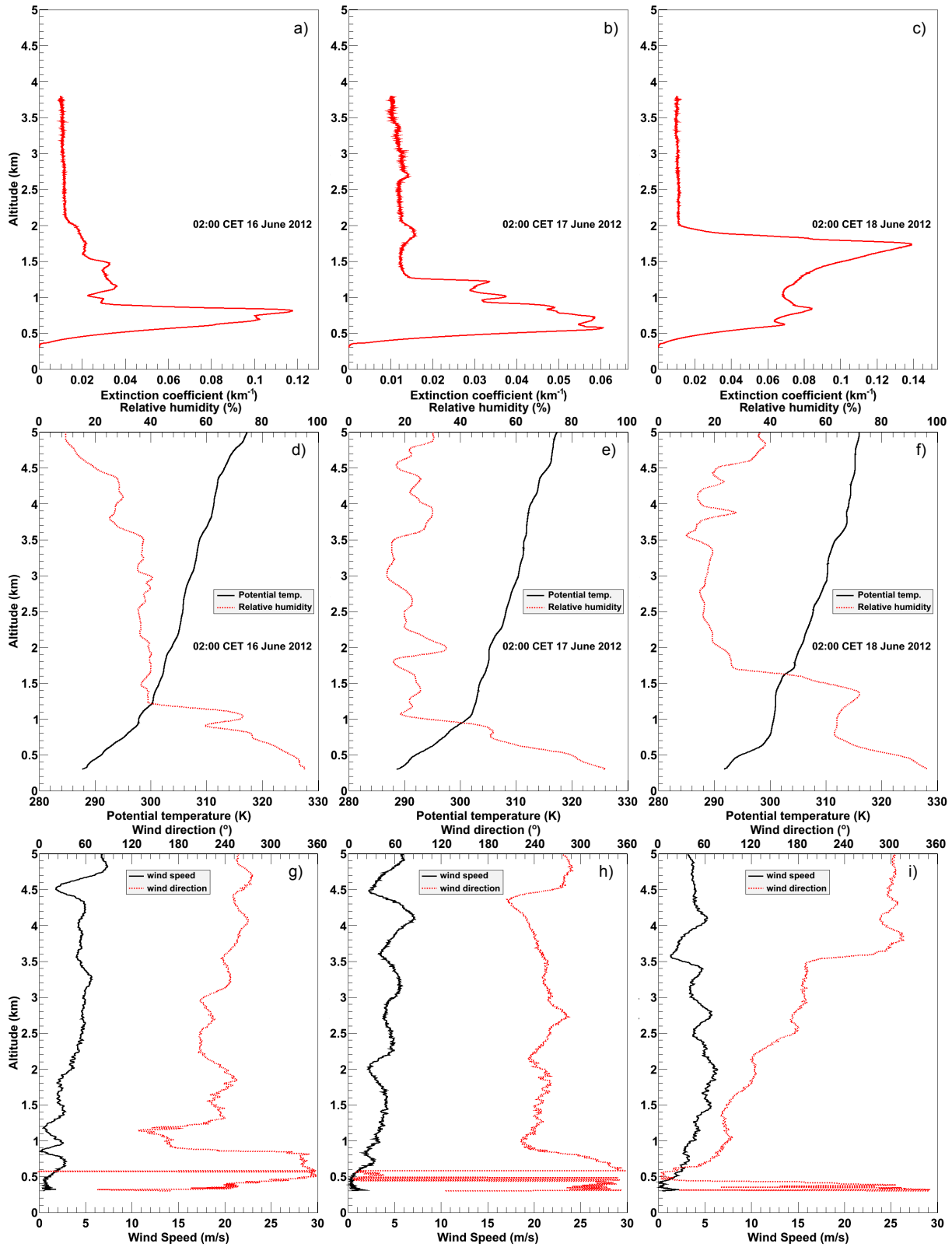


Figure 4.14: Vertical profiles of aerosol extinction coefficient from mobile lidar measurements for the time that radiosondes launched (top). Vertical profiles of potential temperature and relative humidity (middle), and wind profiles (bottom) from radiosonde observations.

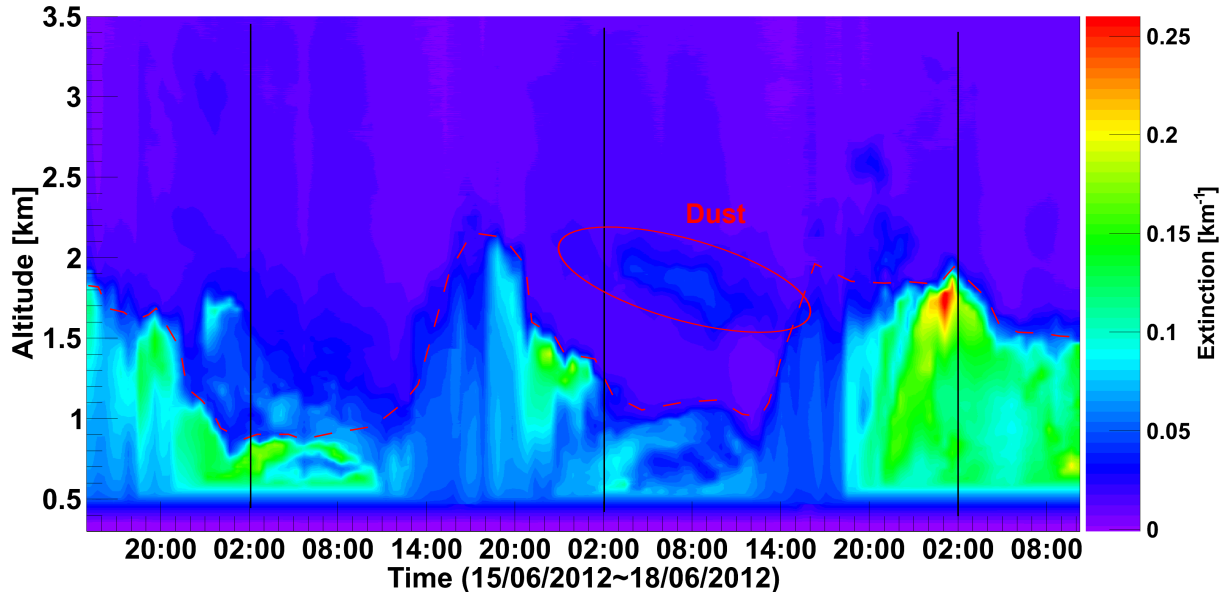


Figure 4.15: Temporal development of aerosol loading over Ljubljana from 15:00 15 June to 10:00 CET 18 June 2012, in terms of aerosol extinction coefficient ( $\text{km}^{-1}$ ) at 1064 nm. The variation of the ABL height is denoted by red dash line and daily cycles can be clearly seen during the measurements. The black solid lines denote where the radiosonde measurements are available.

temperature increases with height) obtained with the radiosonde, lidar measurements provided the dynamics of its formation, which lasted several hours (Fig. 4.15). Similar boundary layer structure was observed in the morning on 17 June 2012 with a ABL height of about 1.1 km a.s.l. A thin elevated aerosol layer was observed above the ABL (between altitudes of 1.8–2.1 km) with extinction coefficient of about  $0.035 \text{ km}^{-1}$  at 1064 nm. The increased relative humidity can be also seen at corresponding altitudes (Fig. 4.14 e). The elevated aerosol layer was found to contain mineral dust particles. Presence of Saharan dust was later confirmed by ground-based  $\text{PM}_{10}$  measurements and the DREAM model (Nickovic et al., 2001), which provides the prediction and validation of the presence of mineral dust aerosols above Europe. The altitude of the layer decreased with time and the aerosols then penetrated into the ABL in the afternoon (Fig. 4.15). This generated a large mixed layer (entrainment zone) of about 0.8 km between 0.7–1.5 km a.s.l., where the potential temperature and relative humidity were nearly constant with height (Fig. 4.14 f). Mixing of dust particles and emissions from the surface yielded relatively high values of extinction coefficient (around 01:00 CET on 18 June 2012 it exceeded  $0.2 \text{ km}^{-1}$  at 1064 nm) at the top of the ABL. ABL height was

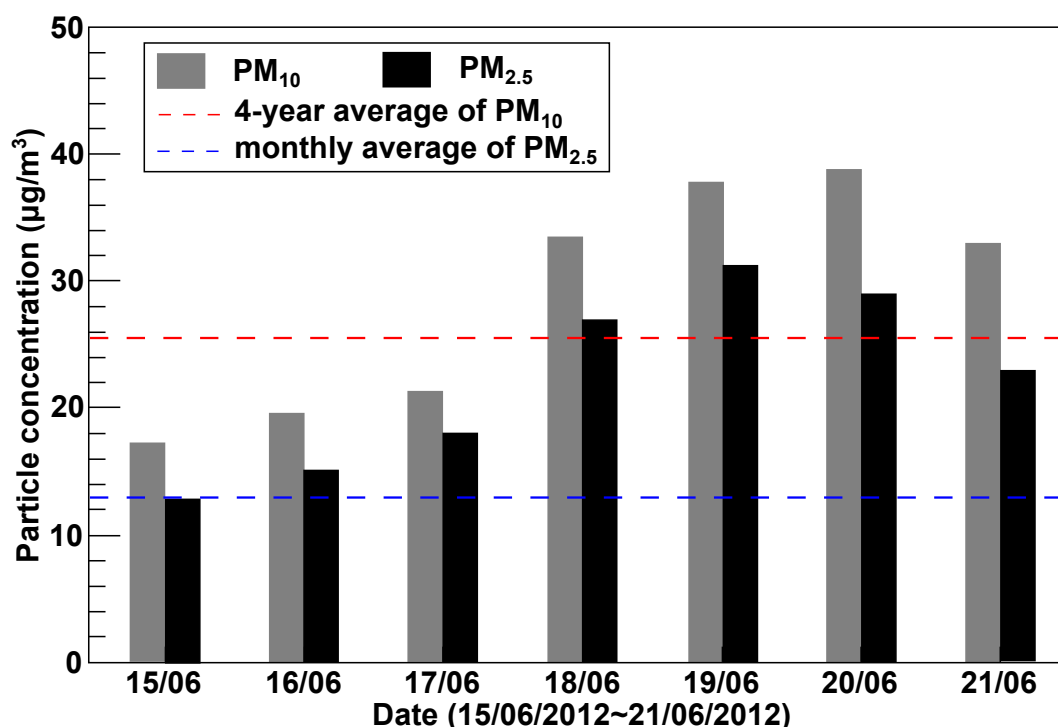


Figure 4.16: Daily average of PM<sub>10</sub> and PM<sub>2.5</sub> concentrations in Ljubljana from 15–21 June 2012, obtained from the ground-based measurements.

found to be 1.8 km a.s.l. at 02:00 CET on 18 June, which is a factor of approximately 2 higher than that on 16 and 17 June. Although the synoptic situation throughout the campaign were mainly influenced by anticyclonic conditions and the wind speeds in the lower troposphere were light, with mostly less than 5 m/s (Fig. 4.14 g–i), the wind directions on 18 June were found to be quite different with that on 16 and 17 June. After further investigation of meteorological circumstances, we found that on 19 June a weak cold flow was present over Ljubljana, which might have influenced the increase of the ABL height on 18 June. The presence of mineral dust at lower altitudes might also have an impact on the development of the ABL.

Daily average of PM<sub>10</sub> and PM<sub>2.5</sub> concentrations in Ljubljana from 15–21 June 2012 are shown in Fig. 4.16. Ground-based measurements show that although daily concentrations of particles slightly increased between 15–17 June, PM<sub>10</sub> concentrations are lower to the long term average. Distinct increase of both PM<sub>10</sub> and PM<sub>2.5</sub> concentrations presented between 18–21 June, with a pronounced PM<sub>2.5</sub> concentrations exceeded monthly average for a factor of two and a PM<sub>10</sub> concentrations exceeded the 4-year average. This provides further evidence of the presence of dust particles above

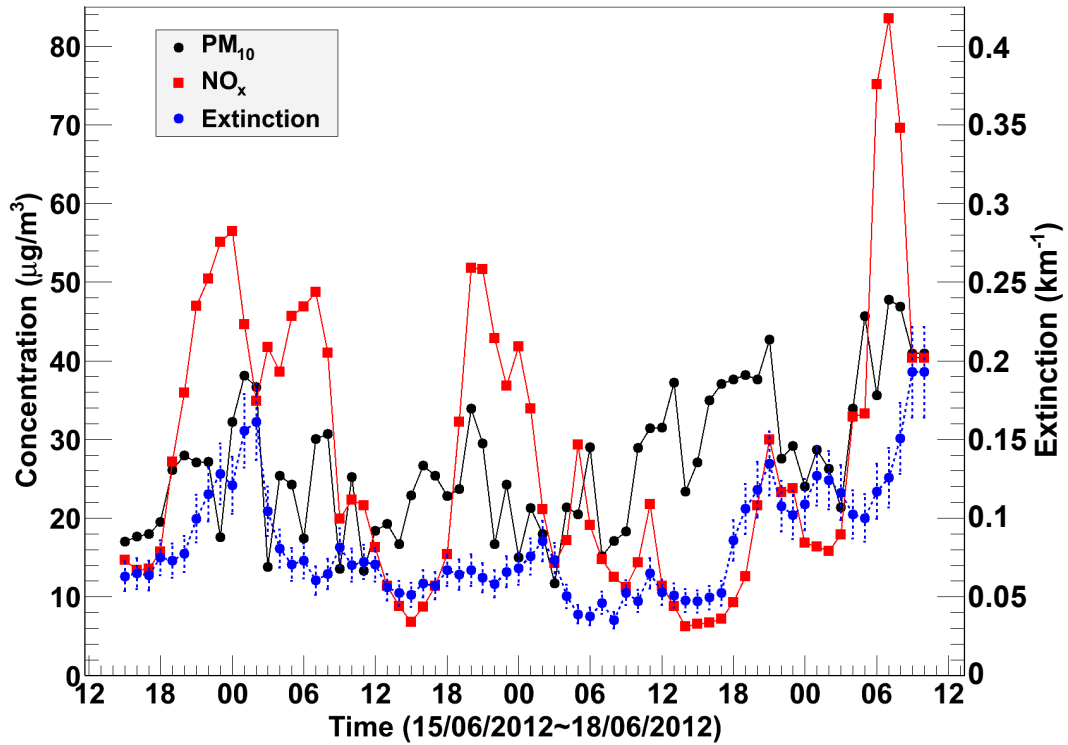


Figure 4.17: Temporal evolution of  $PM_{10}$  and  $NO_x$  concentrations for the period of 15–18 June 2012, obtained from the ground-based measurements. Extinction coefficients at the height of 400 m above the ground (about 700 m a.s.l.) derived from lidar measurements are also shown.

Ljubljana. These measurements also showed a considerable impact of the deposition of mineral dust on local environment. Daily average of particulate matter concentrations measured throughout this study, shows a high  $PM_{2.5}$  fraction in  $PM_{10}$ , up to ~78.5%. For the days (15–17 June) that aerosol concentrations were only dominated by local emissions,  $PM_{2.5}$  represented 80.3 % of  $PM_{10}$ , and the days (18–21 June) by both emissions and dust was 77.8 %. Contributions of both emissions and mineral dust particles to  $PM_{2.5}$  are expected to be high.

Temporal evolution of aerosol loading above Ljubljana throughout the 67 hours of the continuous measurement expressed as time height indicator (THI) plot is shown in Fig. 4.15. Throughout the measurement time, aerosols were present mainly within the ABL. THI plot also presents daily variations of the ABL height, which generally achieved its maximal values in the afternoon, as the accumulative solar radiation reached the maximum value in the day. After the sunset, the ABL height gradually decreased and the first distinct decrease appeared around 21:00. The minimum value of the ABL height was found to be in the early morning, in which the surface totally

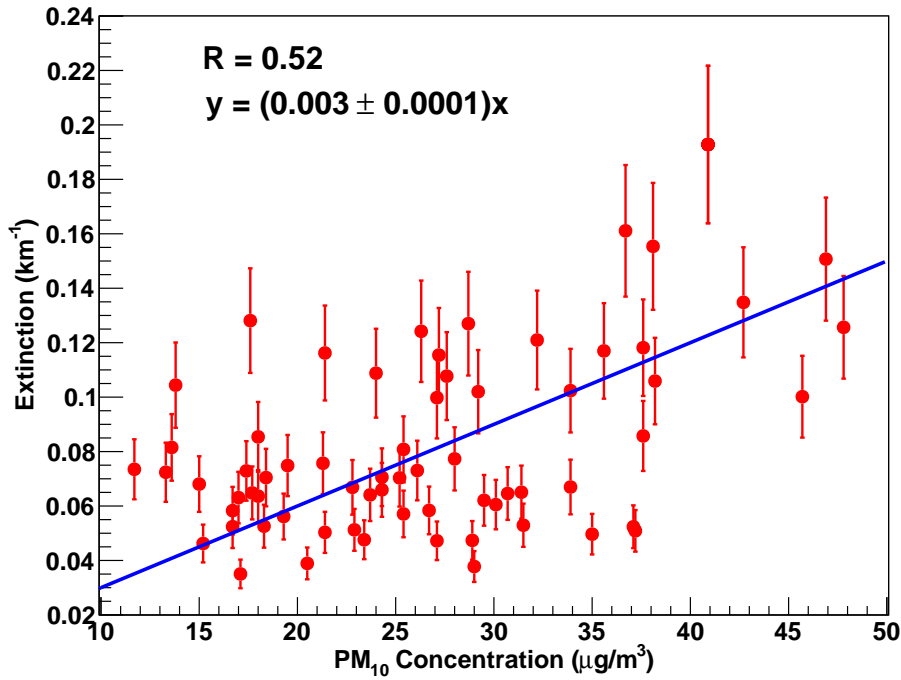


Figure 4.18: The correlation between the lidar-derived extinction at the height of 400 m above the ground and the PM<sub>10</sub> concentration measured on the ground level. The correlation coefficient was found to be 0.52 with a slope of  $0.003 \pm 0.0001 \text{ m}^3 \text{ km}^{-1} \mu\text{g}^{-1}$ . In the fits, aerosol extinction was constrained to zero for the limit case, when PM<sub>10</sub> concentration was zero.

cooled down and human activities were rarely. With the sunrise, increased solar radiation heated the surface again and intensified thermal convection caused the boundary layer to lift to higher altitudes.

Daily variations of PM<sub>10</sub> and NO<sub>x</sub> in Ljubljana are also clearly visible in the ground-based data, shown in Fig. 4.17. Figure 4.17 additionally presents the hourly aerosol extinction coefficients extracted from the lidar measurements at 400 m above the ground, where the complete overlap is expected. The high concentrations of both PM<sub>10</sub> and NO<sub>x</sub> were found at around 07:00 in the morning and 21:00 in the evening, which can be related to human activities and ABL dynamics. The decrease of concentrations was found at around 15:00 in the afternoon. In this period, emissions at the surface were mixed throughout the thicker ABL due to the strongest convection in the day. This results in the decrease of particle concentrations on the ground level. This effect was also confirmed by the presence of relatively low values of aerosol extinction coefficient at 400 m above the ground.

Figure 4.18 shows the correlation between aerosol extinction coefficient at 400 m

above the ground and  $\text{PM}_{10}$  concentration on the ground level was investigated using hourly averaged data. The correlation was found to be linear with a slope of  $0.003 \pm 0.0001$  and a correlation coefficient of 0.52. In the fit, aerosol extinction was constrained to zero for the limit case, when  $\text{PM}_{10}$  concentration was zero. One of the main reasons for imperfect correlation is expected to be related to different altitudes of processes related to the ABL behavior. During morning rush hours, emissions from the surface due to the human activities were found not to mix with higher atmosphere due to a very stable boundary layer (turbulences are rare) that remained from previous night (Fig. 4.15). The obstacle of vertical mixing resulted in a non-uniform distribution of aerosols with height. In our case, another source of uncertainty is assumed to be the presence of mineral dust at lower altitudes. Relatively high aerosol extinction coefficients were observed as mineral dust penetrated into the ABL, however, in the stable conditions the hourly concentrations of  $\text{PM}_{10}$  at the ground level may remain unaffected at the time. This effect was observed later as an increase of daily average of  $\text{PM}_{10}$  concentrations (Fig. 4.16).

## 4.4 Investigation of aerosol distributions in Iowa City

In addition to industrial plants, a large source of anthropogenic pollution in urban areas is traffic. The concerns regarding the impact of aerosol emissions from diesel soot and gross emitting vehicles continue to be raised, e.g. the impact of roadways on adjacent environments, which has proven to be a problem in urban regions. A case study of aerosol loading within Iowa City, USA and along the highway Interstate 80 between Iowa City and Davenport was conducted on 9 and 10 August 2011 using a vehicle-mounted elastic lidar (Sec. 3.3). The measurement campaign is described in this section.

### 4.4.1 Experimental setup

The measurements were performed using The University of Iowa mobile lidar system (1064 nm) mounted inside a dedicated vehicle. The system was capable of taking vertical aerosol measurements while in motion and recording the current position using built-in GPS receiver. The return signals from 50 laser pulses were averaged to 1 s profiles, with a spatial resolution of 1.5 m.

On 9 August 2011, in the presence of mild breezes and cloudless sky, an East-to-West transect measurement across the Iowa City from the city center to the suburbs



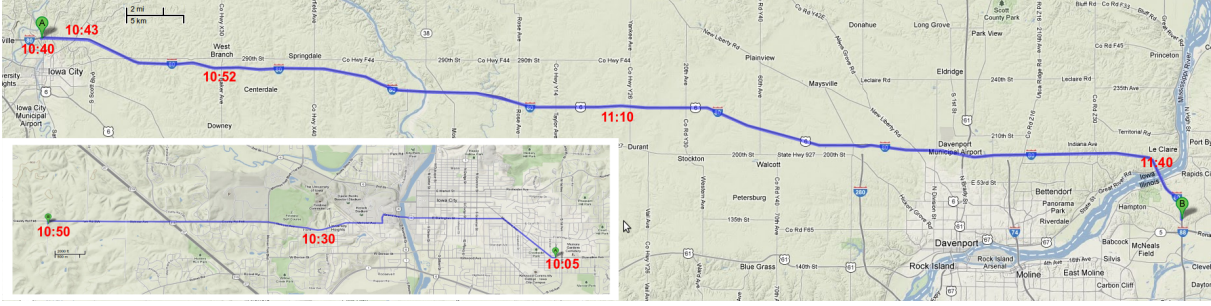


Figure 4.19: Exact routes of the two transect measurements performed on 9 and 10 August 2011. The larger upper map shows the highway Interstate 80 measurement on 10 August 2011 and the inlaid map measurement in the urban center and the suburbs performed on 9 August 2011.

was performed to obtain the vertical aerosol distributions and observe the transition between the urban area and the suburbs. The transect (Fig. 4.19) started at 10:05 Central Standard Time (CST) from Muscatine Avenue and continued through the urban core and reached County Road F46 in the western suburbs of the city at 10:50 CST. On 10 August, a West-to-East transect (Fig. 4.19) along the highway Interstate 80 between Iowa City and Davenport was performed as well, with the aim of investigating the aerosol distributions in the rural areas and the impact of roadways on the adjacent environment.

To be able to normalize elastic lidar return signals (Eq. 4.1) to aerosol concentrations they need to be transformed into atmospheric extinction profiles. As the lidar operated in the infrared part of the spectrum, the contribution from molecular scattering to extinction and backscatter coefficients was considered to be negligible. Under the assumption of fixed extinction-to-backscatter ratio with a value of 50 sr, the atmospheric aerosol extinction coefficient profiles can be retrieved by the Klett method (Klett, 1981) as

$$\alpha(r) = \frac{P(r)r^2}{P(r_m)r_m^2\alpha_m^{-1} + 2 \int_r^{r_m} P(r')r'^2 dr'} , \quad (4.3)$$

where  $\alpha_m = \alpha(r_m)$  is aerosol extinction coefficient at a height of  $r_m$ . While there are several other more complex algorithms for calculating atmospheric extinction, Klett method was found to be fully adequate approach for the purpose of this study (Lewandowski et al., 2010).



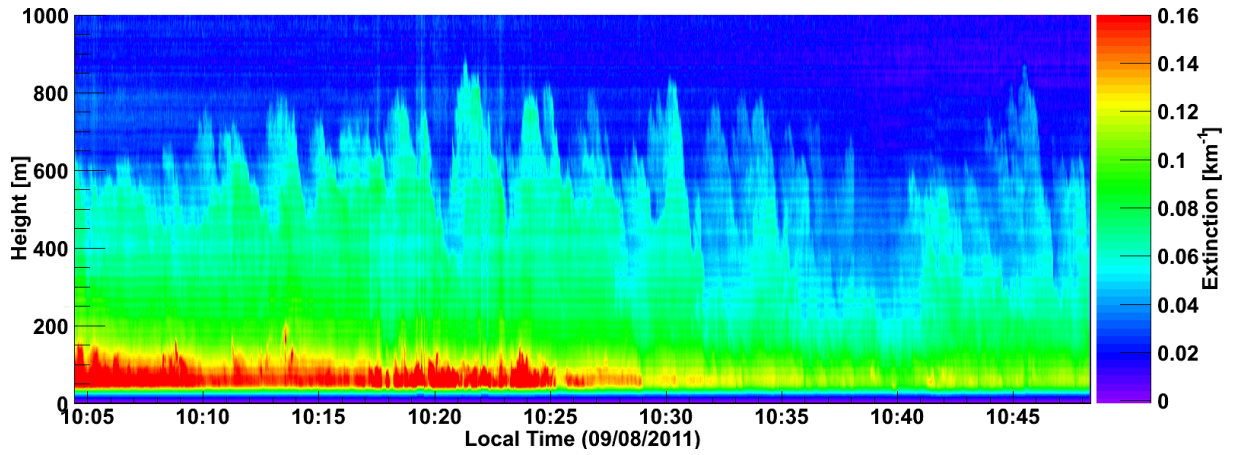


Figure 4.20: Time series of vertical profiles of aerosol loading over Iowa City and its suburbs on 9 August 2011 obtained by vehicle mounted elastic lidar. The exact route of the vehicle is shown in the inlay of Fig. 4.19.

#### 4.4.2 Aerosol presence in the vicinity of Iowa City

Lower troposphere is usually well mixed due to the convection or vertical wind shear. On the other hand, horizontally stratified layers can be formed under stable atmospheric conditions. Meteorological conditions for 9 August 2011, the first day of our study, were persistent, mild breeze, clear sky and stable surface conditions. The transect through the Iowa City was performed from 10:05 to 10:50 CST, from the urban area in the east to the western suburbs. The main purpose was to investigate the vertical distribution of aerosols within atmospheric boundary layer (ABL) and its transition from the status within and outside of the city. In lidar-derived aerosol extinction Fig. 4.20, the trend of the ABL height and the evolution of aerosol layers can be clearly seen. Aerosols were present mainly within the ABL, which was found to be less than 800 m above the ground. The ABL was found to be more stable inside the urban area.

At the beginning of the transect measurements, when the lidar was within the city, the height of the local pollution plume was observed to be less than 200 m above the ground with aerosol extinction coefficient of about  $0.16 \text{ km}^{-1}$ . In urban areas, one of the dominant sources of aerosols was expected to be traffic. As the vehicle-mounted lidar measurements were performed directly above the roads, this may provide an explanation for very high particulate concentrations obtained. From around 10:30 on, the amount of the dense plume close to the ground decreased as the lidar left the busy road with congested traffic and entered into the suburban area. Throughout the transect measurement, the aerosols originating from local ground-based pollution sources

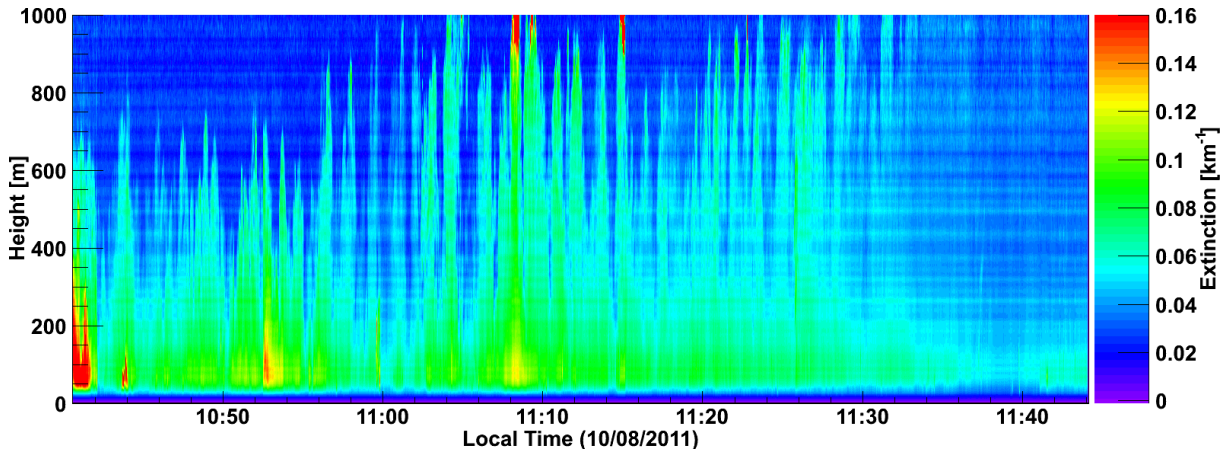


Figure 4.21: Temporal development of aerosol loading along the highway Interstate 80 for the transect between Iowa City and Davenport on 10 August 2011 obtained by vehicle mounted elastic lidar. The exact route of the vehicle is shown in Fig. 4.19.

kept close to the ground and did not mix considerably with the upper residual layer.

Using the lidar data from the highway transect measurement, the observation of the vertical evolution of aerosols in the lower troposphere and the study of the impact of roadways on the aerosol distribution in the ABL were performed. Figure 4.21 presents lidar-derived vertical extinction profiles along the highway Interstate 80 on 10 August 2011. At the beginning of the transect measurements around 10:40, when the lidar was at the highway entry closest to the Iowa City, local plume with high aerosol concentrations extended up to the height of 400 m above the ground. This effect was mainly due to road repairs, where a considerable amount of dust was picked up and injected into the ABL and partially also resulting from dense traffic on the interstate close to the Iowa City. The measurements revealed a sharp decrease in particulate concentrations as the lidar proceeded along the highway away from the construction site. At around 10:43 CST, at the distance of about 3 km from the starting point, aerosol concentration increased again and was found to coincide to the next highway entry with its adjacent commercial region. Increased aerosol concentrations appear also at around 10:53 and 11:08, when passing through the towns of West Branch and Durant. At about 11:30 the vehicle entered the region influenced by the Mississippi River, which resulted in considerable drop of aerosol concentrations in the ABL with aerosol extinction coefficient of about  $0.052 \text{ km}^{-1}$ , notably less than in the neighboring dry areas ( $0.071 \text{ km}^{-1}$ ).

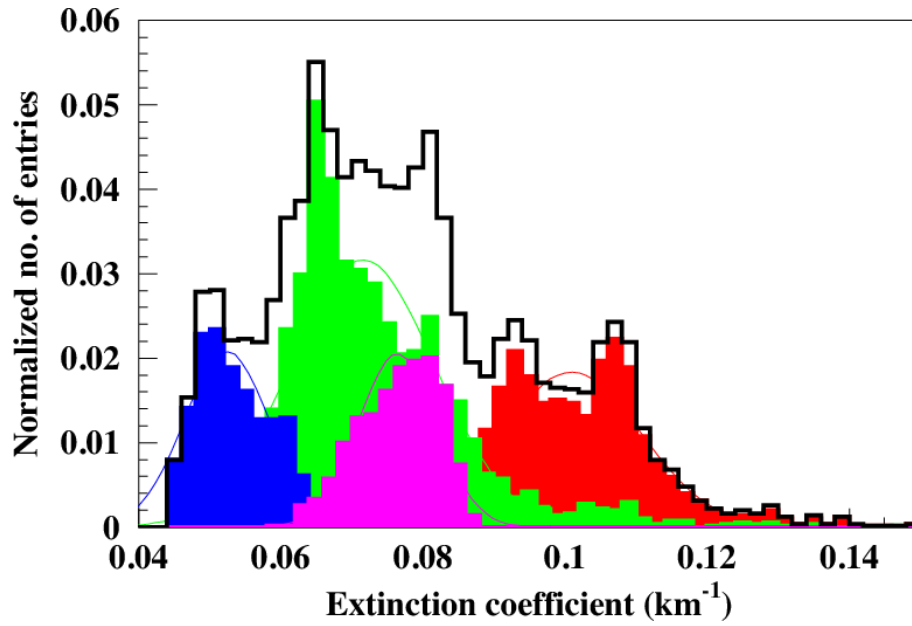


Figure 4.22: Distribution of aerosol extinction coefficient at 150 m above the ground was found to depend strongly on the terrain type. Cumulative distribution of the two measurements on 9 and 10 August 2011 is presented by filled histograms with the distributions corresponding to particular terrain types (based on GPS and timing data). Extinction mean value for urban terrain (red) was found to be  $0.1 \text{ km}^{-1}$ , suburban (purple)  $0.076 \text{ km}^{-1}$ , rural (green)  $0.071 \text{ km}^{-1}$  and riverside (blue)  $0.052 \text{ km}^{-1}$ . Means were obtained from Gaussian fits.

#### 4.4.3 Area dependence of aerosol extinction

As the aerosol extinction measurements were performed in stable weather conditions in different terrain configurations (urban, suburban, rural and riverside) within 48 hours, we investigated the correlation of the extinction to the terrain type (based on GPS and timing data) at a fixed height of 150 m above the ground. The results for both days are shown in Fig. 4.22, where the cumulative distribution of the full dataset from the two transects is presented by filled histograms with the distributions corresponding to particular terrain types. Both for 9 August (urban and suburban) and 10 August (rural and riverside) measurements of aerosol extinction show strongly general dependence on the terrain type. Distributions of the extinction coefficients in the suburban and riverside regions show relatively narrow modes with central values of  $0.076 \text{ km}^{-1}$  (suburbs) and  $0.052 \text{ km}^{-1}$  (riverside). The distribution of aerosol extinction in the urban areas of Iowa City was found to be broad, multi-modal with a central value of  $0.1 \text{ km}^{-1}$ . Two distinct modes at  $0.093 \text{ km}^{-1}$  and  $0.107 \text{ km}^{-1}$ , that imply the presence of multiple local aerosol sources that were detected in passing and contributed to the

total distribution. The distribution of the extinction along the Interstate 80 highway was also found to be broad and multi-modal with a mean of  $0.071 \text{ km}^{-1}$ . Different modes were in this case identified to be due to a variety of aerosol sources co-located to highway entries.

## 4.5 Conclusions

Atmospheric processes involving urban aerosols intuitively strongly depend on the city and location where these effects are being investigated. Namely, aerosol sources may differ, as well as atmospheric and topographic conditions. Aerosol monitoring over the neighboring towns of Nova Gorica in Slovenia and Gorizia in Italy (total population around 60.000, density  $800/\text{km}^2$ ) on 24–25 May 2010 and 30–31 January 2012 established that urban aerosol exhaust sources can be reliably detected by horizontal PPI lidar scanning. Detected sources were successfully identified by an inspection in the field. We also observed daily cycles of aerosol loading and established that traffic plays an important role in air pollution in the Nova Gorica/Gorizia region, as the aerosol loading regularly increases up to four times daily average values during the morning rush hours. In an attempt to correlate horizontal aerosol extinctions from lidar scanning at 200 m above the ground to  $\text{PM}_{10}$  concentration from ground-based measurements, we discovered that they are highly correlated (correlation coefficient 0.84) in a localized area directly above the ground-based measurement site. When averaging the extinctions over the entire scanning area, they remain highly correlated to the  $\text{PM}_{10}$  concentrations, when considered separately for high and low traffic conditions, but not so when averaging over all the data. The effect was found to be due to the proximity of the environmental monitoring station to a frequented road, which was strongly affected by local traffic. Maximum aerosol extinction of  $0.1 \text{ km}^{-1}$  at 1064 nm obtained in the campaign corresponds to about  $40 \mu\text{g m}^{-3}$ . Regarding the structure of the lower troposphere, complex flow dynamics between layers with increased aerosol content was observed. Notably, there were some noticeable differences between temporal evolution of aerosol extinction and  $\text{PM}_{10}$  concentration measured by an environmental station on the ground. These differences are expected to be related to the topographical properties of the region, the properties of aerosol constituents and the daily meteorological conditions. Under windy winter conditions we observed convective turbulences lifting aerosol plumes up to about 800 m above the ground due to the vertical wind shear. The height of the aerosol layer near the surface was found

to be non-uniform, with a maximum value of about 1.5 km. We also observed complex horizontal dispersion paths of the plumes at lidar scanning altitude. We conclude that using aerosols as tracers, scanning Mie lidar may be used for real-time wind field monitoring.

Lidar measurements in Ljubljana from 15–18 June 2012 provided temporal development of aerosol loading, which was used to investigate the dynamics of atmospheric boundary layer in a densely populated urban environment (population around 300.000, density 1700/km<sup>2</sup>). We observed that stable boundary layer typically formed only after 2 AM in the early morning. As in Nova Gorica/Gorizia, we observed daily cycles of aerosol loading in both lidar and ground-based monitoring data, with concentration peaks due to local traffic at around 07:00 and 21:00 CET. The correlation between the aerosol extinctions at 400 m above the ground obtained from lidar and mass concentration on the ground, obtained from the measurements of PM<sub>10</sub> concentration was found to be linear, with a slope of 0.003 m<sup>3</sup> km<sup>-1</sup> µg<sup>-1</sup> and a correlation coefficient of 0.52. During the campaign, the observed ABL at 02:00 CET on 18 June 2012 was found to be about a factor of 2 higher than that on 16 and 17 June, due to the change of synoptic conditions. Based on the ground-based measurements, the fraction of PM<sub>2.5</sub> in PM<sub>10</sub> was found to be up to ~78.5 %. Contribution of dust particles to PM<sub>2.5</sub> is expected to be high.

Lidar measurements of aerosol loading within and around Iowa City (population around 70.000, density 1000/km<sup>2</sup>) on 9 and 10 August 2011, show that aerosol plume from local pollution sources remained mainly less 200 m above the ground with extinction coefficient of about 0.16 km<sup>-1</sup> at 1064 nm. High aerosol concentrations which can be associated with the heavy traffic were observed inside the Iowa City. We observed that both maximum height and extinction coefficient of the aerosol layer gradually decreased when moving out from urban to suburban areas. The comparative study of the ABL structure and aerosol evolution between urban and rural areas shows that vertical mixing of air-masses is much more evident outside the city. In rural areas, increased aerosol concentrations were found to often coincide to the locations of highway entry ramps. Aerosol concentration in the vicinity of the Mississippi River was found to be notably lower than what was observed in the neighboring dry rural areas.



## Investigation of long-range transport of aerosols

Concentrations of aerosols and trace gases over the Mediterranean region are typically factors of 2 to 10 higher than over the North Pacific Ocean, which is expected to be the least polluted environment at low northern latitudes ([Lelieveld et al., 2002](#)). Only in China and northern India aerosol impact on climate is expected to be higher than in the Mediterranean (e.g., [Eek et al., 2005](#)). The southwestern region of Slovenia, located in the north Mediterranean between Julian Alps and Adriatic Sea, represents the first topographic barrier for warm and humid air masses approaching from Mediterranean. Due to this geographical position, strong winds (e.g., [Alpers et al., 2007](#)) frequently occur over the region. An extensive dry and wet deposition of aerosols is commonly present and can alter rapidly. The presence of aerosols mainly include marine (from North Atlantic Ocean and Mediterranean Sea) and mineral (due to the proximity to Sahara desert) components and anthropogenic components (e.g., [Barnada and Gobbi, 2004](#)). The effects of aerosols related to atmospheric processes on environment in Slovenia have not yet been fully investigated.

Through the whole autumn of 2010, daily aerosol lidar measurements were made at Otlica observatory (45.93° N, 13.91° E, 945 m a.s.l.) to provide data for statistical analysis of aerosol distributions and sources over the southwestern part of Slovenia. Mean profiles of aerosol extinction coefficient were obtained separately for the atmospheric boundary layer (ABL) and free troposphere (FT) as particles in the boundary layer usually originate from local sources, while free troposphere particles are often advected over long distances, even as far as from other continents. Lidar results were complemented by radiosonde observations, ground-based measurements of solid particle concentration and measurements of local meteorological conditions. Since the temporal and spatial distributions of aerosols in both the ABL and the FT are related

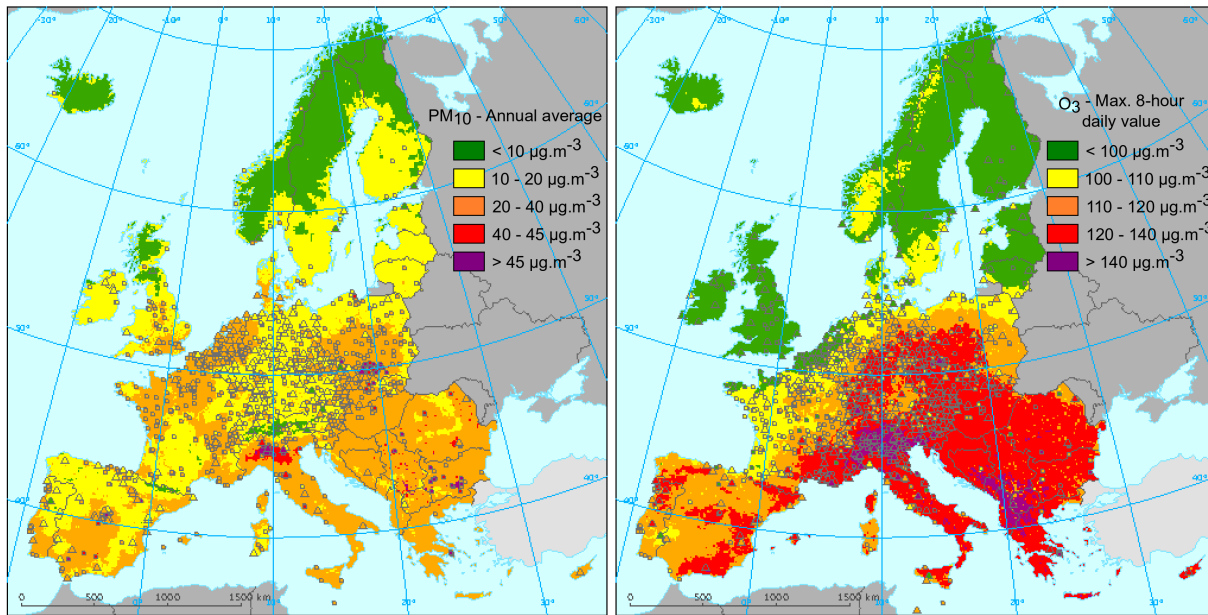


Figure 5.1: Distributions of annual average of  $PM_{10}$  concentration (left) and maximum 8-hour daily  $O_3$  value (right) over Europe in 2007. Images are from European Environment Agency (available at: <http://www.eea.europa.eu>).

to air flows, back trajectories were analyzed using clustering to investigate the dependence of the aerosol optical depth on the origin of the air masses. The present study in this chapter is the first attempt in Slovenia to derive long-term lidar measurements of tropospheric aerosol distributions on a regional scale.

## 5.1 Measurements and data analysis

### 5.1.1 Lidar-based remote sensing

Monitoring of aerosol vertical distribution both in the ABL and the FT was performed using the stationary Mie lidar at Otlica observatory. In a non-coaxial configuration, the incomplete overlap between the laser beam and the receiver field of view significantly affects lidar return signal in the near field. In order to increase the dynamic resolution of the digitizer in the far range, maximum input signal of the Licel transient recorder was decreased from 500 mV to 100 mV in the present study. This caused the saturation of return signals in the range of the first few hundred meters, which were in any case not used in our analysis due to incomplete overlap.

Regarding these issues, two kinds of measurement were executed: range height



indicator (RHI) scanning measurements for lower troposphere and vertical measurements for free troposphere, which facilitated the extraction of the extinction coefficient profile down to the lidar site (945 m a.s.l.) despite the difficulties caused by incomplete overlap. In the RHI scans, the elevation angle was increased in  $0.5^\circ$  steps from  $0^\circ$  to  $20^\circ$ . At each step, 200 laser shots were averaged and each scan took approximately 7 min to complete. In vertical measurements the retrieval profile was obtained in 5 min intervals. Measurements were performed on clear days from sunset to midnight throughout August–October 2010, as the daylight background was prohibitive. On days with precipitation and low altitude clouds, measurements were not performed. In all cases the obtained raw lidar data was normalized to the laser energy. Flat baseline of each return, which is proportional to the intensity of background noise, was subtracted, where the background noise was defined as the average value of data points sampled at the far end of the trace. Each lidar return was then corrected for inverse-range-squared dependence (Measures, 1988).

Spatial distribution of the range-corrected lidar return signal obtained by RHI scanning was presented by Cartesian 2D scans. To fill the pixels where no lidar data was available, a weighted value was reconstructed using a barycentric interpolation scheme (Min, 2004) between successive step profiles with a 10 m resolution of the Cartesian 2D grid. Under the assumption of horizontal atmospheric homogeneity, the atmospheric extinction coefficient profiles can be obtained from the horizontal rows of pixels in the 2D RHI plots, using the multiangle method (Filipčić et al., 2003; Gao et al., 2011a) without the need to select specific extinction-to-backscatter ratio (so-called lidar ratio). For geometrical reasons, retrieval errors with this method increase with height.

In vertical lidar measurements, the aerosol extinction coefficient was retrieved by the Fernald method (Fernald, 1984). The dependent extinction-to-backscatter ratio with 10 % relative error was set on the potential sources of aerosols (Ansmann et al., 1992). The molecular extinction coefficients at 355 nm were calculated from Rayleigh scattering theory (Bucholz, 1995) and radiosonde data of temperature and pressure. The calibration height was set to the height where pure molecular attenuation occurs (e.g. an aerosol-free region). An example of the comparison of aerosol extinction coefficients obtained by the multiangle method and the Fernald method are shown in Fig. 5.2. Good agreement was found over the measured altitude range and the mean deviation was estimated less than 15 %. In the example, a two-layer aerosol structure is clearly visible within the lower troposphere, with the boundary layer reaching about 1.8 km above sea level and the elevated layer at about 2.5 km. The thermodynamical structure of the atmosphere reveals also a presence of a weakly convective lower tropo-

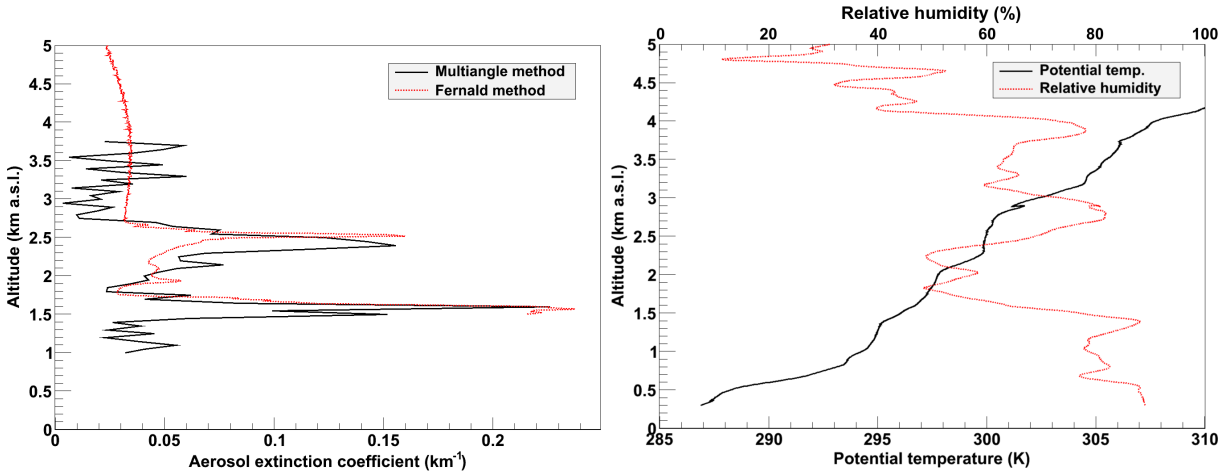


Figure 5.2: Intercomparison of lidar-derived aerosol extinction coefficients at 355 nm using multiangle method and Fernald method (left) and vertical profiles of potential temperature and relative humidity (right) on 17 August 2010. Only the data within complete overlap is presented.

sphere and a neutral atmospheric layer (potential temperature is almost constant with height) around 2.5 km.

The observable used to quantify aerosol presence, correlate aerosols to regions of origin and assess their impact on local environment is the averaged aerosol optical depth (AOD) at 355 nm of each day when the lidar measurements were available. AOD is obtained as a integral of aerosol extinction along the vertical extinction profile (Eq. 2.4 in Sec. 2.2). In order to estimate the contribution of free tropospheric aerosols to the total tropospheric optical depth, AOD in the ABL and the FT were calculated separately.

### 5.1.2 Radiosonde observations

During the lidar monitoring campaign, meteorological radiosondes<sup>1</sup> were launched daily at 2 AM by Slovenian Environment Agency in Ljubljana, 40 km away from Otlica. The instruments, which measured atmospheric pressure, temperature, relative humidity and wind (speed and direction) were calibrated by ground-based devices before each launch. Radiosonde data was used to determine the ABL height in an independent way and to complement lidar measurements.

<sup>1</sup>M2K2-DC GPSonde, Modem, France

### 5.1.3 Ground-based measurements

In order to examine the influence of air mass transport patterns on local environment, we used the data from a number of environmental and meteorological measurements routinely performed by Slovenian Environment Agency. Environmental station at Otlica observatory provided ozone ( $O_3$ ) concentrations, temperature, relative humidity, precipitation and solar irradiation, while the particulate matter ( $PM_{10}$ ) concentrations were measured at the town of Nova Gorica, about 20 km away, which may have been influenced by urban aerosol sources.

## 5.2 Aerosol transport modeling

Air masses form and pass over different geographic regions collecting anthropogenic and natural particles emitted from the surface. Their transport range relies on local weather conditions and typical atmospheric circulation patterns. Some particles are deposited close to their sources, while some may even be spread by air flow all around the globe. A way to distinguish directions of air flow is to analyze air trajectories, which are defined as the paths of infinitesimally small parcels of air ([Dutton, 1986](#)).

### 5.2.1 Air trajectories

Trajectories describe the paths of air parcels during a given time period with two perspectives: Eulerian and Lagrangian ([Jacobson, 1998](#)). Eulerian perspective considers air flows through spatial points, while Lagrangian focuses on space and time information for individual air parcels. Forward trajectories describe where particles will go, while backward trajectories where that are coming from. Backward trajectories provide visualization of not only the local air direction, but transport over a continental scale. The analytical backward trajectories of air masses provide information about origin of the observed aerosols, which is very important with regards to understand their effects on atmospheric optical properties. Systematic aerosol studies based on combined backward trajectories and long-term lidar observations can explain a possible dependence of the aerosol optical properties on the origin of the air mass ([Mattis et al., 2000](#)).

In the present study, 48-hour backward trajectories were daily computed for air flows arriving at Otlica from August to October 2010, using the Hybrid Single-Particle Lagrangian Integrated Trajectory (HYSPLIT) model ([Draxler and Hess, 1998](#)). The ar-

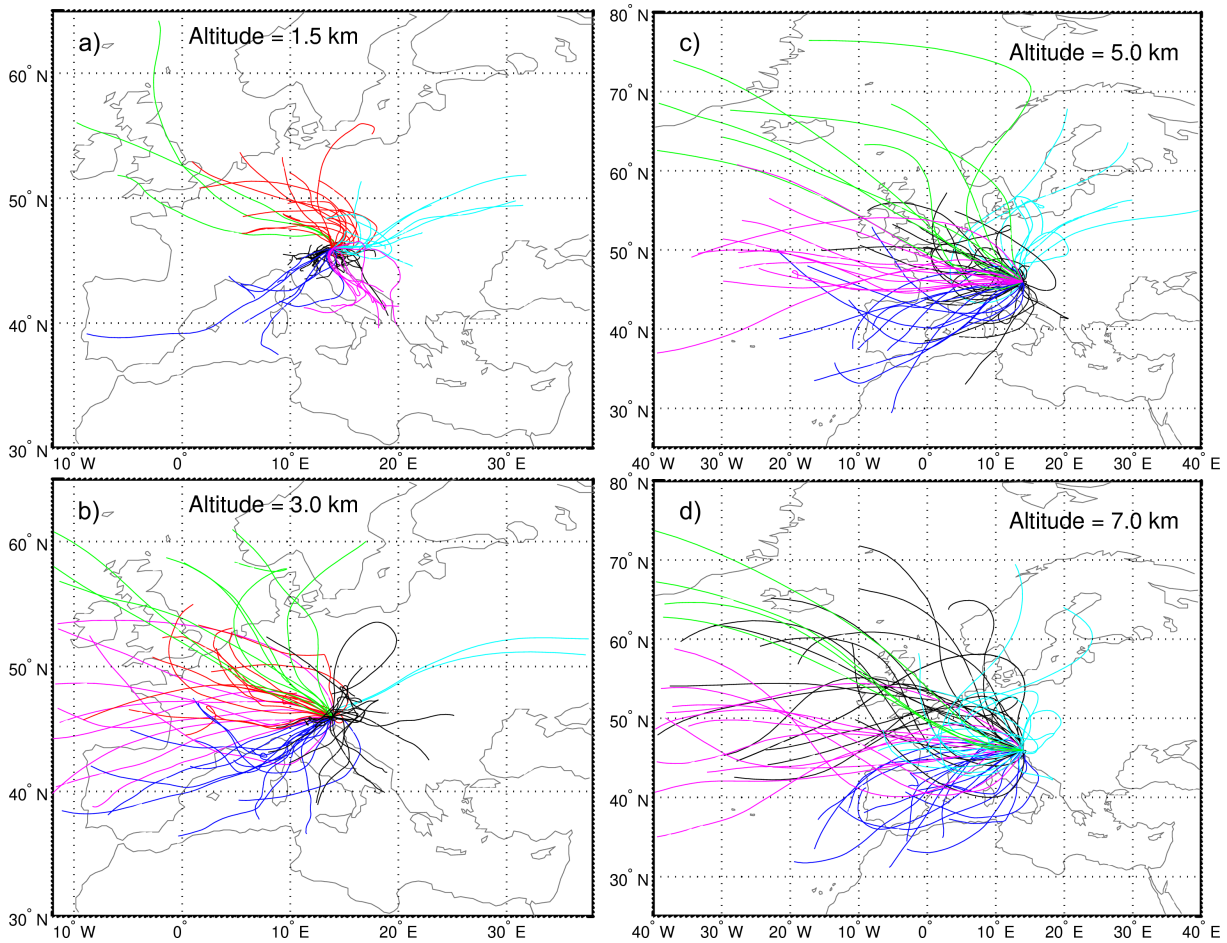


Figure 5.3: 48-hour backward trajectories of air masses over Otlica for the lidar monitoring period at different altitudes: 1.5 km (top left), 3.0 km (bottom left), 5.0 km (top right) and 7.0 km (bottom right), respectively.

rival time of the trajectories was set to 2100 UTC within the time of the lidar observations. Spatial resolution of the modeled flows was  $1^\circ$  in both latitude and longitude with a temporal resolution of 1 hour. Air flows were modeled at five different altitudes: 1.5 km, 3.0 km, 5.0 km, 7.0 km, and 9.0 km above sea level.

### 5.2.2 Presence of Saharan dust

In addition to backward trajectory analysis, commonly used in the studies of transport patterns of air masses, other modeling tools have been used for aerosol source identification. Considering that a large portion of atmospheric particulate matter is derived from desert regions, a number of dedicated atmospheric models have been developed

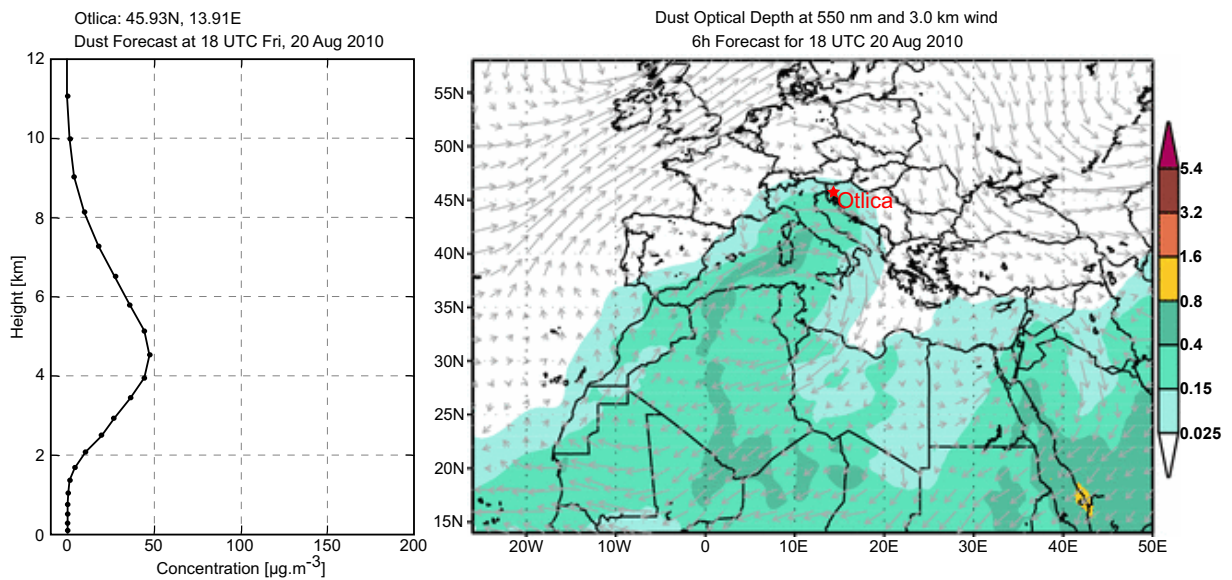


Figure 5.4: The presence of Saharan dust over Otlica predicted by the DREAM model on 20 August 2010. Left: dust concentration with height; Right: distribution of dust optical depth at 550 nm and wind directions at a altitude of 3.0 km. Red star denotes the location of the Otlica observatory.

to predict the presence of mineral dust and assess their impacts on air quality and climate. Presence of Saharan dust in the Mediterranean region is modeled by the Dust Regional Atmospheric Model (DREAM)<sup>2</sup>, designed to simulate and/or predict atmospheric cycle of mineral dust aerosols (Nickovic et al., 2001). The model solves Euler-type non-linear partial differential equation for the dust mass continuity and considers all major atmospheric processes for the dust cycle. During the integration, fluxes of surface dust injection were declared as deserts over the model cells. Once injected into the air, dust is then driven by the atmospheric variables: by turbulence in the early stage when dust is lifted to the upper levels; by winds when traveling away from the sources; and finally, by thermodynamic processes, rainfall and land cover features which provide wet or dry dust deposition. DREAM model is at the present providing operational dust forecasts for the Mediterranean region (affected directly by the Sahara desert) and for East Asia (affected by the Taklamakan desert) in the form of optical depth maps and vertical profiles of dust concentration in 6 hour intervals. The model is also validated through ground-based and remote sensing observations in collaboration with other research groups. In this study, the presence of the possibility of Saharan dust above Otlica was identified by both the DREAM prediction and back trajectory of

<sup>2</sup>Available at: <http://www.bsc.es/projects/earthscience/DREAM>

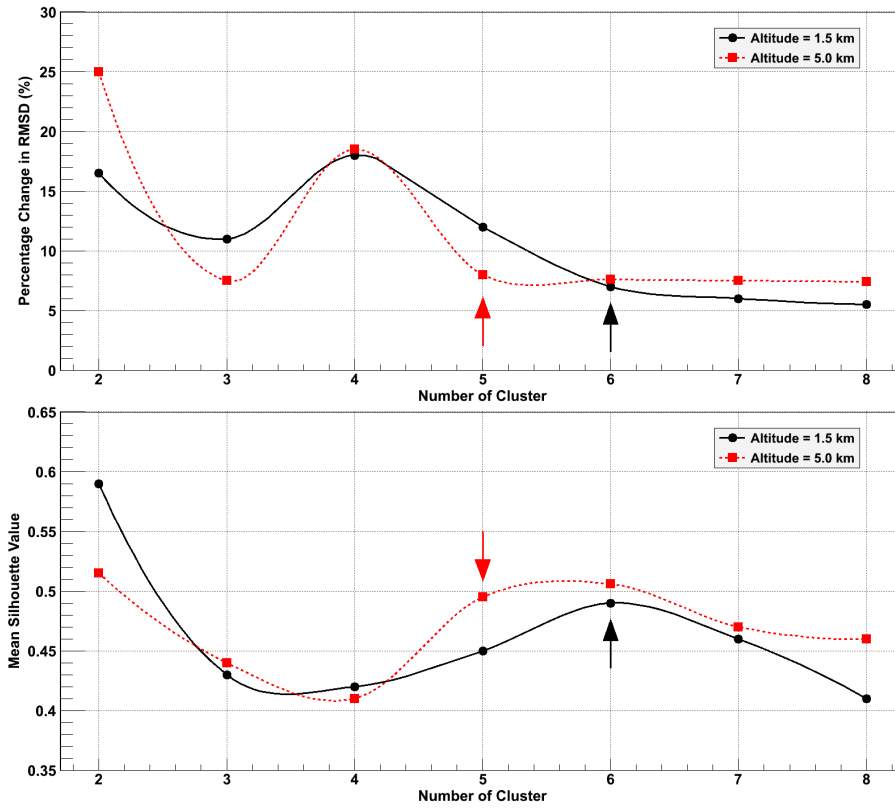


Figure 5.5: Changes in Root Mean Square Deviation (RMSD) and silhouette values calculated for sets of clusters at the lower and upper atmosphere.

air mass. An example of the DREAM prediction for Otlica on 20 August 2010 is shown in Fig. 5.4.

### 5.3 Cluster analysis of backward trajectories

To group transport paths of similar history and origin, cluster analysis was performed by the non-hierarchical K-means algorithm (Kaufman and Rousseeuw, 2005), which minimizes the Euclidean distance between the points on the trajectory and the centroid of the cluster. Since the optimum number of clusters is not a priori fixed by the clustering algorithm, it was determined using the Silhouette method (Kaufman and Rousseeuw, 2005) and the Root Mean Square Deviation (RMSD) method (Dorling et al., 1992), with the high silhouette value for the candidate number and the following small change relative in the RMSD. We observed that transport patterns at different heights in the upper atmosphere are very similar, while they differ significantly at



lower altitudes (Fig. 5.3). For the purpose of this study, circulation was differentiated between the two layers 5.0 km and 1.5 km. Optimal number of clusters for these layers was found to be 5 and 6, respectively (Fig. 5.5). Mathematical details on clustering are presented in the Appendix.

## 5.4 Long-term variation of the boundary layer height

The behavior of the atmospheric boundary layer (ABL) is directly influenced by the Earth's surface. In the daytime, surface emissions usually mix throughout the depth of the ABL due to the convection and vertical wind shear. In this case, the ABL can be referred to as a convective boundary layer and the ABL height is variable in space and time. On the other hand, a stable boundary layer can be formed in stable atmospheric conditions, where comparatively drier air from the free troposphere (FT) doesn't penetrate into the ABL and surface emissions don't mix with higher atmosphere. The top of the ABL can thus be determined by a sharp increase in temperature and a sudden drop in the concentration of water vapor and particles. In this study, where all measurements were performed after the sunset, stable boundary layer was found on most measured days by both lidar and radiosonde measurements (Fig. 5.2), with increasing potential temperature with height. ABL height was then estimated simply as the height of the first strong decrease (significant negative gradient) in the lidar signal of aerosol backscatter starting from the ground level (Russell et al., 1974). However, this method is not always reliable at Otlica (less than 10 % of all measured days), due to the occurrence of sea breeze circulation and the presence of Saharan dust at lower altitudes, even below 2 km a.s.l. (Fig. 5.4). In this case, the ABL height was determined as the height below which most aerosols were contained, even if the layer was not well-mixed (typically about 2 km above sea level), which again compared well to radiosonde-derived value.

Daily variation of the ABL height from August to October 2010 is shown in Fig. 5.6 a. Lidar-derived ABL heights were found to be in a good agreement with the radiosonde observations, with a correlation coefficient of 0.83 and an offset of about 0.4 km (Fig. 5.7). The good correlation implies that both locations (Otlica and Ljubljana) were influenced by similar synoptic conditions. The reasons for the uncertainties may be, in addition to the displacement of the two measurements by 40 km and thus different local topographical and meteorological properties, also the difference in level of urbanization at the two measuring sites (city/mountain) and different nature of the

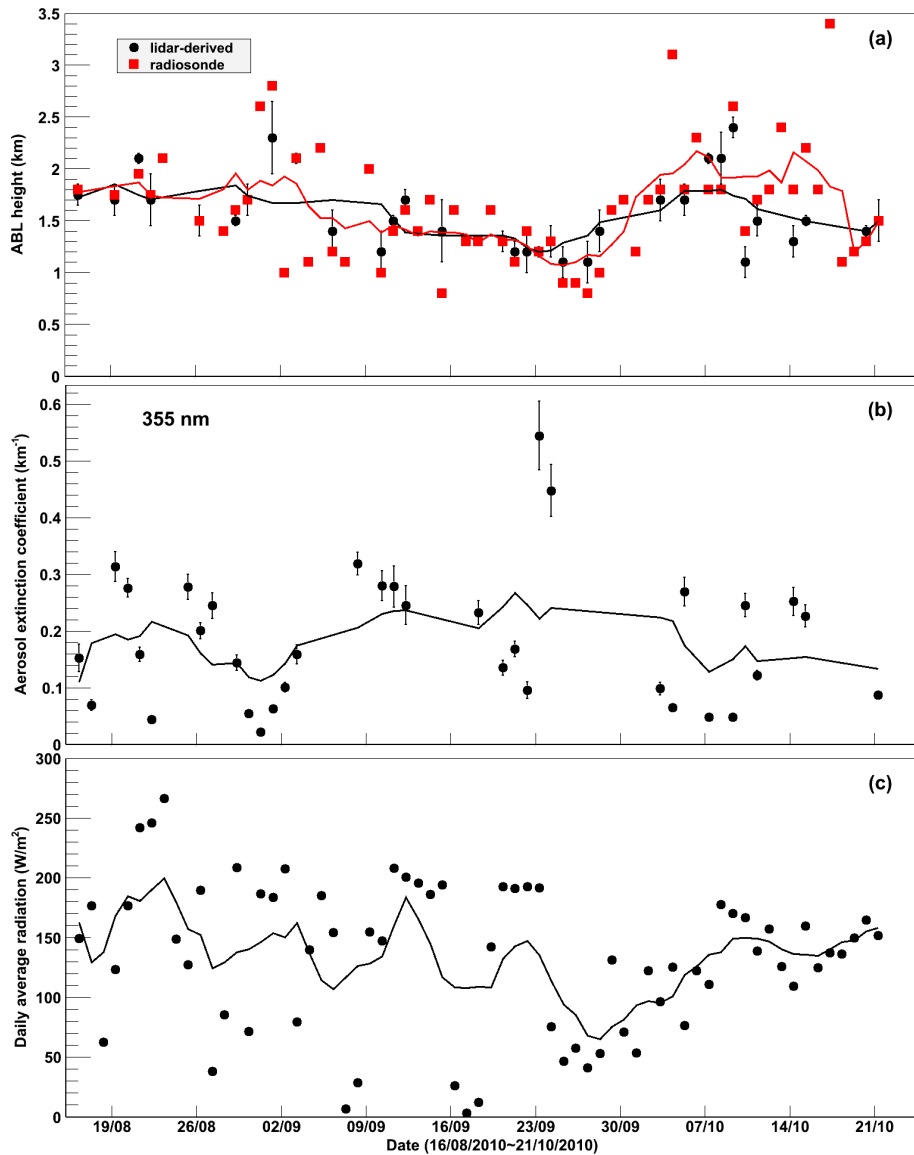


Figure 5.6: Observations at Otlica from August to October 2010: (a) comparison of radiosonde and lidar-derived ABL heights, (b) daily evolution of the average aerosol extinction coefficient at 355 nm within the boundary layer, (c) daily average solar radiation. Solid lines represent results of 7-day sliding average.

two measurements. Lidar-derived ABL height is a result of averaging of lidar data over several hours after sunset, while the radiosonde-derived ABL height comes from a single measurement at 2 AM. We observed many cases where the presence of Saharan dust within the lower atmosphere strongly decreased within hours. Our previous study (Gao et al., 2011a) also demonstrated that the ABL height above Otlica can in



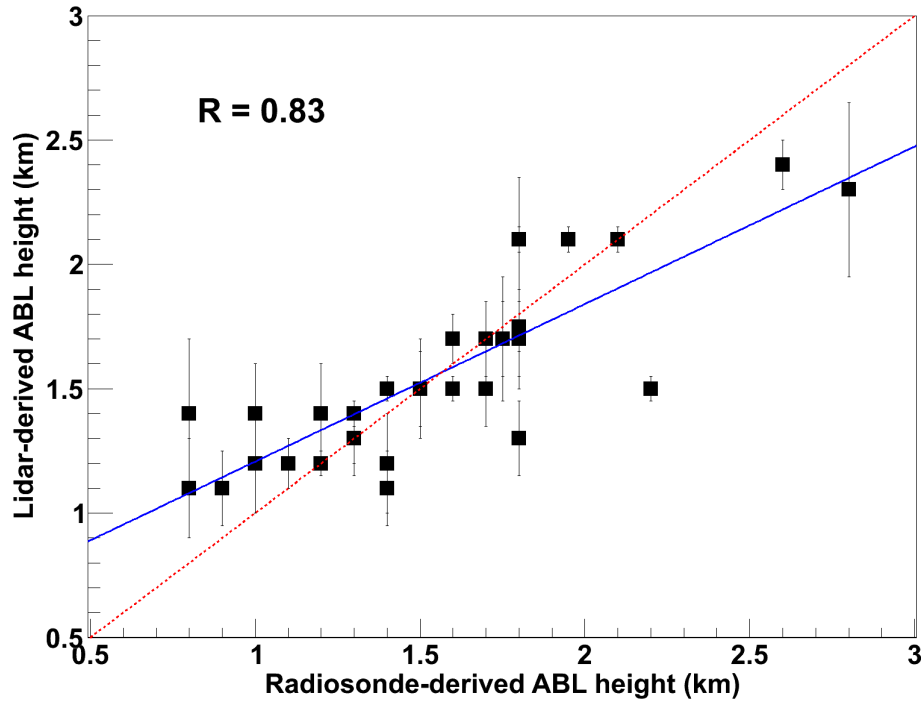


Figure 5.7: Comparison of the ABL height from lidar and radiosonde measurements from August to October 2010.

windy meteorological conditions significantly and rapidly change in a few hours. The uncertainties were considered when we calculated the AOD columns within the ABL. Figure 5.6 a also reveals that ABL height gradually decreased during the late summer (between August and September) and reached a plateau in October. This behavior could be related to meteorological conditions as decreased solar radiation in October resulted in smaller surface thermal convection (Fig. 5.6 c), which in turn resulted in the decrease of the ABL height in comparison to extremely hot summer season, characterized by the subtropical highs. Moreover, the arrival of colder weather was characterized by incoming cyclone and strong winds, lifting the air close to the ground to upper troposphere, which also contributed to an increase in boundary layer height. The average value of the ABL height from August to October was found to be  $1.6 \pm 0.6$  km above sea level, with the highest daily value of 3.4 km observed on 17 October 2010 and the lowest of about 0.8 km on 27 September 2010. High variability of the ABL height indicates its strong day to day dependence on meteorological conditions. The average aerosol extinction within the ABL (Fig. 5.6 b) was however, found to be almost consistent during the measuring campaign, except for a few days in September with about twice higher values than in all other measurements. At that time, ABL was rela-

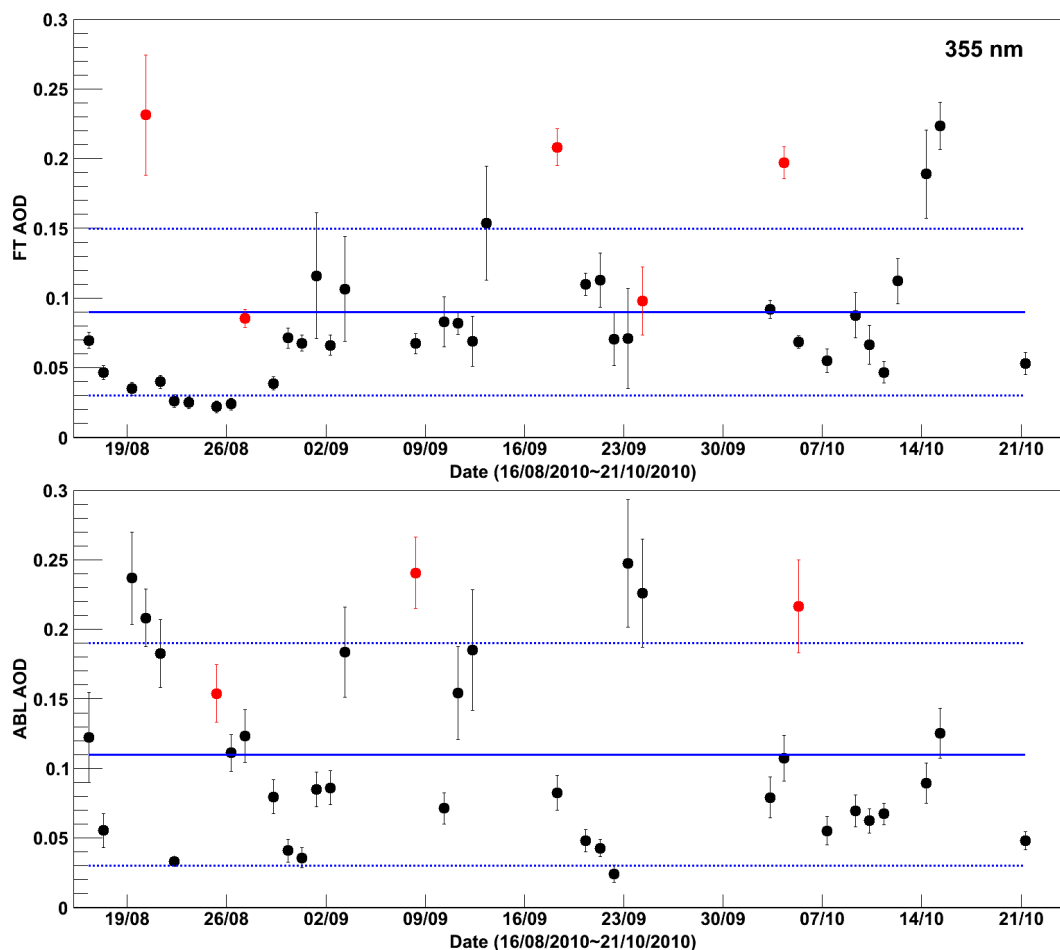


Figure 5.8: Daily variation of lidar-derived aerosol optical depth at 355 nm in free troposphere (top) and boundary layer (bottom) from August to October 2010 at Otlica, Slovenia. Red data points denote the days when both DREAM model and back trajectories predict the presence of the possibility of Saharan dust.

tively stable and low (about 1.2 km). High extinction values may in this case be due to increased intake of aerosols from the ground, which remained in the ABL.

## 5.5 Impact on local environment

The effects of aerosol presence on the atmosphere was characterized by aerosol optical depth (AOD). As the ABL directly interacts and thus stronger affects the surface, AOD was separately obtained for the ABL and the FT. Daily variations of both are shown in Fig. 5.8. Average AOD value within the ABL was found to be  $0.11 \pm 0.08$  and  $0.09 \pm 0.06$  in the FT. Particular topographical and meteorological properties of

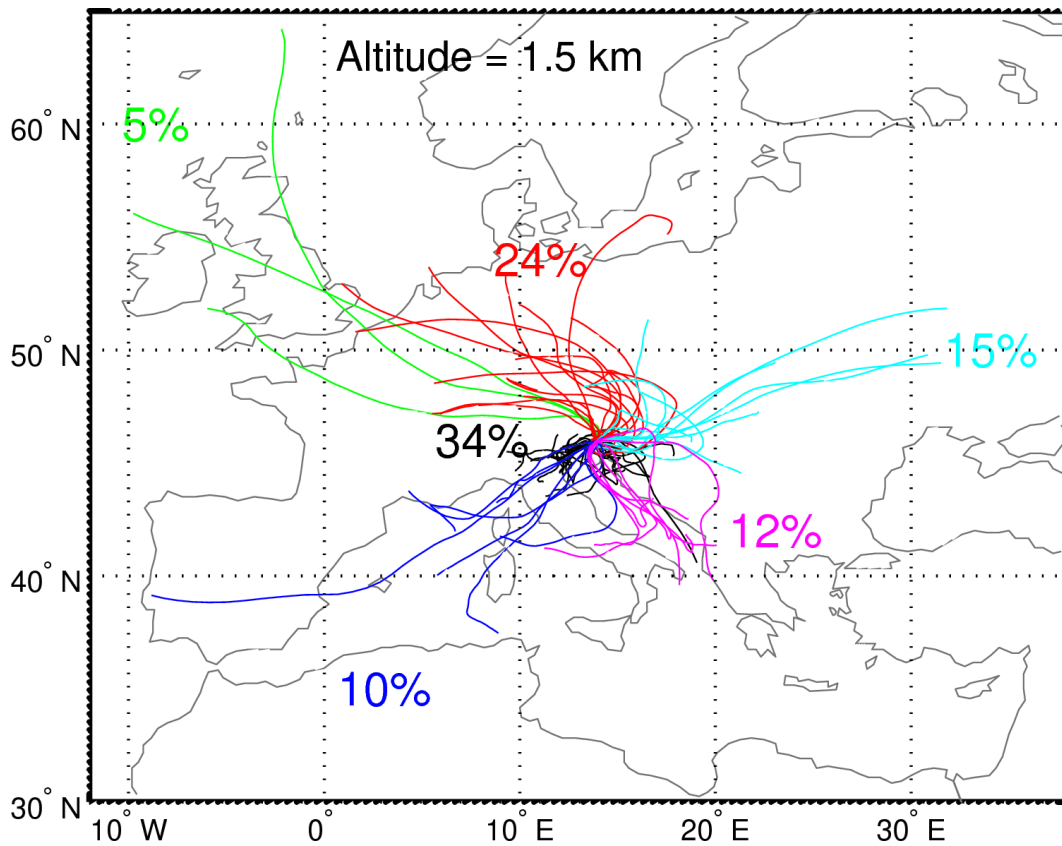


Figure 5.9: Results of the cluster analysis of the backward trajectories arriving at Otlica at 1.5 km at 2100 UTC within the time of the lidar observations from August to October 2010. The percentage of the contained trajectories of each cluster is also given.

the high-altitude measuring site (945 m a.s.l.) with relatively low ABL height (about 1.6 km) and few anthropogenic sources in this area resulted in a large contribution of the FT particles to the total tropospheric aerosol loading. Particles in the free troposphere thus on the average represented 45 % of the total tropospheric particulate matter, with the fraction ranging from 12 % for clean FT to 74 % for the cases with strong presence of Saharan dust. The variability of the AOD in the ABL was found to be high, with the values ranging from 0.02 to 0.25. As local anthropogenic emissions are not expected to vary significantly, the observed AOD in the ABL are mostly related to the meteorological variability. To investigate the dependence of the AOD on the origin of air masses, backward trajectories arriving at Otlica in lower and in upper atmosphere were grouped separately. Figure 5.9 presents the results of the cluster analysis in the ABL, with the total fraction of trajectories contained in each cluster. Six classes represent the origin of the air masses, namely north (N), east (E), southeast (SE), southwest

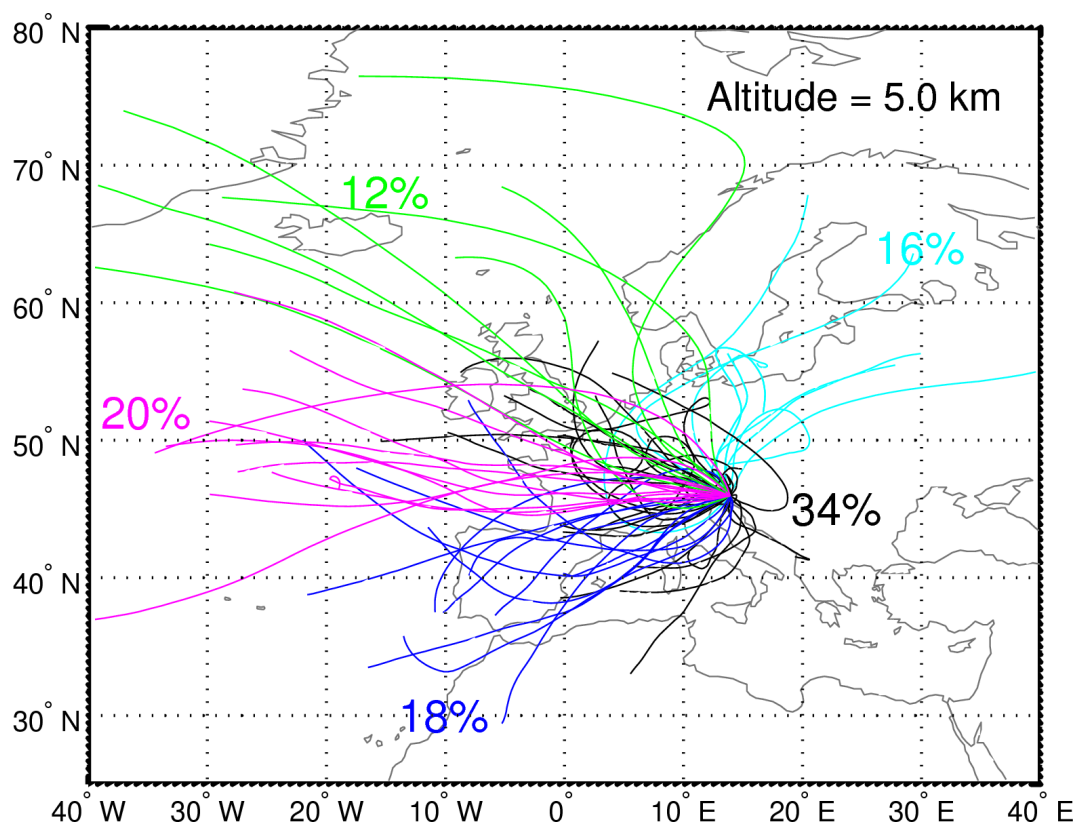


Figure 5.10: Results of the cluster analysis of the backward trajectories arriving at Otlica at 5.0 km at 2100 UTC within the time of the lidar observations from August to October 2010. The percentage of the contained trajectories of each cluster is also given.

(SW), northwest (NW) and center (C). Trajectories in the N class predominately originate from northern Europe, in the NW and W class from north Atlantic Ocean, in the SE class from the Balkans, and in the SW class from the Mediterranean and northern Africa. C class, which amounts to about 34 % of cases during the campaign, includes various local circulation patterns. Table 5.1 summarizes the mean AOD, the frequency of occurrence of each cluster in the FT and the ABL, and the concentrations of  $\text{PM}_{10}$  and  $\text{O}_3$  at the ground level.

In the upper troposphere, air masses mostly moved very fast with long transport patterns (Fig. 5.10) and as a result, a fraction of aerosols characteristic for the place of origin remained high. Background aerosol optical depth of the FT was on average found to be less than 0.1 at 355 nm, with pronounced low values during late August and almost constant values during September and October (Fig. 5.8). High FT AOD values (around 0.11) were associated with C class which contained European continental tropical air masses (about 34 % of all cases) and may be due to biomass burning

Table 5.1: Mean AOD values and concentrations of particulate matter (PM<sub>10</sub>) and ozone (O<sub>3</sub>) associated to different categories of backward trajectories. PM<sub>10</sub> concentrations were measured in Nova Gorica and O<sub>3</sub> concentrations at Otlica.

Layer	Cluster	Mean AOD	Occurrence	PM <sub>10</sub> (µg m <sup>-3</sup> )	O <sub>3</sub> (µg m <sup>-3</sup> )
<b>FT</b>	NE	0.08	16 %		
	C	0.11	34 %		
	SW	0.10	18 %		
	NW	0.09	12 %		
	W	0.05	20 %		
<b>ABL</b>	NW	0.04	5 %	12	75.2
	C	0.14	34 %	22	74
	N	0.09	24 %	20.6	85.8
	E	0.09	15 %	22.5	73.6
	SW	0.20	10 %	25	71.8
	SE	0.17	12 %	21.4	81.8

in surrounding regions in the harvest season. Classes SW and NW contained air trajectories for days with average FT AOD values. Classes NE and W class corresponded to low AOD values of about 0.05–0.08 due to the presence of maritime aerosols from the Arctic region and North Atlantic Ocean.

In the ABL, complex orography of the investigated terrain contributes to the development of complicated air circulation patterns, such as the Bora wind. As a result, a considerable amount of anthropogenic particles can be lifted above the boundary layer. In the three-month study, the ABL in the Otlica region was mainly (85 % of the time) affected by local recirculations of air (C class), slowly moving air masses from northern Europe (N class), eastern Europe (E class) and the Balkans (SE class), mainly be due to the influence of the Atlantic high pressure anticyclone. The resulting regional low pressure gradient conditions at the lower troposphere were frequently present. ABL AOD values on days grouped into C class range between 0.03 to 0.24. Lowest ABL AOD values (0.02–0.07) were found to be associated with the NW class, which includes rapidly moving air masses from Arctic region (observed about 5 % of the time) and highest with the SW class (observed about 10 % of the time) which includes air flows from north Africa, passing over the Mediterranean Sea, resulted a very high AOD in the ABL on the average value of about 0.2. Mixing of Saharan dust with maritime aerosols carried by tropical maritime flows could be a major contribution to the total

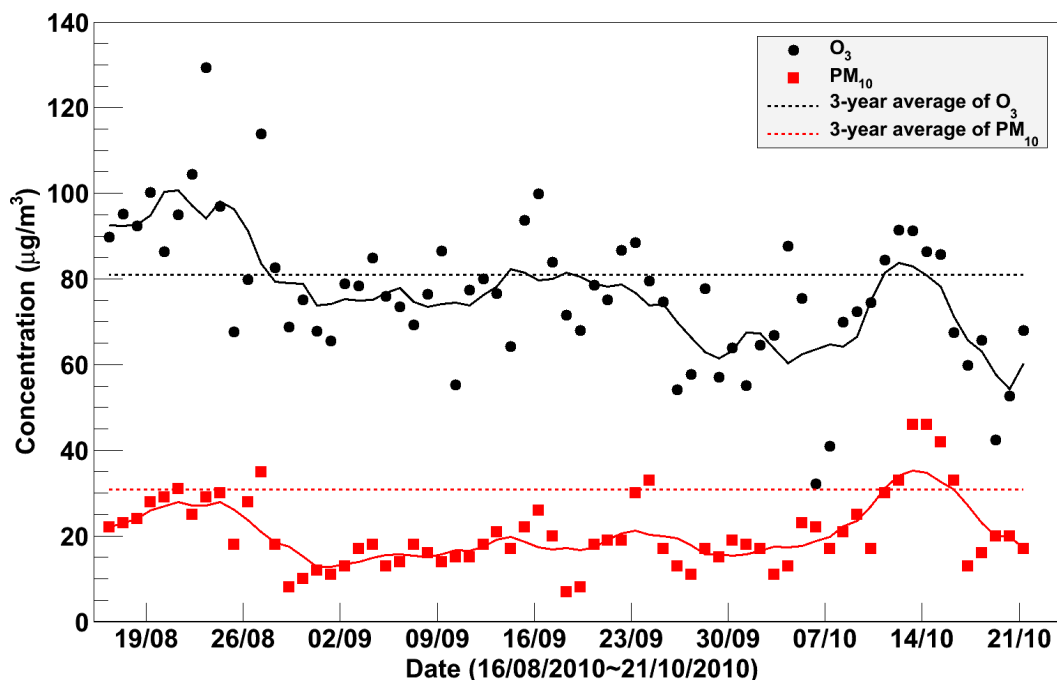


Figure 5.11: Daily evolution of  $O_3$  and  $PM_{10}$  concentrations from August to October 2010, obtained from the ground-based measurements. Solid lines represent results of 7-day sliding average.

aerosol loading.

The presence of Saharan dust in either ABL or FT was predicted by DREAM model for 16 days during the monitoring period. Due to low clouds and precipitation, lidar measurements were performed on 8 of these days, yielding 3 cases of increased aerosol content in the ABL and 5 cases in the FT. Air mass trajectories for the corresponding days were predominantly grouped into the SW class, which supports the DREAM prediction. Days with the FT AOD values larger than one standard deviation above the campaign's average in 60 % of cases corresponded to Saharan dust events (Fig. 5.8). On 20 August 2010, the largest presence of Saharan dust was observed, yielding a value of the FT AOD of 0.23. An attempt was made to correlate extreme ABL AOD values with Saharan dust as well, however, the matching efficiency in this case was only 33 %. During the campaign, dust contributed almost 37 % to the integral FT AOD and 14 % to the ABL AOD.

In order to assess the influence of different types of aerosols from various sources on local environment, daily concentrations of  $O_3$  and  $PM_{10}$  during the monitoring campaign (Fig. 5.11) were also related to the clusters of air mass trajectories within the ABL (Table 5.1). The observed  $O_3$  concentrations were found to be consistent with the three

year average ( $81 \mu\text{g m}^{-3}$ ), with about 20 % increase above the average in August and apparently low in late September and early October. In the case of the C class, which represents local air flows and amounts up to 34 % of all measured cases,  $\text{PM}_{10}$  and  $\text{O}_3$  concentrations at the ground level were found to be comparatively low. The result implies that during the campaign, local pollution sources did not contribute significantly to the decrease in air quality. High concentrations of  $\text{O}_3$  are associated with the SE cluster, which mostly contains trajectories bringing over air masses from the Balkan region. Surprisingly,  $\text{PM}_{10}$  values in this class are relatively low. Highest values of  $\text{O}_3$  concentrations were found for the trajectories from the N cluster, carrying air masses over the highly industrialized northern and central Europe. In all cases, increased  $\text{O}_3$  concentrations imply transport of pollutants into Slovenia; significant increase of  $\text{O}_3$  levels can be detected in rural areas as far as 400 km downwind from industrial zones (Jorba et al., 2005). Differences in  $\text{O}_3$  concentrations between clusters SE and N indicate different extent of pollution in the region of origin and different average length of trajectories.

Regarding ground-based monitoring of aerosols, highest concentrations of  $\text{PM}_{10}$  were found to be correlated to the trajectories belonging to SW cluster, in particular for those carrying Saharan dust as predicted by the DREAM model. Air flows, as north-western however, are characterized by low  $\text{PM}_{10}$  concentrations, with an average value of  $12 \mu\text{g m}^{-3}$ . As the  $\text{PM}_{10}$  monitoring site was located in urban environment of Nova Gorica,  $\text{PM}_{10}$  concentrations were expected to be more affected by local emissions than by incoming air masses, however, in the campaign this was not found to be the case. Although the maximum daily concentration of  $\text{PM}_{10}$  increased up to  $45 \mu\text{g m}^{-3}$  in the middle of October, most daily average values were apparently lower than the three year average of  $30.6 \mu\text{g m}^{-3}$ . Long term observations show that in the autumn the  $\text{PM}_{10}$  concentrations are generally relatively low (i.e. also during our campaign), while the highest mean concentrations were observed in the winter time.

## 5.6 Conclusions

Long range aerosol transport was studied using three months of lidar monitoring data, with precipitation and low altitude cloud overcast days excluded. Remote sensing data were complemented by meteorological and environmental data ( $\text{PM}_{10}$  and  $\text{O}_3$  concentrations). We have found that the ABL height was highly variable and related to local meteorological conditions. ABL heights derived from lidar data at Otlica are com-

parable to the values obtained from radiosonde measurements in Ljubljana although the locations are quite far apart (40 km), the coefficient of linear correlation between the two was found to be 0.83. The type and origin of the detected aerosols was investigated using the modeling of backward trajectories of air masses and their subsequent clustering. Values of aerosol optical depth (AOD) provided by remote sensing were found to be related to the different categories of the air masses arriving to Slovenia. High ABL AOD values can be associated with local circulation of air and slow motion of air masses from the Balkans, while low AOD values correspond to northwestern flows. Highest ABL AOD values (and  $\text{PM}_{10}$  concentrations) were observed for southwestern air masses originating from north Africa, while those from southeast and north result in elevated  $\text{O}_3$  concentrations. It was also found that on the average, aerosols in the free troposphere contribute about 45 % to the total tropospheric aerosol loading.



## Observation of atmospheric structure over complex terrain

Observations of tropospheric structure over complex terrain are very important to understand the impact of topography on air physics and dynamics. Complex terrain is capable of inducing circulations that lift particulate matter and trace gases into the free troposphere (e.g., [Henne et al., 2004](#)). As a result, complex terrain air flows may have a significant impact on air quality and surface radiation balance. Extensive ground-based observations, needed to evaluate numerical simulations are difficult to perform due to terrain complexity and the difficulty of accurate representation of sub-grid scale processes. A solution, explored in this chapter, is using lidar-based remote sensing. The preliminary study of tropospheric structure over Trnovski gozd plateau, divided by the Vipava valley from the Karst plateau in Slovenia was discussed.

### 6.1 Geographic location and experiments

In the southwestern part of Slovenia, within the distance of about 30 km from the Adriatic coast, the terrain first rises to Karst plateau (up to 643 m a.s.l.), then descends into the deep Vipava valley (about 100 m a.s.l.) and rises again to Trnovski gozd, Hrušica and Nanos (around 1500 m a.s.l.) plateaus (Fig. 6.1 and Fig. 6.2). Atmospheric processes over this region, which is known for extremely strong Bora winds ([Alpers et al., 2007](#)) in the winter, have not yet been fully investigated. A preliminary study of the tropospheric structure over the southwest region of Slovenia was performed on 12 October 2011 from 17:00–20:00 CET simultaneously using two long-range scanning lidars with their lines of sight crossing above the Vipava valley. One of the lidars was the scanning stationary Mie lidar at Otlica observatory (45.93° N, 13.91° E, 945 m a.s.l.), operating in ultraviolet range (355 nm). This device performed vertical scanning

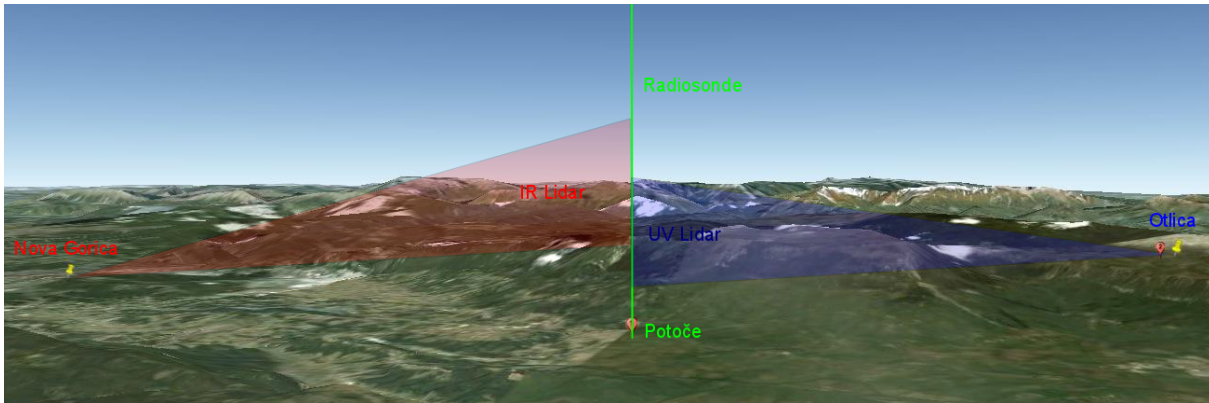


Figure 6.1: Birds-eye view of the study region with indicated lidar scanning regions and radiosonde ascent site within the Vipava valley. An IR (1064 nm) lidar was located at Nova Gorica ( $45.96^{\circ}$  N,  $13.64^{\circ}$  E) and a UV (355 nm) lidar was operated from Otlica ( $45.93^{\circ}$  N,  $13.91^{\circ}$  E). The radiosonde was launched at the intersection point of the two lidar traces at 19:00 CET.

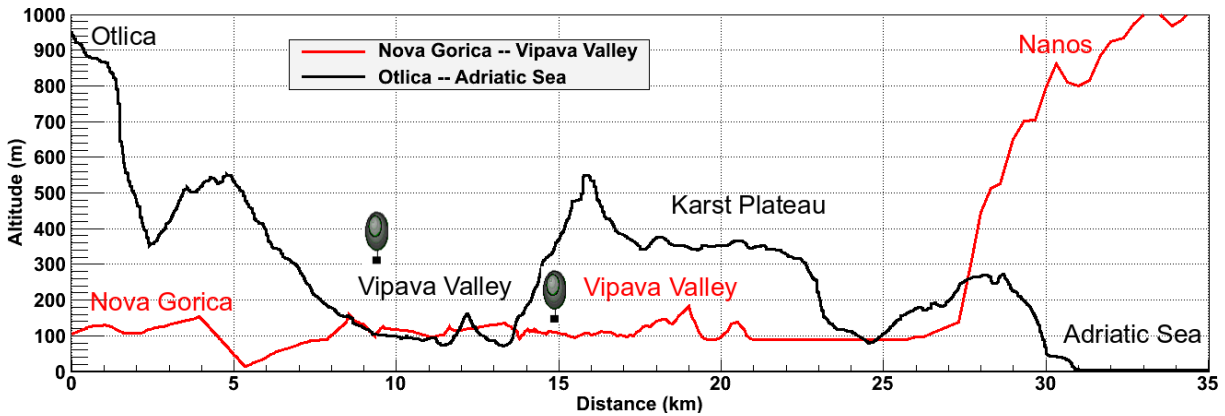


Figure 6.2: Elevation profiles along the lidar lines of sight with indicated radiosonde launch position. The black profile represents line of sight of the Otlica (UV) lidar and the red profile of the Nova Gorica (IR) lidar.

with a fixed azimuth angle of  $235.1^{\circ}$ . With a maximum detectable range about 40 km, it provided information on aerosol loading over the Vipava valley and Karst plateau (Gao et al., 2011a). The other scanning Mie lidar (He et al., 2010) was located at Nova Gorica ( $45.96^{\circ}$  N,  $13.64^{\circ}$  E, 107 m a.s.l.), operating in infrared range (1064 nm). This lidar directed at an azimuth angle of about  $109^{\circ}$ , was providing information on aerosol loading along and above the Vipava valley.

Scanning lidars are useful tools for the study of atmospheric structure because of

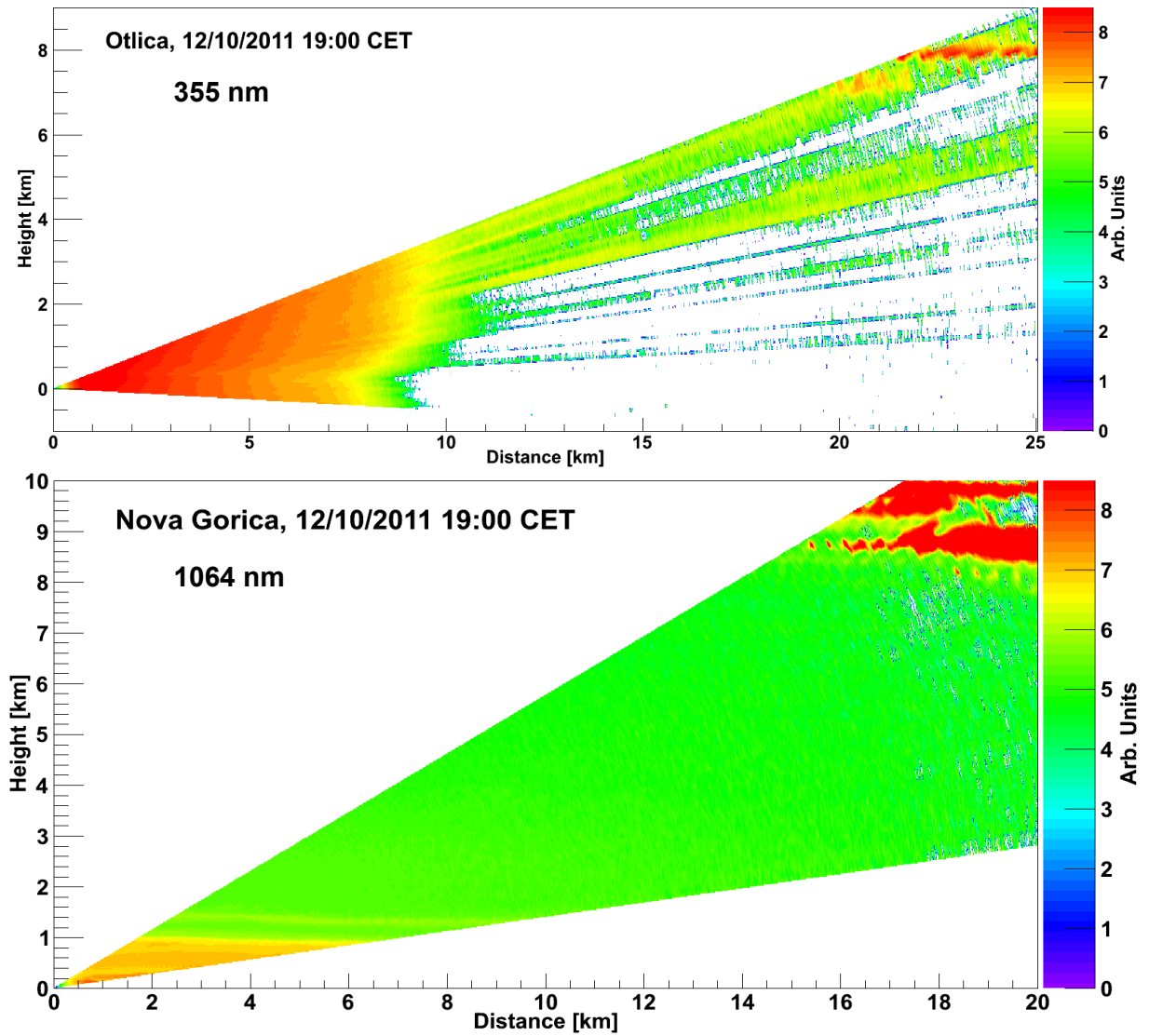


Figure 6.3: RHI scans of range-corrected lidar returns by the Otlica lidar (top) and the Nova Gorica lidar (bottom) simultaneously taken at the exact time of radiosonde ascent (12 October 2011 at 19:00 CET). Height is given relative to the altitude of the lidar site. A thick layer of clouds at the altitude of about 9 km a.s.l. can be seen from both lidar measurements.

their fine spatial and temporal resolution. Two-dimensional temporal and spatial distributions of aerosols were visualized from range height indicator (RHI) scans constructed from lidar data. At Otlica, scanning was performed for elevation angles between  $-3^\circ$  and  $20^\circ$  and in Nova Gorica for angles between  $8^\circ$  and  $30^\circ$ . In both cases the angular step between successive measurements was  $0.5^\circ$ . Throughout the study both devices provided a new RHI scan every 8 minutes. In addition, in collaboration with

Slovenian Armed Forces, a dedicated radiosonde<sup>1</sup> was launched at 19:00 CET at the intersection point of the two lidar traces at Potoče (45.89° N, 13.82° E, 113 m a.s.l., see Fig. 6.1). The launching site was about 9.2 km away from Otlica along the line of the lidar sight and 14.8 km from Nova Gorica (Fig. 6.2).

An example of simultaneous RHI scans taken by both systems is shown in Fig. 6.3, where a thick layer of clouds can be seen at the altitude of about 9 km a.s.l. From the lidar detection at 1064 nm the ABL was found to be up to 1 km a.s.l. and the presence of aerosol layers within it can be clearly visible. Stratified atmosphere was found in the lower troposphere, up to about 2 km a.s.l. Above this height atmosphere was relatively clear up to the layer of clouds. From the lidar detection at 355 nm, stratification can not be directly seen due to the high contribution of molecular scattering to the lidar return signal, which can however smear out the features of low aerosol concentrations. In the case of Otlica lidar, atmospheric stratification was obtained from the features of the aerosol extinction coefficient.

## 6.2 Lidar-based measurements of tropospheric structure

Stable boundary layers can be identified from RHI lidar scans which show horizontal stratification of the atmosphere. The top of a stable ABL manifests a strong decrease of aerosol loading and thus of the lidar return signal (Fig. 6.4). The observations of the ABL on 12 October 2011 showed that the ABL structure noticeably evolved in time, however, the height remained almost constant at about 1.2 km a.s.l. during the scanning. ABL structure obtained from lidar data was at 19:00 CET confirmed by radiosonde observations (Fig. 6.6). The observation of an elevated aerosol layer at about 1.5 km a.s.l. at 18:10 CET manifested the potential of the mobile lidar reveal optically thin structures above the ABL. The bands with different aerosol loading in the ABL can be associated with the layers of air masses with different wind speeds and directions. The winds with various directions were found within the ABL, with low speeds about 5 m/s. Above the boundary layer, the wind speeds rapidly increased to about 30 m/s and the synoptic flow from northwestern Alps region was observed.

Furthermore, we have observed that the ABL became stable only after the sunset (at about 17:30 CET). At 17:15, the top of the boundary layer was still found to be perturbed, while in later measurements it became uniform and the atmosphere can be considered horizontally homogeneous. In such conditions, mixing of the air and

---

<sup>1</sup>ZEEMET™ Mark II MICROSONDE, Sippican, Inc.

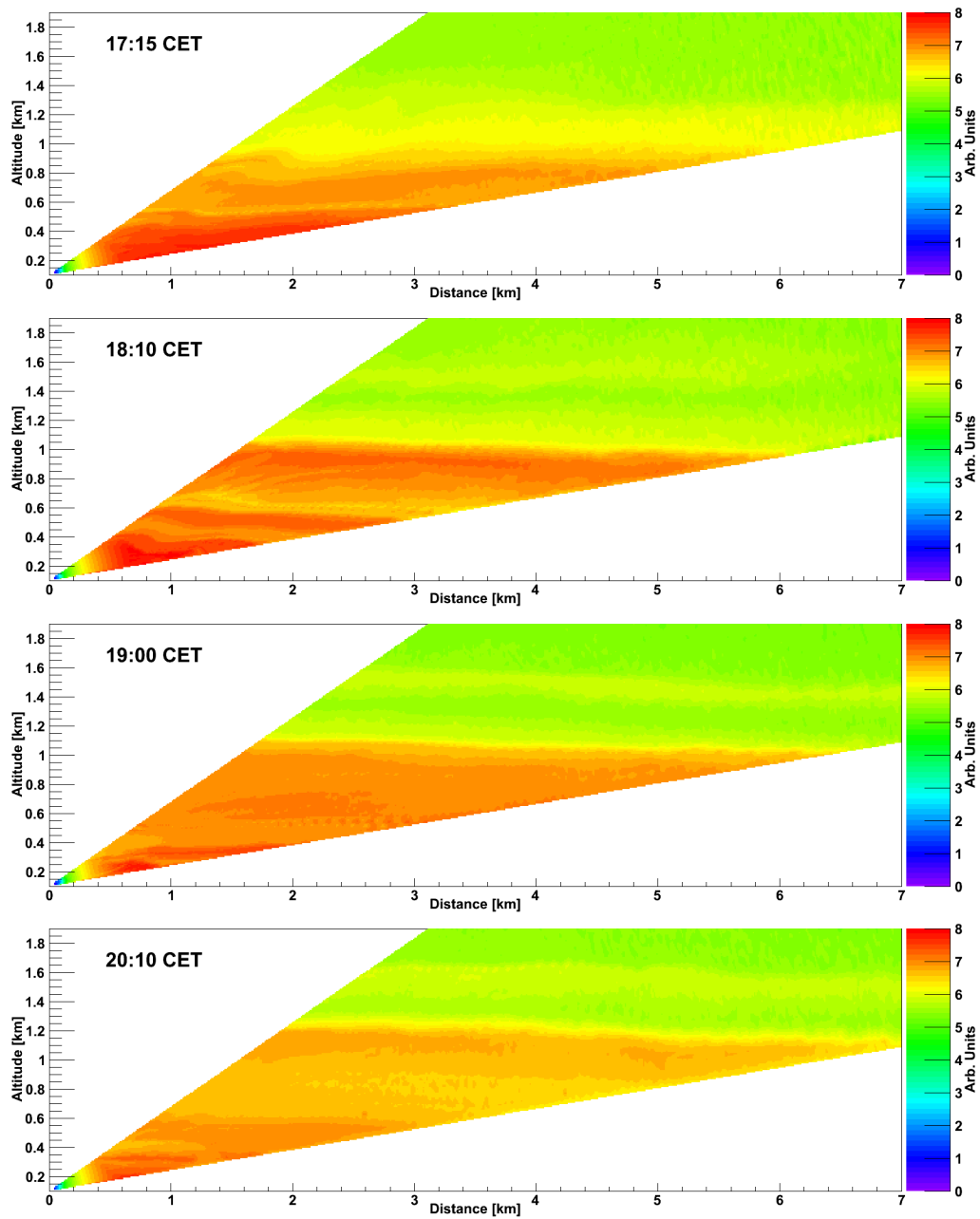


Figure 6.4: Time series of RHI scans by the Nova Gorica lidar taken from 17:00–20:30 CET on 12 October 2011. The plots show range-corrected lidar signal for elevation angles from  $8^\circ$  to  $30^\circ$ .

turbulence are strongly damped and emissions from the surface tend to remain concentrated in a layer close to the surface. In this layer (about 300 m above the ground), aerosol loading was found to be high (Fig. 6.5) and the layer itself horizontally hetero-

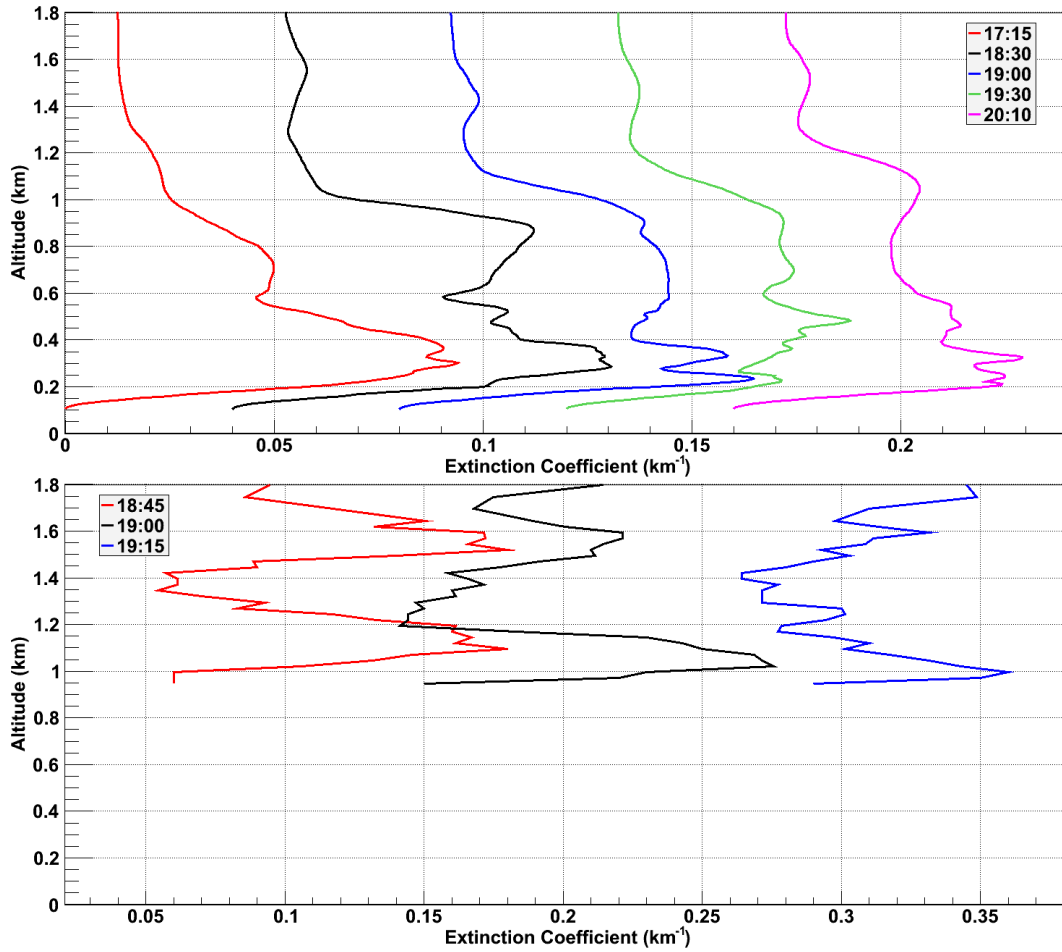


Figure 6.5: Time series of consecutive vertical atmospheric extinction profiles by the Nova Gorica IR lidar (top) with an increment of 0.04 between successive profiles and Otlica UV lidar (bottom) with an increment of 0.1. Both datasets were taken between 17:00 and 20:00 CET on 12 October 2011. The profiles show two-layer aerosol structure with the atmospheric boundary layer reaching up to about 1.2 km a.s.l. and the elevated layer at about 1.5 km.

geneous.

Time series of consecutive vertical aerosol extinction profiles, obtained with both lidar devices are shown in Fig. 6.5. The profiles show that two-layer aerosol structure was present during the scanning, with the boundary layer reaching about up to about 1.2 km a.s.l. and an elevated layer at about 1.5 km. The observed structure could be a result of thermally driven upslope flows and compensating sinking motions away from the slope (De Wekker, 2008).

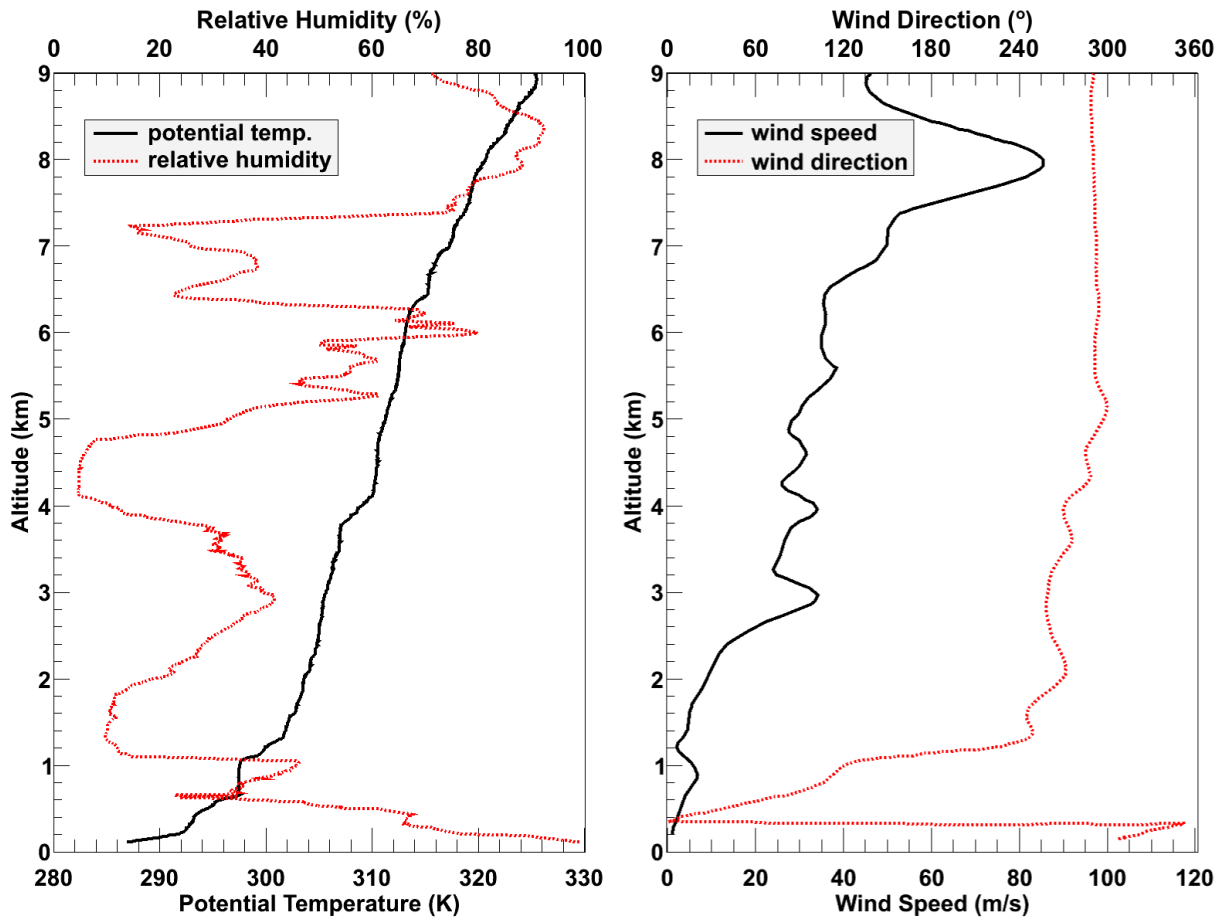


Figure 6.6: Vertical profiles of potential temperature and relative humidity (left), and wind speed and direction (right) as obtained from radiosonde ascent from Potoče at 19:00 CET on 12 October 2011.

### 6.3 Radiosonde measurements of tropospheric structure

In the evening, when the solar heating ends and the surface cools faster in stable atmospheric conditions than the air above through radiative cooling, the temperature does not decrease with height, but rather increases (known as temperature inversion). A stable boundary layer is formed when persistent temperature inversion conditions exist, so that a vertically displaced parcel of air tends to return to its original position. Thermodynamical structure of the atmosphere on 12 October 2011 was obtained from radiosonde measurements performed at 19:00 CET (Fig. 6.6). The top of a stable boundary layer is evident from a strong increase of the potential temperature at 1.2 km a.s.l., which spatially exactly corresponds to the peak in the lidar return signal. The



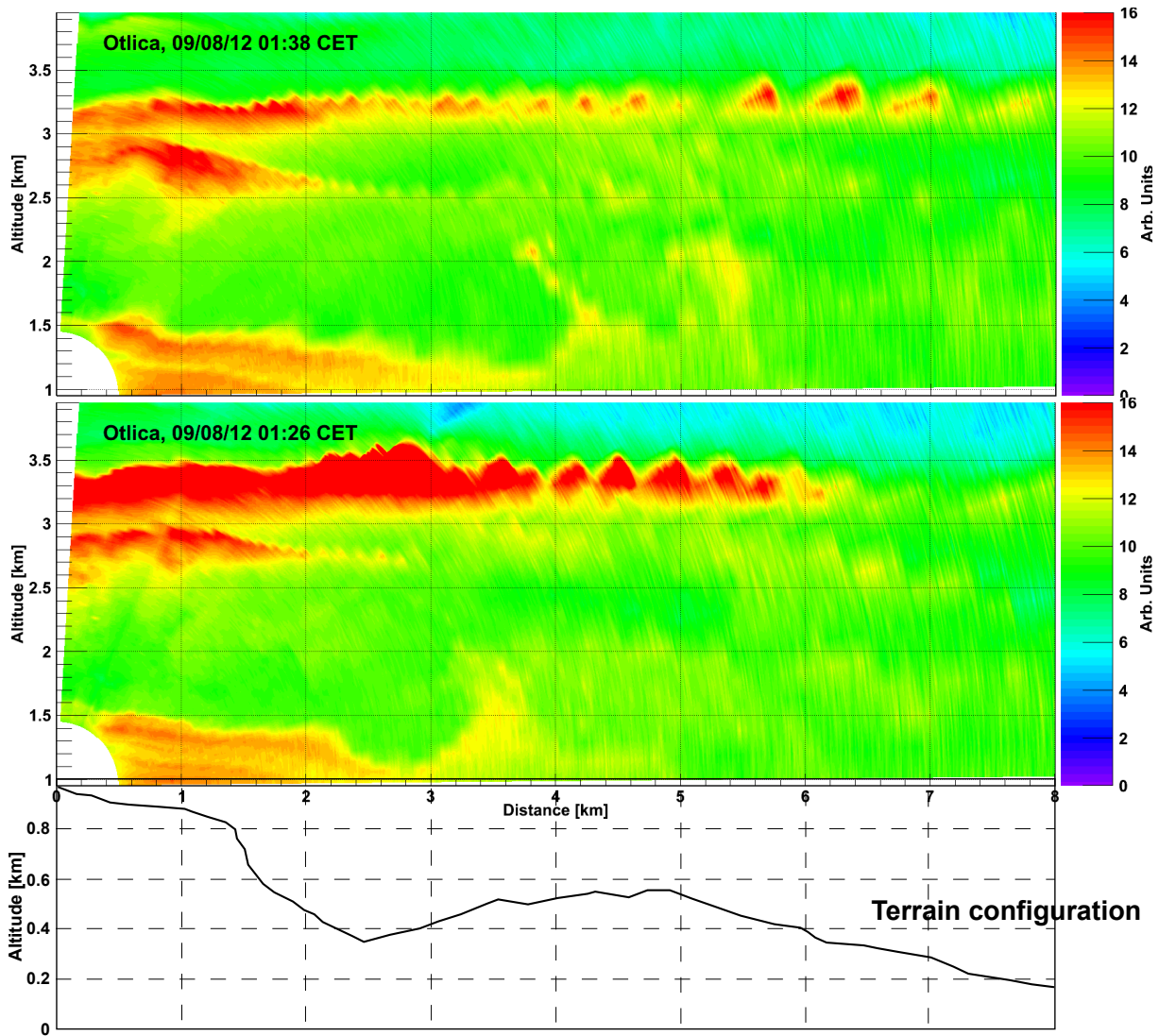


Figure 6.7: Example of RHI scans obtained with scanning lidar, showing the aerosol dispersion over mountainous terrain.

presence of the cloud layer results in a peak in relative humidity at 9 km, reaching up to about 90 %.

## 6.4 Discussion

The present study is the first attempt to investigate the feasibility of using a combination of scanning lidars and radiosondes as tools for the investigation of atmospheric structure over complex terrain of southwestern Slovenia. The attempted approach pro-



vides good visualization of atmospheric structure. Due to the uneven terrain and rapid drop of cold air masses from the adjacent mountain ranges to the sea, the region is often characterized by mountain-valley winds, which however is not the case during the campaign. Other experiments (Fig. 6.7) performed at Otlica show that the scanning elastic lidar could contribute to an improved understanding of aerosol dispersion and wind formation processes over this mountainous terrain. We expect that a similar approach for wind formation processes could be used in the future to investigate the behavior Bora wind which is an important meteorological phenomenon in this region.



## Conclusions and perspectives

Study of atmospheric aerosol transport processes on local and regional scales, using combined lidar-based remote sensing, radiosondes and in-situ ground-based measurement techniques were performed as a part of this dissertation. Scanning lidar measurements in particular were most critical for the monitoring of transport and dilution of aerosol plumes as well as identification of aerosol sources. Based on the results and the experience gained, we can draw a number of conclusions both regarding lidar instrumentation as well as regarding the possibilities of future research in the field.

### Lidar instrumentation

Based on the obtained results, we can conclude that the Mie scanning lidar at 1064 nm that was used in the process already has the capability for providing spatial and temporal visualizations of aerosol loading in the atmosphere. Experiments demonstrated that a combination of lidar-based remote sensing and in-situ ground-based measurements provided interesting information on meteorological phenomena and their effects on the environment. Throughout the study, the performance of the scanning mobile lidar has been analyzed and improved in both the hardware and the software. An example of these improvements is three-dimensional automated scanning functionality of the device, which provided the possibility of continuous environmental monitoring in the desired solid angle around the lidar site. Considering that range height indicator (RHI) scans are generally performed to indicate two-dimensional distributions of atmospheric aerosols, absolute calibration of the elevation angle of the scanning lidar was performed at an elevated site (945 m a.s.l.) with the use of hard target returns from the sea surface about 40 km away. The calibration was found to be essential for

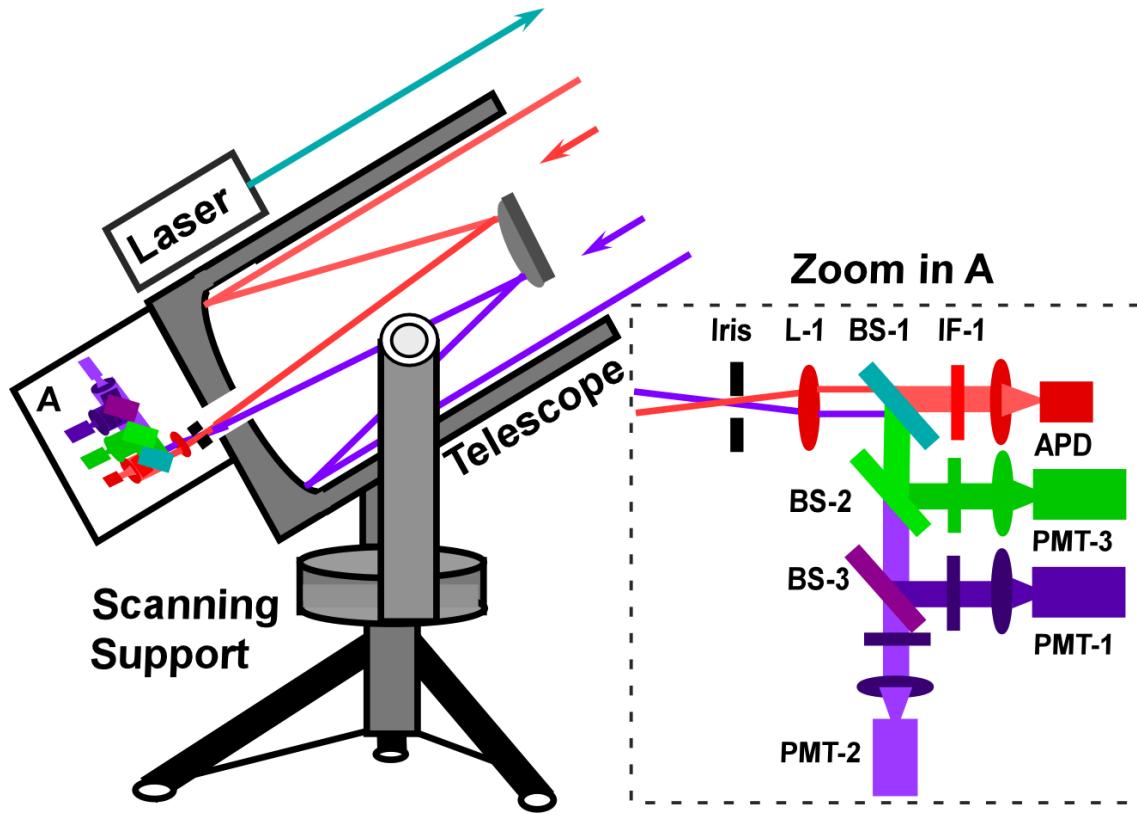


Figure 7.1: Schematic diagram of the proposed modifications to the optical components of the scanning mobile lidar system. Spectroscopic filter is shown in detail in the inlayed enlargement. BS: Beam Splitter, PMT: Photomultiplier Tube, APD: Avalanche Photodiode.

analyses that require the assumption of horizontal atmospheric homogeneity. In addition, we propose a number of hardware and software improvements to the existing mobile lidar to increase its observation potential. We propose: (a) replacing the current Newtonian telescope with a Schmidt-Cassegrain telescope which would greatly compact the lidar system (Fig. 7.1); (b) establishing the 532 nm detection channel, which would, in combination with 1064 nm detection provide more information on aerosol particles such as the Ångström exponent. The transmitter already has the capability of emitting green light, which is at the present blocked by a mechanical mask. The upgrade work includes the merging of a new beam splitter and a PMT (BS-2 and PMT-3, see in Fig. 7.1) into the receiver. As the maximum permissible exposure (MPE) of the green light (532 nm) is about 10 times less than that of the IR light (1064 nm) (International Electrotechnical Commission, 2007) within the same exposure time, eye-safety must be considered during the operation. This could be achieved by either lowering the energy output of the laser or the use of a 10X beam expander; (c) investigating and

eliminating the data event loss issues during data transfer from transient recorder into the computer that exist in the present configuration.

## Studies of aerosol transport

Investigation of the emissions of particulate matter and increased aerosol loading in urban areas using combined lidar-based remote sensing, ground-based measurements and radiosondes, was found to yield detailed information on aerosol sources, transport mechanisms, and the dynamics of the atmospheric structure. In particular, from time series of lidar scans we succeeded to reveal exact locations of aerosol sources and complex dispersion paths of the plumes. Measurements within urban regions showed daily variation cycles of aerosol loading with considerable impact of traffic conditions on air pollution. From our measurements in flat terrain configuration, we found that both the maximum height and the value of extinction coefficient of the aerosol layer close to the ground gradually decreased when moving out from urban to suburban areas. Vertical mixing of air-masses was also much more evident outside the city. In windy conditions, heterogeneous atmosphere and convective turbulence lifting aerosol plumes up to 800 m above the ground were observed. Aerosol extinctions were found to be linearly correlated to mass concentrations of  $\text{PM}_{10}$ , with slopes of  $0.0015\text{--}0.003\text{ m}^3\text{ km}^{-1}\text{ }\mu\text{g}^{-1}$  at 1064 nm.

In the long term study of aerosol transport, lidar data were combined with meteorological, environmental and radiosonde data. An attempt was made to correlate all the obtained information to categories of modeled backward trajectories of air masses and the predictions of a dedicated mineral dust cycle model. The impact of aerosols on the atmosphere was evaluated using aerosol optical depth (AOD). We established that AOD values were correlated to different categories of the air masses arriving to Slovenia. Largest AOD values in the free troposphere (FT) were in 60 % of the cases found to be a result of Saharan dust events and were found to belong to the SW class. In the atmospheric boundary layer (ABL) the situation was found to be more complex due to local aerosol sources. Nevertheless, events grouped in the SW class manifested largest average AOD value and  $\text{PM}_{10}$  concentration. High mean AOD values were observed also for local air circulation (C class) and southeastern (SE) air masses originating from the Balkans, while low values correspond to northwestern (N) and eastern (E) flows. Saharan dust and local human activities are therefore estimated to be main aerosol sources in Slovenia. Furthermore, arrival of air masses from the north and from the

southeast was found to coincide with elevated  $O_3$  concentrations. In the present study, the uncertainties regarding aerosol transport mechanisms and the impacts of aerosol presence are considerable. Long term systematic studies should be able to reduce these uncertainties to a certain extent, providing more information on the dependence of the aerosol optical properties on the origin of the air masses, and on the environmental effects of the air masses reaching Slovenia. Currently, the type and origin of the detected aerosols was estimated using the modeling of backward trajectories of air masses and their subsequent clustering. For future work we propose to use a robust polarization lidar, which would provide information on the shape of detected particles and thus greatly improve the identification of aerosols and their origins.

In this work, we also investigated the feasibility of the use of scanning lidar to reveal the atmospheric structure and particle dispersion over the complex terrain in the southwestern Slovenia, which characterized by the mountain-valley winds. Based on the obtained results, we believe that future use of a rapidly scanning lidar could significantly contribute to an improved understanding of complex meteorological phenomena in this area.

---

## Appendix

---

### Analysis of air trajectories

Air trajectory which is defined as the path of infinitesimally small parcels of air, can be described by the differential equation ([Dutton, 1986](#))

$$\frac{dX}{dt} = \dot{X}[X(t)], \quad (1)$$

where  $t$  is being time,  $X$  the position vector and  $\dot{X}$  the wind velocity vector. Considering the expansion of  $X(t)$  in a Taylor series about the initial position  $X_0$  at time  $t = t_0$ , evaluation at  $t_1 = t_0 + \Delta t$  is given

$$X(t_1) = X(t_0) + (\Delta t) \left. \frac{dX}{dt} \right|_{t_0} + \frac{1}{2} (\Delta t)^2 \left. \frac{d^2 X}{dt^2} \right|_{t_0} + \dots \quad (2)$$

The first approximation is then

$$X(t_1) \approx X_0 + (\Delta t) \dot{X}(t_0). \quad (3)$$

This is a “zero acceleration” solution. In very short integrated time steps, trajectories are of sufficient accuracy ([Stohl, 1998](#)).

Trajectories computed using the HYSPLIT model ([Draxler and Hess, 1998](#)) in present study, were given in geodetic coordinate. Using the trigonometrical transformation, Cartesian coordinates  $X$ ,  $Y$  and  $Z$  are, respectively

$$\begin{aligned} X &= r \sin \phi \cos \theta, \\ Y &= r \sin \phi \sin \theta, \\ Z &= r \cos \phi, \end{aligned} \quad (4)$$

where  $r$  is the distance from the origin of the coordinate system (the center of the earth),  $\phi$  the zenith angle and  $\theta$  the azimuth angle. In order to setup a local reference system, further transformations are required

$$[x, y, z]_{\text{local}} = \mathbf{A}^{-1}[(X, Y, Z)_{\text{traj}} - (X, Y, Z)_{\text{local}}], \quad (5)$$

where  $(X, Y, Z)_{\text{traj}}$  is the generic coordinate of air trajectory and  $(X, Y, Z)_{\text{local}}$  the coordinate of the observation site (Otlica, in our case). The rotation matrix of shape  $\mathbf{A}$  can be expressed as

$$\mathbf{A} = \begin{pmatrix} -\sin \phi_{\text{ot}} \cos \theta_{\text{ot}} & -\sin \theta_{\text{ot}} & \cos \phi_{\text{ot}} \cos \theta_{\text{ot}} \\ -\sin \phi_{\text{ot}} \sin \theta_{\text{ot}} & \cos \theta_{\text{ot}} & \cos \phi_{\text{ot}} \sin \theta_{\text{ot}} \\ \cos \phi_{\text{ot}} & 0 & \sin \phi_{\text{ot}} \end{pmatrix}, \quad (6)$$

where  $\phi_{\text{ot}}$  and  $\theta_{\text{ot}}$  are the geodetic coordinates of Otlica with respect to the center of the earth (latitude and longitude, respectively). The Euclidean distance between two trajectories is then calculated by

$$d_{i,j} = \sqrt{\sum_{m=1}^M [(x_{i,m} - x_{j,m})^2 + (y_{i,m} - y_{j,m})^2 + (z_{i,m} - z_{j,m})^2]}, \quad (7)$$

where  $M$  is the total data points of the trajectory.

The  $K$ -means algorithm (Kaufman and Rousseeuw, 2005), which was employed to group the trajectories in present study, aims to minimize the Euclidean distance between the centroid of the cluster  $C_A$  and the data points of all of the trajectories within cluster  $A$ . The distance is written as

$$d_A = \sum_{i=1}^N \sum_{m=1}^M \|X_i(x_m, y_m, z_m) - C_A\|, \quad (8)$$

where  $N$  is the number of the trajectories and  $\|X_i - C_A\|$  represents the Euclidean distance between trajectory  $i$  and cluster centroid  $C_A$ .

The optimum number of clusters is not a priori fixed by the clustering algorithm. Generally, clustering is performed separately for different candidate numbers of clusters, in which each trajectory is assigned to the cluster that is closest in terms of Euclidean distances. To determine the optimum number, two validation methods are then applied: the Silhouette method (Kaufman and Rousseeuw, 2005), which consid-



ers how well trajectories are grouped around centroids; the Root Mean Square Deviation (RMSD) method (Dorling et al., 1992), which estimates how well trajectories are assigned within the particular cluster.

## Silhouette method

Average distance between trajectory  $i$  and all of the other trajectories within cluster  $A$  can be determined by

$$d_{i,A} = \sum_{j=1}^{N_A-1} \frac{d_{i,j}}{N_A - 1}, \quad (9)$$

where  $N_A$  is the number of the trajectories in cluster  $A$ . Similarly, the distance between trajectory  $i$  and trajectories within cluster  $B$  can be written as

$$d_{i,B} = \sum_{j=1}^{N_B} \frac{d_{i,j}}{N_B}. \quad (10)$$

Considering all other sets of trajectories, the smallest distance is

$$d_{i,L} = \min_{B \neq A} \{d_{i,B}\}. \quad (11)$$

The cluster  $L$  obtained from the minimum is “the second best choice” for trajectory  $i$ . The silhouette value  $s$  is then defined as

$$s(i) = \frac{d_{i,L} - d_{i,A}}{\max\{d_{i,A}, d_{i,L}\}}. \quad (12)$$

Based on different silhouette values, trajectory  $i$  is assigned to cluster  $A$  or cluster  $L$ . Mean silhouette value of the cluster is then written as

$$\bar{s}(A) = \frac{1}{N_A} \sum_{i=1}^{N_A} \left(1 - \frac{d_{i,A}}{d_{i,L}}\right). \quad (13)$$

## RMSD method

Considering a cluster  $A$  which includes  $N_A$  trajectories, the mean trajectory can be expressed by

$$X_A = \begin{pmatrix} \bar{x}_1^A & \bar{y}_1^A & \bar{z}_1^A \\ \bar{x}_2^A & \bar{y}_2^A & \bar{z}_2^A \\ \vdots & \vdots & \vdots \\ \bar{x}_M^A & \bar{y}_M^A & \bar{z}_M^A \end{pmatrix}, \quad (14)$$

where

$$\begin{aligned} \bar{x}_m^A &= \frac{1}{N_A} \sum_{i=1}^{N_A} x_{i,m}^A, \\ \bar{y}_m^A &= \frac{1}{N_A} \sum_{i=1}^{N_A} y_{i,m}^A, \\ \bar{z}_m^A &= \frac{1}{N_A} \sum_{i=1}^{N_A} z_{i,m}^A. \end{aligned} \quad (15)$$

The RMSD from mean trajectory of cluster  $A$  is

$$\sigma_A = \frac{1}{N_A} \sqrt{\sum_{i=1}^{N_A} \sum_{m=1}^M [(x_{i,m}^A - \bar{x}_m^A)^2 + (y_{i,m}^A - \bar{y}_m^A)^2 + (z_{i,m}^A - \bar{z}_m^A)^2]}. \quad (16)$$

The total RMSD value for all clustering groups  $K$  is

$$\sigma_K = \sqrt{\sum_{k=1}^K \sigma_k}. \quad (17)$$

The RMSD tends to be smaller with larger number of clusters  $K$  and greater with smaller number. The relative percentage change of the RMSD due to reduced number of clusters is defined as

$$\epsilon = \frac{\sigma_K - \sigma_{K+1}}{K + 1} 100\%, \quad (18)$$

where calculation is from the assumed maximum value to the possible minimum value (2, for instance).

---

## References

---

- Alpers, W., Ivanov, A. Y., and Horstmann, J.: Bora events over the Adriatic Sea and Black Sea studied by multi-sensor satellite imagery, in: Proceedings of the International Geoscience and Remote Sensing Symposium (IGARSS), pp. 1307–1313, Toulouse, France, 2007.
- Andreae, M. O. and Crutzen, P. J.: Atmospheric aerosols: Biogeochemical sources and role in atmospheric chemistry, *Science*, **276**, 1052–1058, 1997.
- Ansmann, A., Riebesell, M., and Weitkamp, C.: Measurements of atmospheric aerosol extinction profiles with a Raman lidar, *Optics Lett.*, **15**, 746–748, 1990.
- Ansmann, A., Riebesell, M., Wandinger, U., Weitkamp, C., Voss, E., Lahmann, W., and Michaelis, W.: Combined Raman elastic-backscatter LIDAR for vertical profiling of moisture, aerosol extinction, backscatter, and LIDAR ratio, *Appl. Phys. B*, **55**, 18–28, 1992.
- Atkins, P. and De Paula, J.: *Physical Chemistry*, Oxford Univ. Press, New York, 2002.
- Barnada, F. and Gobbi, G. P.: Aerosol seasonal variability over the Mediterranean region and relative impact of maritime, continental and Saharan dust particles over the basin from MODIS data in the year 2001, *Atmos. Chem. Phys.*, **4**, 2367–2391, 2004.
- Bernard, V.: *Molecular Fluorescence: Principles and Applications*, Wiley-VCH Verlag GmbH, Weinheim, Germany, 2001.
- Betzer, P. R., Carder, K. L., Duce, R. A., Merrill, J. T., Tindale, N. W., Uematsu, M., Costello, D. K., Young, R. W., Feely, R. A., Breland, J. A., Bernstein, R. E., and Greco, A. M.: Long-range transport of giant mineral aerosol particles, *Nature*, **336**, 568–571, 1988.

- Birmili, W., Heinke, K., Pitz, M., Matschullat, J., Wiedensohler, A., Cyrys, J., Wichmann, H.-E., and Peters, A.: Particle number size distributions in urban air before and after volatilisation, *Atmos. Chem. Phys.*, **10**, 4643–4660, 2010.
- Bissonnette, L. R.: Multiple-scattering lidar equation, *Appl. Opt.*, **35**, 6449–6465, 1996.
- Bissonnette, L. R. and Hutt, D. L.: Multiply scattered aerosol lidar returns: inversion method and comparison with in situ measurements, *Appl. Opt.*, **34**, 6959–6975, 1995.
- Bohren, F. C. and Huffman, D. R.: *Absorption and Scattering of Light by Small Particles*, John Wiley & Sons, New York, 1983.
- Bosenberg, J., Matthias, V., Amodeo, A., Amoiridis, V., Ansmann, A., Baldasano, J. M., Balin, I., Balis, D., Bockmann, C., Boselli, A., Carlsson, G., Chaikovsky, A., Chourdakis, G., *et al.*: A European Aerosol Research Lidar Network to Establish an Aerosol Climatology, Max-Planck-Institute (MPI) Report, **No. 348**, 1–191, 2003.
- Bucholz, A.: Rayleigh-scattering calculations for the terrestrial atmosphere, *Appl. Opt.*, **34**, 2765–2773, 1995.
- Che, H. Z., Shi, G. Y., Zhang, X. Y., Arimoto, R., Zhao, J. Q., Xu, L., Wang, B., and Chen, Z. H.: Analysis of 40 years of solar radiation data from China, 1961–2000, *Geophys. Res. Lett.*, **32**, L06 803, doi:10.1029/2004GL022322, 2005.
- Collis, R. T. H.: LIDAR: A new atmospheric probe, *Q. J. Roy. Meteor. Soc.*, **92**, 220–230, 1966.
- Collis, R. T. H. and Russel, P. B.: Lidar measurement of particles and gases by elastic backscattering and differential absorption, in: *Laser Monitoring of the Atmosphere*, edited by Hinkley, E. D., pp. 71–151, Springer, Berlin, 1976.
- Cooper, D. and Eichinger, W.: Structure of the atmosphere in an urban planetary boundary layer from lidar and radiosonde observations, *J. Geophys. Res.*, **99**, 22 937–33 948, 1994.
- Corn, M.: Nonviable particles in the air, in: *Air Pollution*, edited by Stern, A. C., Academic Press, New York, 1968.
- Curcio, J. A. and Knestrick, G. L.: Correlation of atmospheric transmission with backscattering, *J. Opt. Soc. Amer.*, **48**, 686–689, 1958.

- De Wekker, S. F. J.: Observational and numerical evidence of depressed convective boundary layer heights near a mountain base, *J. Appl. Meteor. Climatol.*, **47**, 1017–1026, 2008.
- Del Gusta, M. and Marini, S.: On the retrieval of urban mass concentrations by a 532 and 1064 nm LIDAR, *J. Aerosol Sci.*, **31**, 1469–1488, 2000.
- Devara, P. C. S., Raj, P. E., and Sharma, S.: Remote sensing of atmospheric aerosol in the nocturnal boundary layer, *Environ. Pollut.*, **85**, 97–102, 1994.
- Dorling, S. R., Davies, T. D., and Pierce, C. E.: Cluster analysis: a technique for estimating the synoptic meteorological controls on air and precipitation chemistry – method and applications, *Atmos. Environ.*, **26**, 2575–2581, 1992.
- Draxler, R. R. and Hess, G. D.: An overview of the HYSPLIT\_4 modelling system for trajectories, dispersion and deposition, *Aust. Meteor. Mag.*, **47**, 295–308, 1998.
- Dutton, J. A.: *The Ceaseless Wind: An Introduction to the Theory of Atmospheric Motion*, Dover Pubns, New York, 1986.
- EC: Directive 2008/50/EC of the European parliament and of the council of 21 May 2008 on ambient air quality and cleaner air for Europe, *Official Journal of the European Union*, **L152**, 30–35, 2008.
- Eek, T. F., Holben, B. N., Dubovik, O., Smirnov, A., Goloub, P., Chen, H. B., Chatenet, B., Gomes, L., Zhang, X.-Y., Tsay, S.-C., Ji, Q., Giles, D., and Slutsker, I.: Columnar aerosol optical properties at AERONET sites in central eastern Asia and aerosol transport to the tropical mid-Pacific, *J. Geophys. Res.*, **110**, D06202, doi:10.1029/2004JD005274, 2005.
- Eichinger, W., Cooper, D., Buttler, W., Cottingame, W., and Tellier, L.: Use of lidar for the evaluation of traffic-related urban pollution, *Proc. SPIE*, **209**, 2102, doi:10.1117/12.170636, 1994.
- Fernald, F. G.: Analysis of atmospheric lidar observations: some comments, *Appl. Opt.*, **23**, 652–653, 1984.
- Filipčič, A., Horvat, M., Veberič, D., Zavrtanik, D., and Zavrtanik, M.: Scanning lidar based atmospheric monitoring for fluorescence detectors of cosmic showers, *Astropart. Phys.*, **18**, 501–512, 2003.

- Fiocco, G. and Smullin, L. D.: Detection of scattering layers in the upper atmosphere (60–140 km) by optical radar, *Nature*, **199**, 1275–1276, 1963.
- Forster, P., Ramaswamy, V., Artaxo, P., Bernsten, T., Betts, R., Fahey, D. W., Haywood, J., Lean, J., Lowe, D. C., Myhre, G., Nganga, J., Prinn, R., Raga, G., Schulz, M., and Van Dorland, R.: Changes in Atmospheric Constituents and in Radiative Forcing, in: *Climate Change 2007: The Physical Science Basis. Contribution of Working Group I to the Fourth Assessment Report of the Intergovernmental Panel on Climate Change*, edited by Solomon, S., Qin, D., Manning, M., Chen, Z., Marquis, M., Averyt, K. B., Tignor, M., and Miller, H. L., pp. 131–234, Cambridge Univ. Press, Cambridge, UK and New York, NY, USA, 2007.
- Fouche, D. G., Herzenberg, A., and Chang, R. K.: Inelastic photon scattering by a polyatomic molecule: NO<sub>2</sub>, *J. Appl. Phys.*, **43**, 3846–3852, 1972.
- Fujii, T. and Fukuchi, T.: *Laser Remote Sensing*, Taylor & Francis Group, Inc., 2005.
- Gao, F., Bergant, K., Filipčič, A., Forte, B., Hua, D.-X., Song, X.-Q., Stanič, S., Veberič, D., and Zavrtnik, M.: Observations of the atmospheric boundary layer across the land-sea transition zone using a scanning Mie lidar, *J. Quant. Spectrosc. Ra.*, **112**, 182–188, 2011a.
- Gao, F., Stanič, S., Bergant, K., Bolte, T., Coren, F., He, T.-Y., Hrabar, A., Jerman, J., Mladenovič, A., Turšič, J., Veberič, D., and Iršič Žibert, M.: Monitoring presence and streaming patterns of Icelandic volcanic ash during its arrival to Slovenia, *Biogeosciences*, **8**, 2351–2363, 2011b.
- Garratt, J. R.: *The Atmospheric Boundary Layer*, Cambridge Univ. Press, Cambridge, UK, 1992.
- Gasith, A. and Resh, V. H.: Streams in Mediterranean climate regions: Abiotic influences and biotic responses to predictable seasonal events, *Annu. Rev. Ecol. Syst.*, **30**, 51–81, 1999.
- Hair, J. W., Caldwell, L. M., Krueger, D. A., and She, C. Y.: High-spectral-resolution lidar with iodine-vapor filters: measurement of atmospheric-state and aerosol profiles, *Appl. Opt.*, **40**, 5280–5294, 2001.
- Hamilton, P. M.: Lidar measurement of backscatter and attenuation of atmospheric aerosol, *Atmos. Environ.*, **3**, 221–223, 1969.

- Harrison, R. M., Jones, M., and Collins, G.: Measurements of the physical properties of particles in the urban atmosphere, *Atmos. Environ.*, **33**, 309–321, 1999.
- He, T.-Y., Gao, F., Stanič, S., Veberič, D., Bergant, K., Dolžan, A., and Song, X.-Q.: Scanning mobile lidar for aerosol tracking and biological aerosol identification, *Proc. SPIE*, **7832**, 78 320U, doi:10.1117/12.868387, 2010.
- He, T.-Y., Stanič, S., Gao, F., Bergant, K., Veberič, D., Song, X.-Q., and Dolžan, A.: Tracking of urban aerosols using combined LIDAR-based remote sensing and ground-based measurements, *Atmos. Meas. Tech.*, **5**, 891–900, 2012a.
- He, T.-Y., Stanič, S., Eichinger, W., and Barnhart, B.: Investigation of vertical aerosol distributions in the vicinity of Iowa City, in: *Proc. of the 26th International Laser Radar Conference*, pp. 965–968, Porto Heli, Greece, 2012b.
- Henne, S., Furger, M., Nyeki, S., Steinbacher, M., Neininger, B., De Wekker, S. F. J., Dommen, J., Spichtinger, N., Stohl, A., and Prévôt, A. S. H.: Quantification of topographic venting of boundary layer air to the free troposphere, *Atmos. Chem. Phys.*, **4**, 497–509, 2004.
- Herman, J. R., Barthia, P., Torres, O., Hsu, C., Seftor, C., and Celarier, E.: Global distribution of UV-absorbing aerosols from Nimbus 7/TOMS data, *J. Geophys. Res.*, **102**, 16 911–16 922, 1997.
- Hoff, R. M., Guise-Bagley, L., Staebler, R. M., Wiebe, H. A., Brook, J., Georgi, B., and Dürsterdiek, T.: Lidar, nephelometer, and in situ aerosol experiments in southern Ontario, *J. Geophys. Res.*, **101**, 19 199–19 209, 1996.
- Hofmann, D. J.: Twenty years of balloon borne tropospheric aerosol measurements at Laramie, Wyoming, *J. Geophys. Res.*, **98**, 12 753–12 766, 1993.
- Holben, B. N., Eck, T. F., Slutsker, I., Tanré, D., Buis, J. P., Setzer, A., Vermote, E., Reagan, J. A., Kaufman, Y. J., Nakajima, T., Lavenue, F., Jankowiak, I., and Smirnov, A.: AERONET – a federated instrument network and data archive for aerosol characterization, *Remote Sens. Environ.*, **66**, 1–16, 1998.
- Hua, D., Uchida, M., and Kobayashi, T.: Ultraviolet high-spectral-resolution Rayleigh-Mie lidar with a dual-pass Fabry-Perot etalon for measuring atmospheric temperature profiles of the troposphere, *Optics Lett.*, **29**, 1063–1065, 2004.

- International Electrotechnical Commission, .: Safety of laser products - Part 1: Equipment classification and requirements, International Standard, **IEC 60825-1**, 2007.
- IPCC: Climate Change 2007, in: The Scientific Basis, edited by Solomon, S., Qin, D., Manning, M., Chen, Z., Marquis, M., Averyt, K. B., Tignor, M., and Miller, H. L., pp. 131–336, Cambridge Univ. Press, Cambridge, UK and New York, NY, USA, 2007.
- Jacobson, M. Z.: Fundamentals of Atmospheric Modeling, Cambridge Univ. Press, Cambridge, UK, 1998.
- Jorba, O., Jiménez-Guerrero, P., Pérez, C., and Baldasano, J. M.: Characterization of ozone and particulate matter levels in a coastal site with the application of a trajectory clustering correlation methodology, in: Proc. of the 10th Int. Conf. on Harmonisation within Atmospheric Dispersion Modelling for Regulatory Purposes, pp. 36–40, Sissi, Crete, 2005.
- Kano, M.: On the determination of backscattered and extinction coefficient of the atmosphere by using laser radar, Pap. Meteorol. Geophys., **19**, 121–129, 1968.
- Kaufman, L. and Rousseeuw, P. J.: Finding Groups in Data: An Introduction to Cluster Analysis, Wiley and Sons, New Jersey, 2005.
- Kaufman, Y. J., Tanré, D., Gordon, H. R., Nakajima, T., Lenoble, J., Frouin, R., Grassl, H., Herman, B. M., King, M. D., and Teillet, P. M.: Passive remote sensing of tropospheric aerosol and atmospheric correction for the aerosol effect, J. Geophys. Res., **102**, 16 815–16 830, 1997.
- Kaufman, Y. J., Tanre, D., and Boucher, O.: A satellite view of aerosols in the climate system, Nature, **419**, 215–223, 2002.
- Klett, J. D.: Stable analytical inversion solution for processing lidar returns, Appl. Opt., **20**, 211–220, 1981.
- Kliger, D. S.: Ultrasensitive Laser Spectroscopy, Academic Press, New York, 1983.
- Kovalev, V. A. and Eichinger, W. E.: Elastic Lidar: Theory, Practice and Analysis Methods, Wiley and Sons, New York, 2004.
- Lagrosas, N., Kuze, H., Takeuchi, N., Fukagawa, S., Bagtasa, G., Yoshii, Y., Naito, S., and Yabuki, M.: Correlation study between suspended particulate matter and portable automated lidar data, J. Aerosol Sci., **36**, 439–454, 2005.



- Lakowicz, J. R.: Principles of Fluorescence Spectroscopy, Kluwer Academic/Plenum, New York, 1999.
- Lelieveld, J., Berresheim, H., Borrmann, S., Crutzen, P. J., Dentener, F. J., Fischer, H., Feichter, J., Flatau, P. J., Heland, J., Holzinger, R., Kormann, R., Lawrence, M. G., Levin, Z., *et al.*: Global air pollution crossroads over the Mediterranean, *Science*, **298**, 794–799, 2002.
- Lewandowski, P. A., Eichinger, W. E., Holder, H., Prueger, J., Wang, J., and Kleinman, L. I.: Vertical distribution of aerosols in the vicinity of Mexico City during MILAGRO-2006 Campaign, *Atmos. Chem. Phys.*, **10**, 1017–1030, 2010.
- Li, Z.: Influence of absorbing aerosols on the inference of solar surface radiation budget and cloud absorption, *J. Climate*, **11**, 5–17, 1998.
- Mattis, I., Jaenisch, V., Müller, D., Franke, K., and Ansmann, A.: Classification of particle extinction profiles derived within the framework of the German lidar network by the use of cluster analysis of back trajectories, in: *Lidar Remote Sensing of the Atmosphere*, edited by Dabas, A. *et al.*, pp. 211–214, Ed. Ecole Polytech., Palaiseau, France, 2000.
- McCartney, E. J.: Optics of Atmosphere: Scattering by Molecules and Particles, John Wiley & Sons, New York, 1977.
- McClung, F. J. and Hellwarth, R. W.: Giant optical pulsations from ruby, *J. Appl. Phys.*, **33**, 828–829, 1962.
- McGill, M., Hlavka, D., Hart, W., Scott, V. S., Spinhirne, J., and Schmid, B.: Cloud physics lidar: instrument description and initial measurement results, *Appl. Opt.*, **41**, 3725–3734, 2002.
- Measures, R. M.: Laser Remote Sensing: Fundamentals and Applications, Wiley, New York, 1984.
- Measures, R. M.: Laser Remote Chemical Analysis, Wiley, New York, 1988.
- Melchior, H.: Demodulation and Photodetection Techniques, in: *Laser Handbook*, edited by Arecchi, F. T. and Schultz-Dubois, E. O., North Holland, Amsterdam, 1972.
- Min, C.: Local level set method in high dimension and codimension, *J. Comput. Phys.*, **200**, 368–382, 2004.

- Nickovic, S., Kallos, G., Papadopoulos, A., and Kakaliagou, O.: A model for prediction of desert dust cycle in the atmosphere, *J. Geophys. Res.*, **106**, 18 113–18 129, 2001.
- Penndorf, R.: Tables of the refractive index for standard air and the Rayleigh scattering coefficient for the spectral region between 0.2 and 20 microns and their application to atmospheric optics, *J. Opt. Soc. Amer.*, **47**, 176–182, 1957.
- PerkinElmer: Long wavelength Enhanced Silicon APD, C30954EH, C30955EH and C30956EH Series, URL [www.excelitas.com/downloads/DTS\\_LongWLEnSiliconAPDSeries.pdf](http://www.excelitas.com/downloads/DTS_LongWLEnSiliconAPDSeries.pdf), 2012.
- Rosenfeld, D.: Suppression of rain and snow by urban and industrial air pollution, *Science*, **287**, 1793–1796, 2000.
- Russell, P. B., Uthe, E. E., Ludwig, F. L., and Shaw, N. A.: A comparison of atmospheric structure as observed with monostatic acoustic sounder and lidar techniques, *J. Geophys. Res.*, **79**, 5555–5566, 1974.
- Russell, P. B., Hobbs, P. V., and Stowe, L.: Aerosol properties and radiative effects in the United States East Coast haze plume: an overview of the Tropospheric Aerosol Radiative Forcing Observational Experiment (TARFOX), *J. Geophys. Res.*, **104**, 2213–2222, 1999.
- Sicard, M., Chazette, P., Pelon, J., Won, J. G., and Yoon, S.: Variational method for the retrieval of the optical thickness and the backscatter coefficient from multiangle lidar profiles, *Appl. Opt.*, **41**, 493–502, 2002.
- Slingo, A.: Sensitivity of the Earth's radiation budget to changes in low clouds, *Nature*, **343**, 49–51, 1990.
- Spinhirne, J. D.: Micro pulse lidar, *IEEE T. Geosci. Remote*, **31**, 48–55, 1993.
- Spinhirne, J. D., Reagan, J. A., and Herman, B. M.: Vertical distribution of aerosol extinction cross section and inference of aerosol imaginary index in the troposphere by lidar technique, *J. Appl. Meteorol.*, **19**, 426–438, 1980.
- Spuler, S. M. and Mayor, S. D.: Scanning eye-safe elastic backscatter lidar at 1.5-micron wavelength, *J. Atmos. Ocean. Tech.*, **22**, 696–703, 2005.
- Stohl, A.: Computation, accuracy and applications of trajectories – a review and bibliography, *Atmos. Environ.*, **32**, 947–966, 1998.

- Stull, P. B.: An Introduction to Boundary Layer Meteorology, Kluwer Academic Publisher, Dordrecht, 1988.
- Taylor, J. R.: An Introduction to Error Analysis: the study of uncertainties in physical measurements, University Science Books, Sausalito, California, 1997.
- U.S. Standard Atmosphere, .: U.S. Standard Atmosphere, 1976, U.S. Government Printing Office, Washington, D.C., 1976.
- Van de Hulst, H. C.: Light Scattering by Small Particles, John Wiley & Sons, New York, 1957.
- Wandinger, U.: Multiple-scattering influence on extinction-and backscatter-coefficient measurements with Raman and High-Spectral-Resolution lidars, *Appl. Opt.*, **37**, 417–427, 1998.
- Weinman, J. A.: Derivation of atmospheric extinction profiles and wind speed over the ocean from a satellite-borne lidar, *Appl. Opt.*, **27**, 3994–4001, 1988.
- Weitkamp, C.: Laser: Range-Resolved Optical Remote Sensing of the Atmosphere, Springer, New York, 2005.
- Winker, D. M., Hunt, W. H., and McGill, M. J.: Initial performance assessment of CALIOP, *Geophys. Res. Lett.*, **34**, L19 803, doi:10.1029/2007GL030135, 2007.
- Winker, D. M., Vaughan, M. A., Omar, A., Hu, Y., Powell, K. A., Liu, Z., Hunt, W. H., and Young, S. A.: Overview of the CALIPSO mission and CALIOP data processing algorithms, *J. Atmos. Ocean. Tech.*, **26**, 2310–2323, 2009.
- Winker, D. M., Pelon, J., Coakley Jr., J. A., Ackerman, S. A., Charlson, R. J., Colarco, P. R., Flamant, P., Fu, Q., Hoff, R., Kittaka, C., Kubar, T. L., LeTreut, H., McCormick, M. P., Megie, G., Poole, L., Powell, K., Trepte, C., Vaughan, M. A., and Wielicki, B. A.: A global 3D view of aerosols and clouds, *B. Am. Meteorol. Soc.*, **91**, 1211–1229, 2010.